

UNIVERSITY OF
BIRMINGHAM

4th annual
BEAR
PGR CONFERENCE 2013



on

Research Computing

16th December 2013

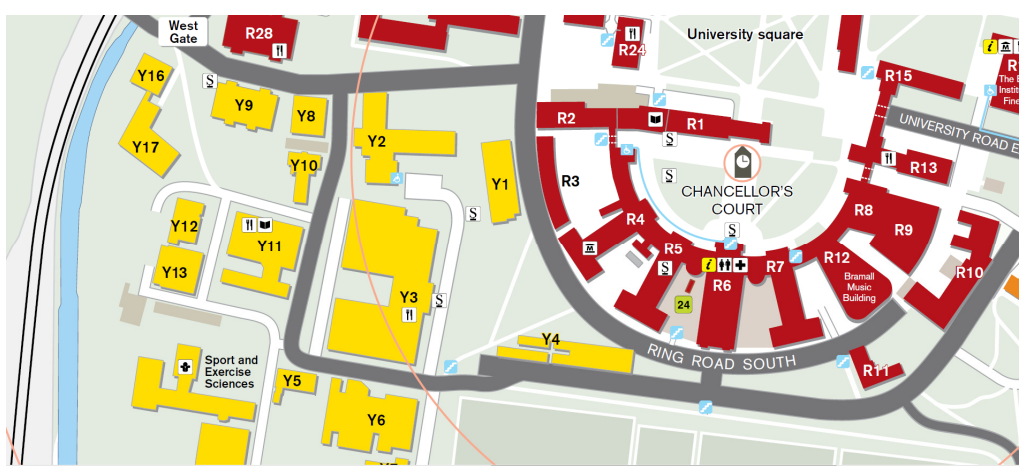
Sponsored by



4th annual BEAR Postgraduate Researcher Conference 2013

Welcome to the fourth annual Birmingham Environment for Academic Research (BEAR) Postgraduate Researcher Conference. This event offers an exciting opportunity for postgraduate students and early-career researchers to present their work to academics, industry professionals and their peers. Keynote speakers from industry and academia will describe their experiences using numerical modelling in their respective fields. We look forward to a day of exciting oral and poster presentations on a variety of interesting research topics from across the University Colleges and Schools. Additionally, there will be plenty of opportunity for discussion with like-minded colleagues from the University during coffee and lunch breaks.

The conference will be held in the lecture theatre G34 at the School of Civil Engineering, University of Birmingham (Building Y3 on the map). Breakfast, coffee breaks and lunch will be served in the Shell Lounge while poster presentations will be in room G36 in the same building.



| Organising Committee | Advisory Committee |
|-----------------------------|---------------------|
| Dominic Flynn (Chair) | Prof John Bridgeman |
| Rebecca Sindall (Secretary) | Dr Hassan Hemida |
| Danique Fintelman | Earl Joseph |
| Hamid Rakhodaei | Aslam Ghumra |
| Zainab Al-sharify | |
| Komal Pahwa | |
| Nazita Bonab | |

Contact us: pgrsecretary@lists.bham.ac.uk

Conference Programme

| Time | Speaker | Title | Chair |
|-------------|--|---|-------------------|
| 9:00-9:30 | Registration in Shell Lounge, School of Civil Engineering (Breakfast provided) | | |
| 9:30-9:45 | Prof. John Bridgeman | Welcome | Dr Hassan Hemida |
| 9:45-10:30 | Prof. Roy Johnston | Keynote speaker: Computational Chemistry, University of Birmingham | |
| 10:30-10:45 | James Cumby | Magnetic Pathways: exploring the energy landscape | |
| 10:45-11:00 | Claire Green | Derivation of enhanced interatomic potentials for Thorium dioxide (ThO ₂): a potential nuclear fuel | |
| 11:00-11:30 | Tea and coffee | | |
| 11:30-11:45 | Alireza Rastegarpanah | Analysis and simulation of various Stewart Platform configurations for lower limb rehabilitation | Dominic Flynn |
| 11:45-12:00 | Mohamed Wehbi | Investigating the effects of soft spots on the functional and structural condition of a railway track | |
| 12:00-12:15 | Hamid Rakhodaei | Methodology development of design of a hybrid parallel robot | |
| 12:15-12:30 | James Turner | Parallel solution of the linear elasticity problem with applications in topology optimization | |
| 12:30-13:30 | Lunch | | |
| 13:30-14:15 | Dr Jim Wicks | Keynote speaker: Computational Fluid Dynamics (CFD) and Process Simulation, The Fluid Group | Rebecca Sindall |
| 14:15-14:30 | Justin Morden | Comparison of CFD methods to wind-tunnel data for a Class 43 high speed train | |
| 14:30-14:45 | Danique Fintelman | Numerical investigation of the effect of crosswind on cyclists | |
| 14:45-15:15 | Tea and coffee | | |
| 15:15-15:30 | Dominic Flynn | Detached-eddy simulation of the slipstream of an operational freight train | Danique Fintelman |
| 15:30-15:45 | Rebecca Sindall | CFD modelling of lab-scale anaerobic digesters to determine experimental sampling locations | |
| 15:45-16:00 | Chris Meah | Development of simulation tools for exploring plenoptic camera applications | |
| 16:00-16:15 | Nan Jian | Atlas of simulated images for Au ₅₅ nanoclusters multislice method | |
| 16:15-16:30 | Dr Hassan Hemida | Closing remarks | |
| 16:30-17:30 | Drinks reception and prize giving | | |

Posters will be on display in the Shell Lounge and in G34 throughout the day.

Presenters are asked to liaise with session chairs to ensure that all presentations are uploaded in the break prior to each session. This will help keep the conference running to schedule.

Welcome

Welcome to the University of Birmingham and to the fourth annual BEAR conference, organised by postgraduate researchers from the College of Engineering and Physical Sciences. The research undertaken within the University cuts across a diverse range of themes and the BEAR conference is a wonderful opportunity for researchers from all disciplines to come together and share their experiences and research successes undertaken using our impressive high performance computing facilities, BEAR (Birmingham Environment for Academic research).



One of the many roles of a University is to encourage and facilitate multidisciplinary research, education and development in a broad range of fields. An essential component of this is the effective dissemination of high quality research, and the hosting of regular conferences and workshops in critical areas assists in the transfer of knowledge and good practice to the academic and industrial communities. Thus, the purpose of this conference is to promote the exchange of the latest information and developments in various fields, all underpinned by a common interest in high performance computing.

This is the fourth conference in the series of annual events that provide an excellent opportunity for scientists, engineers and other academic researchers to network and discuss key issues. The event builds on the success of the previous conferences held annually in Birmingham since 2010. Thanks to an excellent response to the call for papers, the Organising Committee has been able to put together a wide ranging programme. I am delighted that so many researchers are keen to share their work with their peers and look forward to a stimulating event where we learn more of subjects ranging from the effects of crosswinds on cyclists, to the structural condition of rail tracks, to potential nuclear fuels.

Many thanks for joining us at the conference which the Organising Committee and I hope you will find interesting, informative and enjoyable.

John Bridgeman

Professor of Environmental Engineering

Director of Research and Knowledge Transfer, College of Engineering and Physical Sciences

Key note speakers

Professor Roy Johnston

Roy Johnston is Professor of Computational Chemistry and Deputy Head of the School of Chemistry at University of Birmingham. He is the School's Director of Research, Chair of the Postgraduate Research Committee of the College of Engineering and Physical Sciences and represents the College on the University's Graduate School Management Board. He is also a member of the Research Computing Management Board.

Roy has published over 150 research papers in scientific journals as well as reviews and book chapters in the fields of computational nanoscience and applications of nature-inspired computation. He has also authored a book "Atomic and Molecular Clusters" (2002) and edited several volumes and special issues of journals.

He has received major grants from EPSRC (including a Programme Grant of approximately £2.5M) and the Leverhulme Trust and is on the Management Committee of an EU COST Action on nanoalloys.

Dr Jim Wicks

Jim Wicks is the director of Computational Fluid Dynamics (CFD) and Process Simulation at The Fluid Group. He is a former Fellow of the University of Cambridge in Physics, a Research Fellow at both UCL (London) and the University of Oxford.

With a PhD in Physics from Oxford University in 1993, Jim spent 5 years as a leading academic, before joining a major UK company to manage a team of environmental modellers. After 7 years in the commercial arena, Jim founded The Fluid Group in Oxford, with the goal of being the best water, chemical, medical and environmental fluid modelling company in the UK.

A specialist in CFD and fluid physics, Jim has a long history of working in a range of diverse projects in the UK and overseas. The Fluid Group are specialists in Computational Fluid Dynamics & Process Modelling for Chemical Engineering, Water and Wastewater Treatment.

Oral abstracts and papers

Magnetic Pathways – exploring the energy landscape

James Cumby¹, Colin Greaves¹ and David Quigley²

¹School of Chemistry, University of Birmingham, UK.

²Department of Physics, University of Warwick, UK.

c.greaves@bham.ac.uk

Abstract

This study reports the use of computer modelling (particularly using density functional theory) to analyse magnetic interactions within a series of compounds structurally and chemically related to Schafarzikite (FeSb_2O_4). This technique has provided further understanding of the complex magnetic order observed in such structures, while also predicting a ferromagnetic derivative for the first time. This prediction has since been shown to be correct through a corresponding experimental study.

1 Introduction

Magnetism is important in many aspects of modern life, from loudspeakers and credit cards through to transformers and medical MRI machines. As such, magnetism is a highly active area of research across many disciplines, as in many cases the underlying physical properties are not entirely understood. The quest for new materials is necessary in order to improve existing technologies, and provide advanced materials for future applications. A prime example of this is computer hard-drives, where the limiting factor in magnetic storage density is the size of individual magnetic domains, and how small they can become without losing data integrity. This limit is gradually approaching, and so new devices must start to use other techniques. Low dimensional materials are one possible solution to the problem; these substances possess structures that give rise to highly directional properties. One

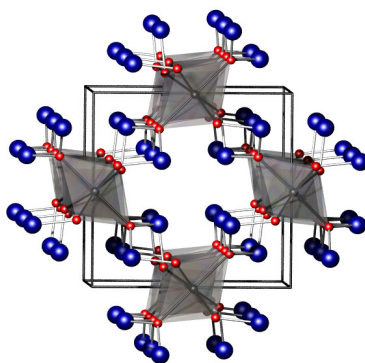


Figure 1: Schafarzikite crystal structure viewed along c -axis: Fe – grey octahedra, Sb – blue spheres, O –

example would be a one-dimensional (1D) ‘wire’ for conducting electricity, which would ideally have high conductivity along one crystallographic direction, but low conductivity otherwise. Low dimensional magnetism could be one solution to the hard drive limit, as magnetic domains involving directionality may be able to overcome interference from surrounding magnetic fields, and thus more stable for data recording. Combining these novel magnetic properties with another capability (such as the electrical conductivity mentioned above) could lead to an easy way to control the magnetic ordering over even smaller length scales, and also improve device performance.

Schafarzikite (Figure 1) is a rare mineral with the chemical formula FeSb_2O_4 . It possesses a crystal structure similar to rutile (TiO_2) of opposite edge-sharing FeO_6 octahedra, but here the dimensionality is reduced (to approximately 1D) due to antimony linkages between these octahedral ‘chains’. It is of great chemical interest, however, due to the ability to dope and/or fully substitute some atoms in the structure with other cations such as Mn^{2+} , Co^{2+} and Pb^{4+} (de Laune *et al.*, 2012). These dopants have been shown experimentally to lead to fundamental changes in the properties of the materials.

Many of the MSb_2O_4 compounds ($\text{M} = \text{Mn}, \text{Fe}, \text{Co}, \text{Ni}$) have been shown to order magnetically at low temperatures (approximately 60 K or -213°C) but the exact nature of this ordering is critically dependant on the ions present in the structure. The ability to control the magnetic properties through doping is obviously desirable in order to develop specific device properties. In many cases, however, the exact cause of these changes in magnetic behaviour is not fully understood. This study has used density functional theory (DFT) modelling of the bulk electronic structure to evaluate the interactions present between magnetic cations, and further understand the properties. The study has also extended to prediction of the first example of a ferromagnetic Schafarzikite variant, CuAs_2O_4 . This compound (found naturally as the mineral Trippkeite [Pertlik, 1975]) has since been shown to order ferromagnetically below 8 K, as predicted (Cumby *et al.*, 2013).

2 Results

Schafarzikite and its derivatives can adopt a number of different magnetic structures, excluding arrangements involving a magnetic supercell. The differences relate to whether the magnetic moments (represented by green arrows) on a given cation (grey spheres) are aligned in the same direction as the adjacent cations, or opposed. By considering interactions both along a given octahedral chain and between adjacent chains, this gives rise to four possible structures, which are labelled A, C, G and F (Figure 2). For a given chemical composition, one of these magnetic structures (or possibly a combination) will be lowest in energy, and therefore favourable at low temperature. From neutron diffraction experiments, an A-type order is seen for $\text{M} = \text{Mn}$ and Fe , while a C-type order is seen for $\text{M} = \text{Co}$ and Ni .

Using DFT (as implemented using the CASTEP package [Clark *et al.*, 2005]) we have been able to calculate the relative energies of each of the magnetic structures for a range of cation substitutions, the results of which have agreed well with the experimentally determined structures. Using these energies, it is then possible to compute the strength of the nearest-neighbour magnetic interactions, denoted J . These indicate which interaction is most influential for the resulting magnetic structure, and have revealed some surprising results. As expected due to the close proximity of magnetic ions along the chains, the ‘direct’ coupling (J_1) is most significant, promoting the change from A- to C-type order on varying the transition metals. The calculations reveal that the diagonal coupling between adjacent chains is stronger than expected, however, in some cases to a similar order of magnitude as J_1 . This is

surprising given the large length-scale over which the interaction occurs (ca. 12 Å, compared with 3 Å along the chains) and indicates the effective exchange mechanism along the highly covalent O–Sb–O linkages.

The previous result led to the investigation of CuSb_2O_4 and CuAs_2O_4 as a potential example where this inter-chain coupling was reduced, due to the electronic configuration of Cu^{2+} . Both of these materials show a strongly positive coupling along the chains, but negligible coupling between chains, as desired. The net result of this is that DFT indicates both copper-containing materials to exhibit ferromagnetic behaviour (type-F). Following this result, a synthetic sample of CuAs_2O_4 has been shown to be ferromagnetic below 8 K, consistent with the predictions. Currently, synthesis of CuSb_2O_4 has proved unsuccessful, and so the prediction cannot be confirmed.

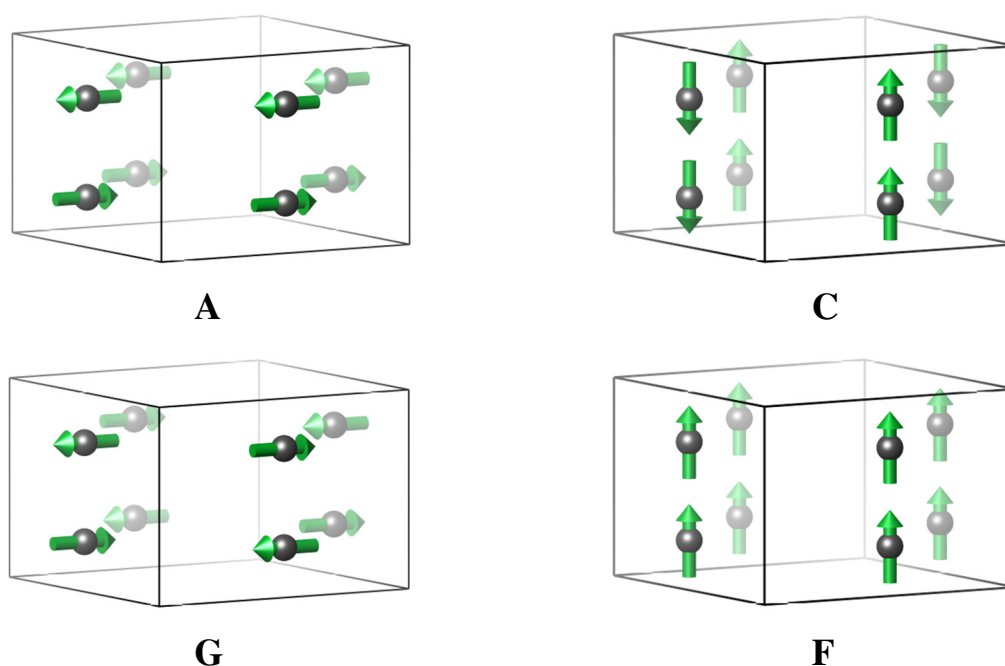


Figure 2: Magnetic ordering possibilities in Schafarzikite-related materials (only magnetic cations shown)

References

De Laune, B. & Greaves, C. 2012, Structural and magnetic characterisation of CoSb_2O_4 , and the substitution of Pb^{2+} for Sb^{3+} . *Journal of Solid State Chemistry*, **187**, 225-230.

Pertlik, F, Verfeinerung der Kristallstruktur von synthetischem Trippkeit, CuAs_2O_4 , *Tschermaks mineralogische und petrographische mitteilungen*, **22**, 211-217.

Cumby, J., Greaves, C. and Quigley, D., *Unpublished*.

Clark, S. J., Segall, M. D., Pickard, C. J., Hasnip, P. J., Probert, M. I. J., Refson, K. & Payne, M. C., First principles methods using CASTEP, *Zeitschrift fuer Kristallographie*, **220**, 567-570.

Numerical investigation of the effect of crosswind on cyclists

D.M. Fintelman¹, H. Hemida², M. Sterling² and F-X Li¹

¹School of Sport, Exercise and Rehabilitation Sciences, University of Birmingham, UK.

²School of Civil Engineering, University of Birmingham, UK.

DMF144@bham.ac.uk

Abstract

The aim of the study was to investigate the effect of crosswind on the aerodynamic responses of cyclists. The Reynolds Averaged Navier Stokes (RANS) SST $k-\omega$ model and $k-\epsilon$ turbulence models were employed. The geometry was a full scale model of a cyclist on a bicycle. The Reynolds number was 8.9×10^5 , based on the effective wind velocity and height of the cyclist from the floor. A good agreement (RMSE = 0.12) has been found between the simulation results and the experimental data. The aerodynamic force coefficients at different yaw angles have been obtained and the main feature of the flow around the cyclist determined. The results of this study will help to improve the understanding of the aerodynamic behaviour of cyclists in crosswind.

1 Introduction

Crosswinds can have an impact on the performance, stability and safety of a cyclist. To the best of the author's knowledge no studies have investigated the effect of crosswind on the aerodynamic behaviour of cyclists at yaw angles $> 30^\circ$ (i.e. the angle of the wind with the cyclists direction of travel as shown in Fig. 1) despite the several occurrences of fatal accidents due to crosswinds (Department of Transport, 2012). To improve the safety of cyclists and equipment, it is crucial to understand the flow field around cyclists and to calculate the corresponding aerodynamic forces. There are different methods which can be used to investigate the flow pattern around cyclists and one of these is numerical modelling, i.e., Computational Fluid Dynamic (CFD) simulations. CFD analysis gives comprehensive information compared to analytical and experimental fluid dynamics, where information is dependent on the position of the measurement instrument. Conversely, only a limited number of CFD based studies in cycling are published (Hanna, 2002; Lukes et al., 2004; Defraeye et al., 2010; Griffith et al., 2012). Except a study on the effect of disk wheels in full side wind (Hanna, 2002), all current CFD studies are focused on windless environmental conditions. Since it is appreciated by road safety specialists, road designers and bicycle developers that worse case conditions can occur, side wind analysis at crosswind yaw angles $> 30^\circ$ is essential. However, a comprehensive study about the effect of crosswind on bicycle and cyclist is lacking in the literature. Hence, the aim of this CFD study is to investigate the effect of crosswind on cyclists at different crosswind yaw angles.

2 Method

The flow around a cyclist on a bicycle is computed for different crosswind angles ranging between 0 to 90°. The flow field around a cyclist is obtained with two different Reynolds Averaged Navier Stokes (RANS) turbulence models: the two-equation SST $k-\omega$ and $k-\epsilon$ models. These models are commonly used in crosswind vehicle studies. The method is validated with full-scale wind tunnel experiments of a mannequin on a bicycle (Fig 1a). In order to simulate realistic flow conditions, the geometry of the mannequin on the bicycle of the wind tunnel experiments is used as shown in Fig. 1b. The geometry has a high level of complexity. All main components are included in the computational model, whilst smaller features have been excluded such as the bicycle cables, spokes, chain and brakes, as these small details will consume many grid cells. The cyclist has been positioned with straight arms, the hands on the dropped handlebars and in a torso angle position of 24° with respect to the ground.

The computational domain is shown in Fig. 2a, where H (1.35m) represents the height of the cyclists. The bicycle has been placed on the floor of the computational domain as shown in Fig. 2a. A generalized computational domain has been used in all simulations, regardless of the crosswind conditions. The domain has a length, width and height of 21H, 21H and 5.2H respectively. The front wheel of the bicycle has been positioned 4.6H from the front and side inlet to prevent effects of the bicycle on the pressure inlet. A refinement box has been defined around the bicycle and cyclist to refine the mesh in the region close to geometry. The length, width and height of the refinement box are respectively 5.7H, 5.1H and 1.3H. Three different meshes are created with different number of nodes. The coarse, medium and fine mesh consist of 7.3×10^6 , 13.1×10^6 and 17.9×10^6 nodes, respectively. An example of the surface mesh is shown in Fig. 2b. For the fine mesh, the dimensionless normal wall distance is 25.2.

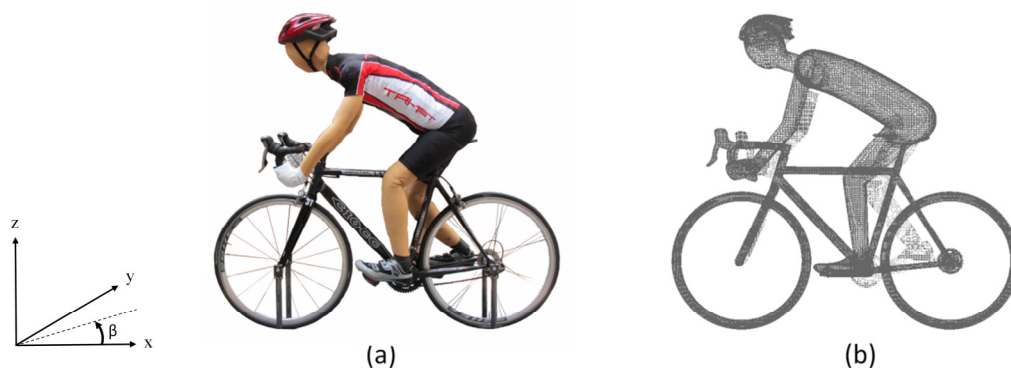


Figure 1: (a) Bicycle with mannequin used in the wind tunnel experiments and (b) geometry of bicycle with cyclist in the simulations.

The initial conditions of the simulations are chosen to closely reassemble the wind tunnel experiments. A turbulence intensity (i.e. standard deviation divided by the mean wind velocity) of 0.67 % is used at the inlet of the domain. Different yaw angles, β , have been analysed. Simulations have been carried out for yaw angles between 0° and 90°, with increments of 15°. Similar to the wind tunnel experiments, a uniform effective velocity, U_∞ , of 9.91 m/s is applied for all different yaw angles, β . The velocity in the main inlet direction, U_x , and in the crosswind inlet direction, U_y , is calculated by:

$$U_x = U_\infty \cos(\beta), U_y = U_\infty \sin(\beta). \quad (1)$$

A Reynolds number of 8.9×10^5 is used based on the effective wind velocity and the height of the cyclists from the ground. To enable to compare the results with the wind tunnel results, stationary ground and wheels have been simulated. No slip-boundary conditions have been given to the surface of the model and the ground. Free slip velocity boundary conditions are applied on the sides and upper walls.

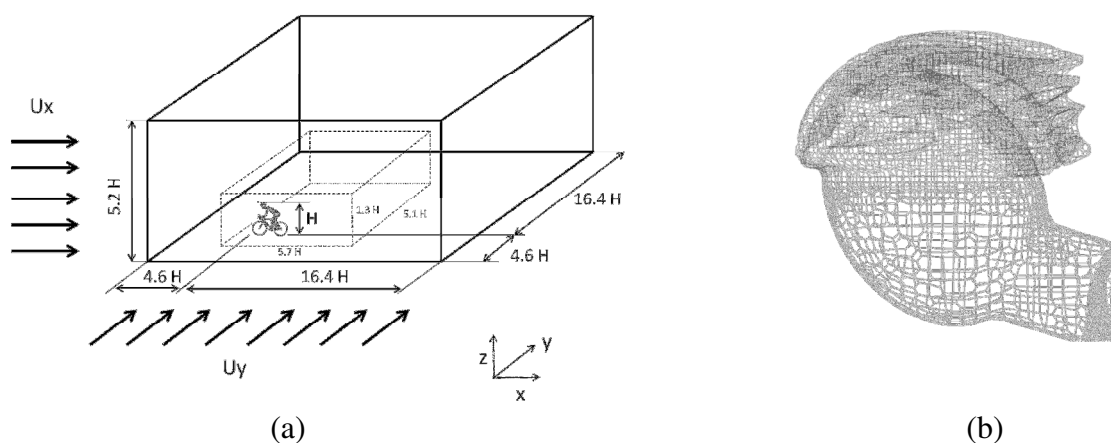


Figure 2: (a) Computational domain, (b) surface mesh of cyclist

All simulations have been performed in OpenFOAM. The steady state SIMPLE algorithm is implemented in the simulations to couple the pressure and the velocity. In all simulations an incompressible flow is assumed. The simulations have run on 32 processors on the BlueBEAR (Birmingham Environment for Academic Research) in parallel.

3 Results and discussion

In this section, the mesh dependency, the aerodynamic coefficients and flow structures around the cyclists at different yaw angles is explored. The flow structures are visualised with Ensign. All results are from the fine RANS simulations unless otherwise stated.

Mesh dependency

To attain a mesh independent mesh, the aerodynamic forces of the different meshes are compared. The aerodynamic forces are usually expressed by force coefficients. The drag force coefficient C_D , side force coefficient C_S and lift force coefficient C_L , are defined by:

$$C_D = \frac{F_D}{0.5A\rho U_\infty^2}, C_S = \frac{F_S}{0.5A\rho U_\infty^2}, C_L = \frac{F_L}{0.5A\rho U_\infty^2}, \quad (2)$$

where ρ the air density (kg/m^3), A the total frontal area of the cyclist and bicycle at 0° yaw angle (0.55 m^2), U_∞ the effective flow velocity (m/s), and F_D , F_S and F_L respectively the drag force, side force and lift force (N). The aerodynamic force coefficients as function of grid size are shown in Table 1. A small error difference of 4.3 % is obtained in the drag force coefficient results from the medium and fine mesh.

Table 1: RANS aerodynamic force coefficients for RANS k- ϵ simulations at $\beta=0^\circ$. Error percentage of the simulation results compared to the fine simulation results and the experimental data. The error is defined as: Value- Reference value / Reference value.

| | | C_D | C_S | C_L |
|-------------|--------------|-------|--------|-------|
| Coarse | Value | 0.638 | 0.000 | 0.102 |
| | % Error Fine | 15.1 | -100.0 | 14.6 |
| | % Error Exp. | 4.4 | -100.0 | -30.6 |
| Medium | Value | 0.578 | 0.040 | 0.075 |
| | % Error Fine | 4.3 | -14.9 | -15.7 |
| | % Error Exp. | -5.4 | -14.9 | -49.0 |
| Fine | Value | 0.554 | 0.047 | 0.089 |
| | % Error Exp. | -9.3 | 0.0 | 39.5 |
| Experiments | Value | 0.611 | 0.047 | 0.147 |

In addition, the surface pressure of the cyclist at a height of $0.7H$ is obtained from the coarse, medium and fine mesh as shown in Fig. 3. The pressure distribution is expressed in terms of the local pressure coefficient C_p . The C_p is defined as:

$$C_p = \frac{p - p_\infty}{0.5 \rho U_\infty^2}, \quad (3)$$

where p is the local pressure, p_∞ the free stream pressure and ρ the air density. The good agreement (RMSE = 0.12) between the results obtained from the fine and medium meshes suggest that the fine mesh simulation accurately predict the flow and no further mesh refinement is needed.

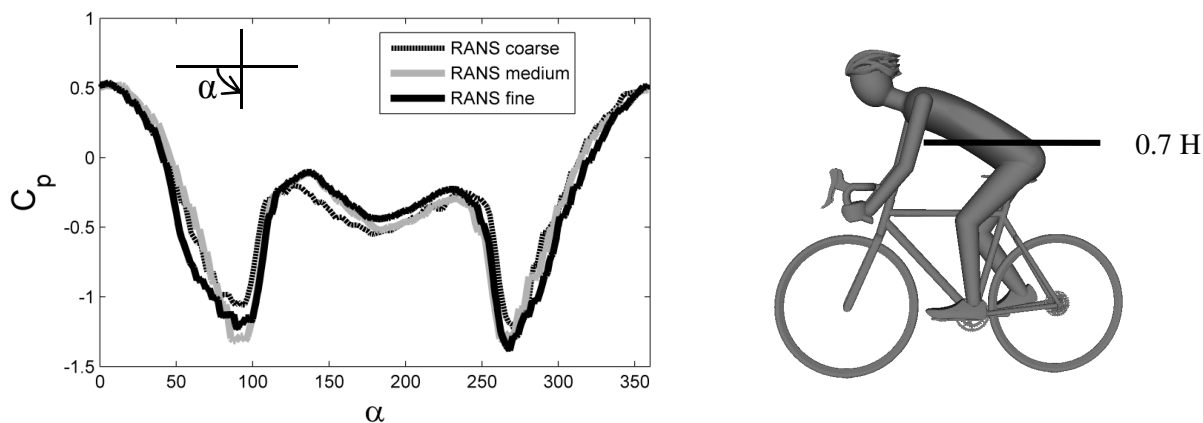


Figure 3: Pressure distribution around the surface of the main body of the cyclist obtained from the coarse, medium and fine mesh RANS k- ϵ simulations at $\beta=0^\circ$.

Aerodynamic force coefficients

The aerodynamic force coefficient at different crosswind angles is shown in Fig. 4. At full head wind, i.e. $\beta = 0^\circ$, the drag force coefficient is around 0.55. A peak drag coefficient is found at $\beta = 15^\circ$, after which the drag force coefficient constantly decreases. The increase in drag force from $\beta = 0^\circ$ to $\beta = 15^\circ$ is caused by the increase of frontal area and the less aerodynamic shape of the cyclist. The

side force coefficient gradually increases with yaw angle. The lift forces are compared to the side forces up to 37 times smaller and therefore excluded from consideration.

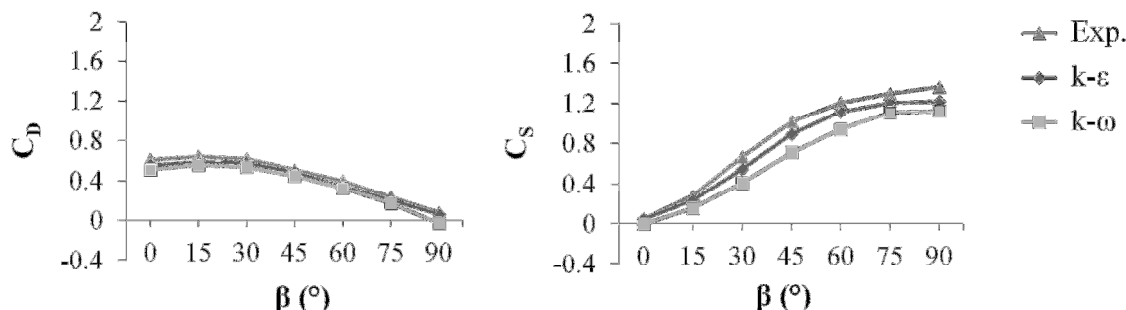


Figure 4: Aerodynamic force as function of yaw angle with mannequin in 24° torso angle position of the experiments and the k-ε and k-ω turbulence models.

The error of the CFD results with the wind tunnel results is expressed as a relative percentage difference:

$$Pct = \frac{AC_{i,CFD} - AC_{i,wt}}{AC_{i,wt}}, \quad (4)$$

where $AC_{i,CFD}$ is the aerodynamic force coefficients of the CFD simulations in all i directions and $AC_{i,wt}$ the measured wind tunnel force coefficients in all directions. The results of the comparison of the force coefficients of the CFD simulations and the wind tunnel experiments are shown in Fig. 5. The smallest difference in simulation results are found with the k-ε model in all analysed force directions. Both two-equation RANS turbulence models slightly underestimate the total drag force and side force coefficient. The average difference percentage in drag for yaw angles $\beta = 0 - 45^\circ$ is -7 % for the k-ε model and -13 % for the k-ω model. The side force differences in the yaw angle range $\beta = 45 - 90^\circ$ are -9 % and -21 % for respectively the k-ε and k-ω model.

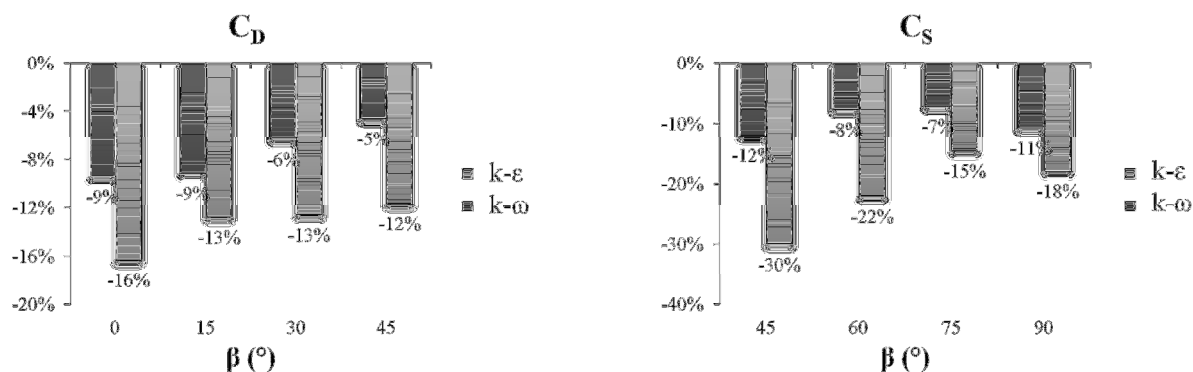


Figure 5: Relative percentage difference aerodynamic drag force and side force coefficient of the RANS k-ε and k-ω simulations.

In the RANS simulation results, a distinction is made between the pressure forces and skin friction forces. The skin friction is caused by the viscous pressure in the boundary layer around the bicycle and cyclist. In the RANS simulations approximately 3 % of the total drag forces contribute to skin drag versus 2 % of the total side forces. This relatively low viscous forces are comparable with that of an isolated cyclist [1] and might be caused by the smooth surface roughness of the cyclist model. It

could be therefore expected that the predicted viscous forces in the simulations are higher in the wind tunnel experiments, where the cyclists' surface was not perfectly smooth. However, the total experimentally recorded drag is only around 10 % higher compared to the simulation results and therefore it is likely that this effect is limited.

Pressure distribution

The pressure distribution over the surface of the geometry in different crosswind angles is shown in Fig. 6. A low pressure area develops at the back of the cyclist by increasing yaw angles, while high pressure regions are developing on the upper lower limbs and the abdomen. At full side wind ($\beta = 90^\circ$), high pressure areas at the wind ward side of the cyclist are present, while low pressure regions develop on the back of the cyclist and the leeward side of the cyclist.

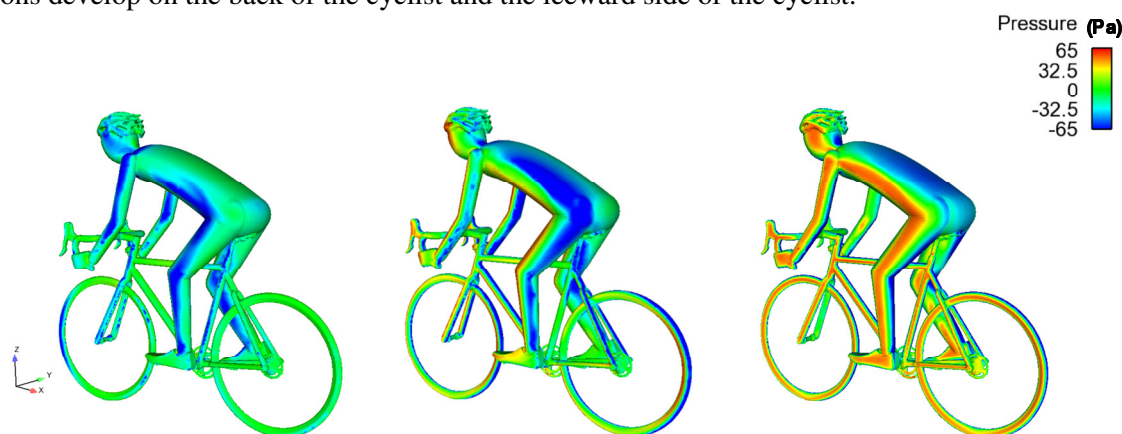


Figure 6: Pressure distribution on the surface of the cyclist in different crosswind yaw angles of the RANS standard $k-\epsilon$ turbulence model: (a) $\beta = 0^\circ$, (b) $\beta = 45^\circ$ and (c) $\beta = 90^\circ$.

Pressure contour lines

Fig. 7 shows the pressure contour lines on the cyclist in head wind ($\beta = 0^\circ$). The mean stagnation points can be found on the head (S1), the shoulders (S2), the pelvis (S3), the hands (S4) and the ankles of the cyclist (S5). The stagnation points are moving to the wind ward side of the cyclist with increasing yaw angles.

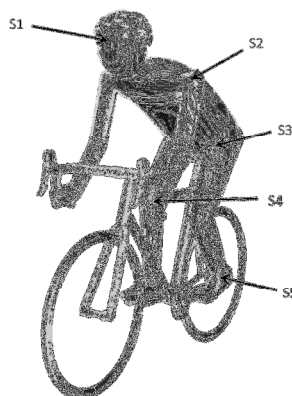


Figure 7: Pressure contour lines on the cyclist surface in case of head wind ($\beta = 0^\circ$) of the RANS standard $k-\epsilon$ turbulence model. Mean stagnation points are found on the head (S1), shoulders (S2), pelvis (S3), hands (S4) and ankles (S5) of the cyclist.

Vortex cores analysis

The vortex cores of the flow around the cyclists are found by means of Eigen analysis. This method is based on an algorithm of Sujudi and Haines (1995). The location of the vortex for two different yaw angles, i.e. 0 and 60°, is shown in Fig. 8. In case of a crosswind yaw angle of $\beta=0^\circ$, the helmet, bicycle and legs mainly contribute to the vortex generation in the flow, while the upper body does not create swirl to the flow. With increasing yaw angles, it should be noticed that the vortex cores move from the back of the cyclists towards the side of the cyclist. At large crosswind angles, practically all vortex cores are in the direction of the main flow.

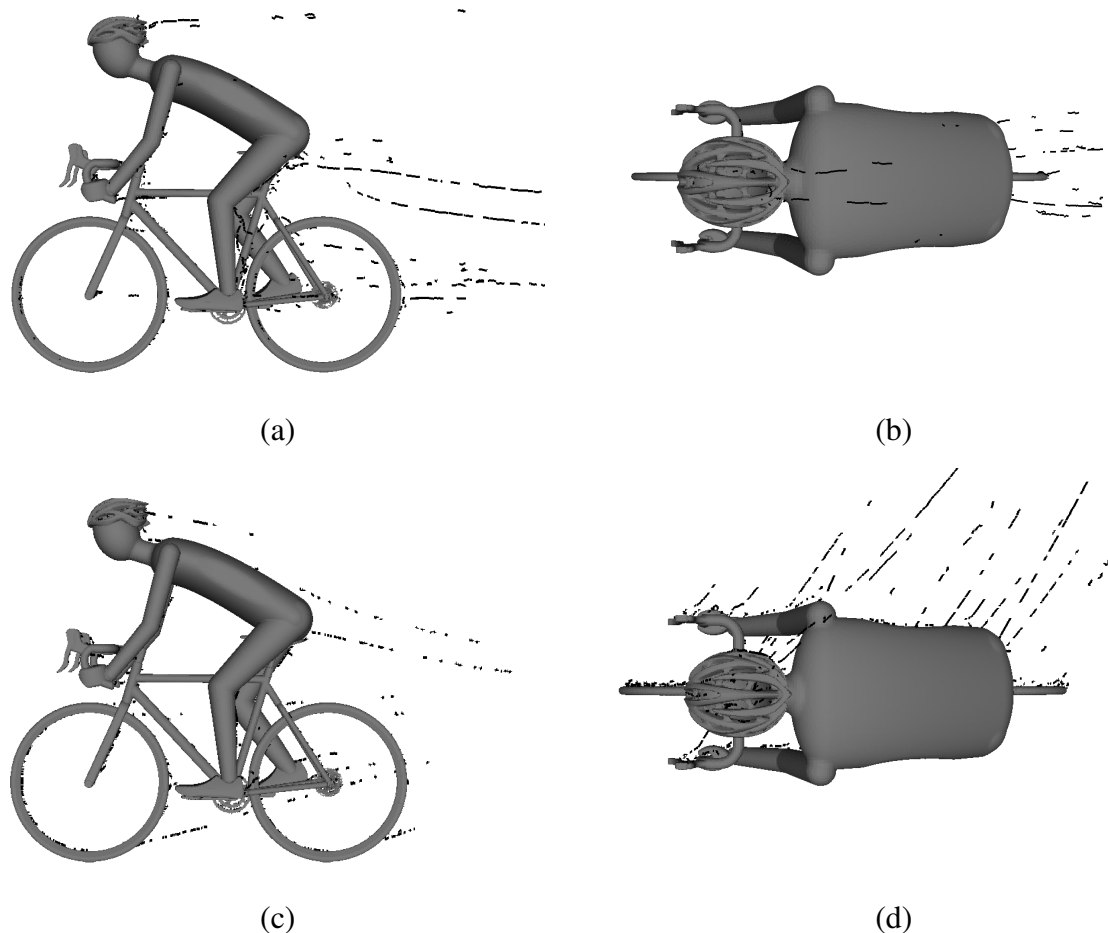


Figure 8: Location of the vortex cores in the flow around a cyclist: (a) $\beta=0^\circ$ side view; (b) $\beta=0^\circ$ top view; (c) $\beta=60^\circ$ side view; (d) $\beta=60^\circ$ top view

Isosurface around cyclist

The isosurface around the cyclists at $C_p = -0.240$ at different crosswind angles is shown in Fig. 9. The isosurface is mainly attached to the cyclist at this pressure. In the case of 60° side wind yaw angle,

besides the cyclist's body also a pressure surface is located at the leeward side of the entire bicycle. This flow characteristic is caused by the slender body of the bicycle.

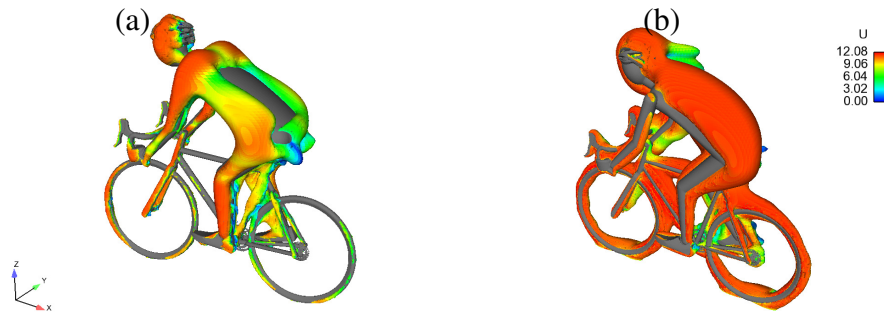


Figure 9: Isosurface of the time averaged pressure at $C_p = -0.240$ at different yaw angles; (a) $\beta=0^\circ$; (b) $\beta=60^\circ$

4 Conclusions

Two RANS simulations have been employed for a cyclist on a bicycle in different crosswinds. The results showed that crosswind has a significant effect on the aerodynamic force coefficients. Good agreement has been found between the trend of the CFD results and the experimental data across a wide range of yaw angles. Both the $k-\epsilon$ and $k-\omega$ RANS turbulence models under-predict the aerodynamic forces, likely caused by discrepancies in surface friction. The flow structures have been identified and the aerodynamic coefficients have been obtained. Future research will involve investigating the effect of time varying wind and the implications on the stability of cyclists and improving the CFD model by using time varying solver, large-eddy simulations.

References

- Defraeye, T., Blocken, B., Koninckx et al. 2010. Computational fluid dynamics analysis of the cyclist aerodynamics: Performance of different turbulence-modelling and boundary-layer modelling approaches. *Journal of Biomechanics*, **42** (12), 2281-2287.
- Great Britain. Department of Transport, 2012. Reported Road Casualties in Great Britain: Main Results 2011, Statistical Release.
- Griffith, M., Crouch, T., et al. 2012. Elite Cycling Aerodynamics: Wind Tunnel Experiments and CFD. In: *18th Australasian Fluid Mechanics Conference*, Launceston, Australia.
- Hanna R.K. 2002. Can CFD make a performance difference in sport? *The engineering of sport 4*. Blackwell Science Ltd.
- Lukes, R.A., Chin, S.B., et al. 2004. The aerodynamics of mountain bicycles: the role of computational fluid dynamics. *The engineering of sport 5*. International Sports Engineering Association.
- Sujudi, D., Haimes, R. 1995. Identification of Swirling Flow in 3-D Vector Fields. Technical Report AIAA-95-1715, American Institute of Aeronautics and Astronautics.

Detached-eddy simulation of the slipstream of an operational freight train

Dominic Flynn, David Soper, Hassan Hemida & Chris Baker

¹School of Civil Engineering, University of Birmingham, UK.

dcf147@bham.ac.uk

Abstract

With increasing train speeds the subsequent increase in slipstream velocities can have a detrimental effect on the safety of persons within a close proximity to the vehicle. The highly turbulent non-stationary slipstream of a model-scale Class 66 locomotive is investigated using delayed detached-eddy simulation (DES). Good agreement was seen between the present work and model-scale physical experiments. Slipstream velocities along the train side were investigated with the bogie region producing the highest slipstream velocities.

1 Introduction

The UK government aims to double the volume of cargo transported by freight trains on the UK rail network by 2030 (DFT, 2007). The increase in traffic volume on the network can be supported in several ways: building new lines, re-opening old lines, increasing train length or train speed. The first two options are expensive would take several years to complete. Route capacity could be increased by lengthening freight trains, although this could lead to slower moving trains congesting the already full lines. The final option of increasing the operational speed of freight trains would be a much simpler option to increase route capacity; though there are associated aerodynamic consequences.

When a train moves through the air it generates a slipstream that is characterised by a high-turbulent non-stationary region of air. To a static observer the slipstream appears as gradually-building gust punctuated with pulses of higher speed air. These air pulses are caused by gaps in the geometry of the vehicle and are generally much larger for freight trains than for passenger trains, therefore causing much larger pressure and velocity transients.

Slipstreams are recognised as posing a risk to the stability of persons and being capable of moving objects on platforms: an assessment of the risks posed by the slipstreams of freight and passenger trains was conducted by RSSB (Pope, 2006). The project collated previously collected slipstream data although due to a great deal of scatter in the data the drawing of solid conclusions was prevented.

The present work uses the open-source software, OpenFOAM (Open Foundation, 2012) to conduct a delayed detached-eddy simulation (DDES) in order to investigate the flow properties and behaviour of the slipstream of a 1/25th scale model freight train. The simulation is validated against the physical experiments of Soper et al., (2013) in order to elucidate the nature of the flow field around the freight train.

2 Model description

The freight train used in the present work is a 1/25th scale Class 66 locomotive with 4 fully-loaded FEA type B container wagons in tow; rails are also included in the simulation.

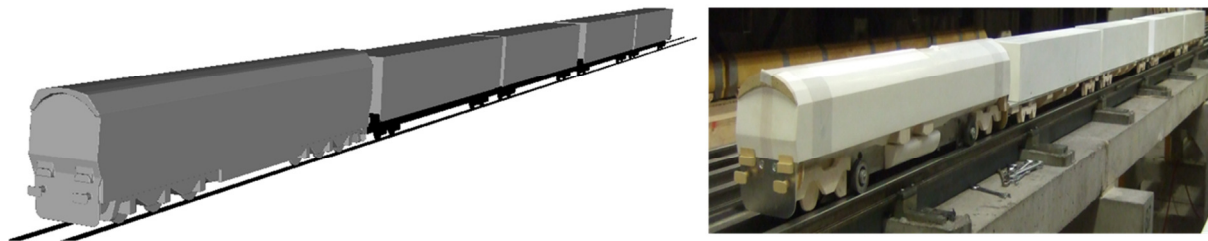


Figure 1: Comparison between train models used in the numerical and physical experiments

3 Computational domain and boundary conditions

The computational domain used in the present work is shown in Figure 2. The simulation replicates the relative movement between the train and the ground by specifying a no-slip moving-wall boundary condition for the ground plane and rails with the same velocity as the inlet. By holding the train in a fixed reference frame, the correct relative movement between the train and the ground is achieved without the need for complex methods such as sliding meshes.

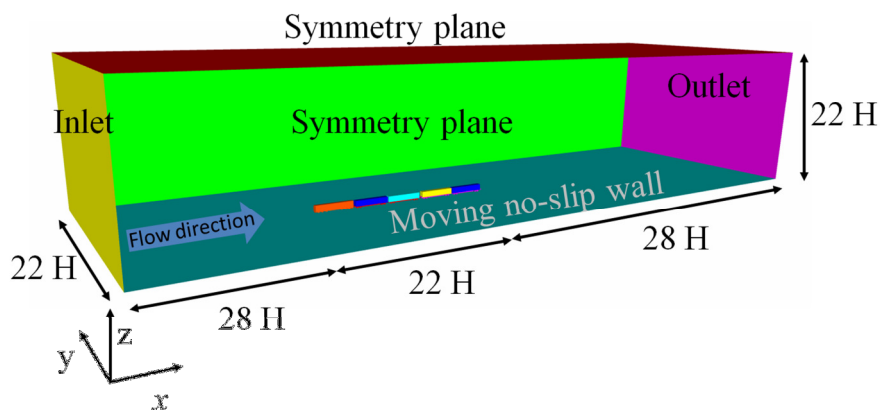


Figure 2: Computational domain and boundary conditions

4 Numerical schemes

The convection terms were discretised using a blended central differencing scheme with 5% upwinding to aid stability. Time integration was conducted using a second order backward implicit scheme and time steps were kept at $\Delta t = 3 \times 10^{-6}$ s in order to prevent the maximum Courant number from exceeding 2. The high computational cost associated with such small time steps is compensated by the resolution of the high frequency/small-scale structures in the flow.

5 Computational mesh

The computational mesh used in the present work is an unstructured hexahedral grid. The entire computational mesh consisted of 38 million cells: 400,000 cells on each container wagon and 600,000 cells on the locomotive. The mesh is dominated by hexahedral cells but other polyhedral elements are also present due to the complexity of the geometry (Figure 3). The quality of the mesh was verified

using mesh metrics within OpenFOAM and it was ensured that the maximum skewness of every cell was below 4 and maximum non-orthogonality was less than 60.

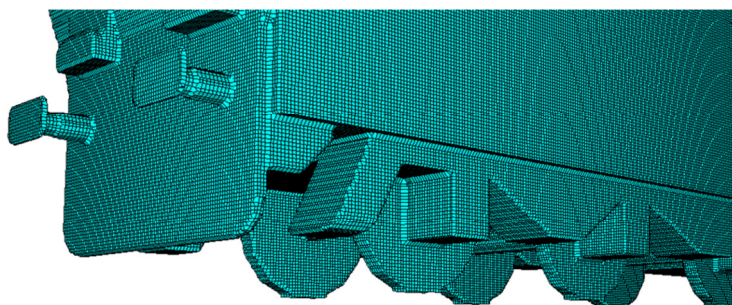


Figure 3: Surface mesh on the complex geometry of the Class 66 locomotive

6 Results

To ensure the validity of the numerical results a comparison was made to the experimental data. Comparison between the pressure and velocity for the physical and numerical experiments is seen in Figure 4, there is a good agreement with the experimental work. The poorest agreement for the slipstream velocity occurs in the latter half of the slipstream ($x=60-100$ m). It is unclear why there is such a large discrepancy for $x > 60$ m, it is possible that it is due to minor differences in experimental procedures for the physical and numerical cases.

Upstream of the train ($x < 0$ m) noise in the experimental velocity and pressure signals is observed. It is likely that this noise is a result of vibration in the experimental equipment.

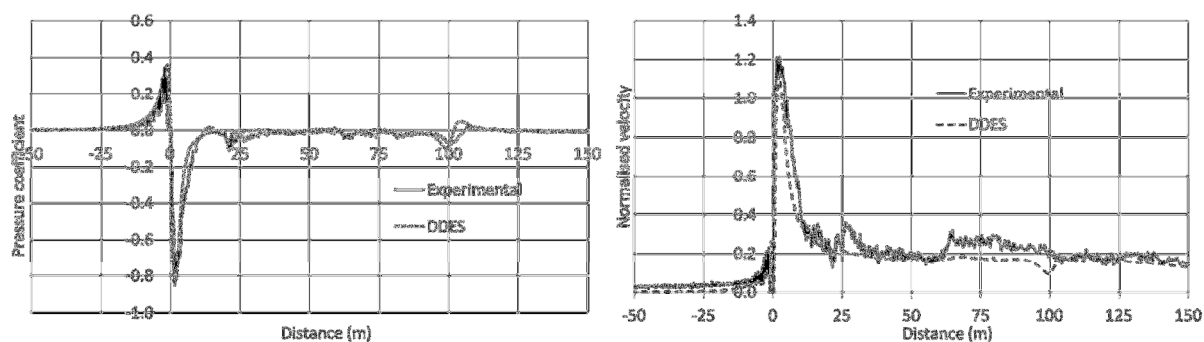


Figure 4 Time and ensemble-averaged pressure coefficients and u components of velocity at probe position 2 for the numerical and experimental results, respectively.

Figure 5 shows the variation of slipstream velocity magnitude at the side of the train. The maximum velocities in the slipstream are always observed near the train nose, $x \approx 0$ m. The blunt front of the Class 66 locomotive causes the flow to shear around the sharp corners and accelerate in much the same way that it would around any cuboid. The highest peak velocity is observed at $z=2.0$ m (i.e. at approximately mid-height of the locomotive) and is likely to be a consequence of the rear-sloped front of the locomotive causing the air to accelerate upwards thus increasing the vertical component of velocity.

The velocity transients in the slipstream are due to the presence of inter-wagon spacings. The spacing between the second and third wagon is the largest and hence it is responsible for the greatest velocity

peaks ($x=60$ m) in the slipstream, after the nose peak. Similar, but smaller, peaks are observed at $x=21$ m, $x=40$ m and $x=80$ m and are due to inter-wagon gaps that are $1/3^{\text{rd}}$ of the largest inter-wagon spacing.

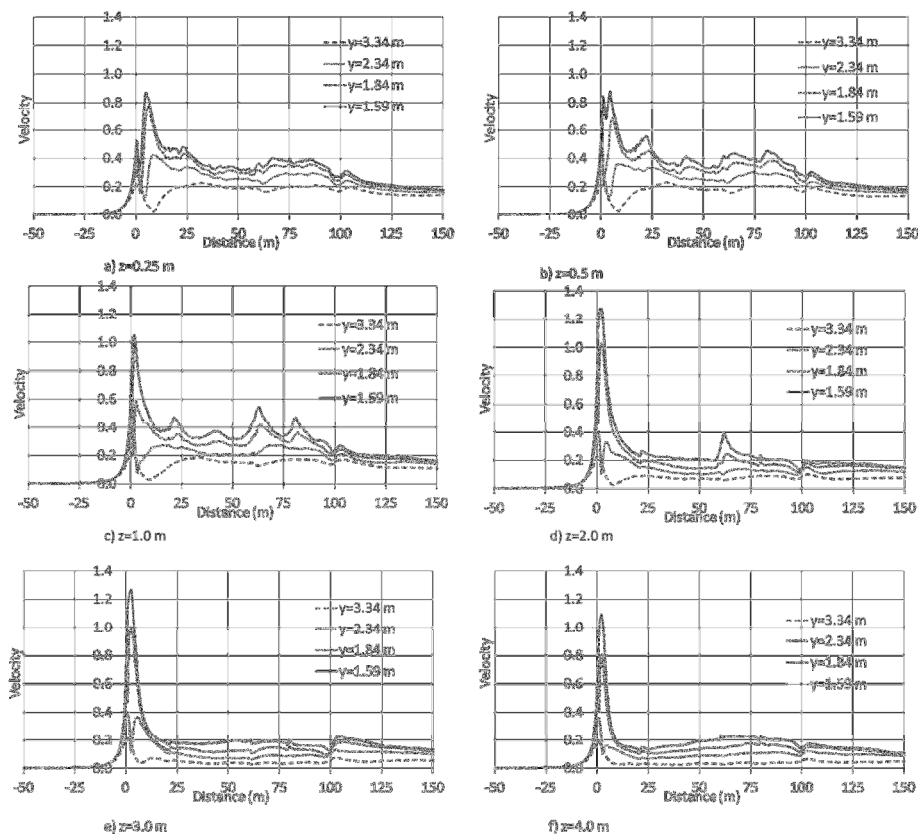


Figure 5: Normalised slipstream velocity magnitude at distances from the centre of track and at varying distances above top of rail (TOR) (a) $z=0.25$ m, (b) $z=0.5$ m, (c) $z=1.0$ m, (d) $z=2.0$ m, (e) $z=3.0$ m and (f) $z=4.0$ m.

An increase in slipstream velocity is observed at the top of the container wagons (Figure 5f). The increase in velocity is associated with a growth of the slipstream which has been shown to occur at full-scale (Sterling et al., 2008), although the present train is too small to determine how long it would continue to grow for.

References

- DFT 2007. Delivering a sustainable railway. In: TRANSPORT, D. F. (ed.).
 OPEN FOUNDATION. 2012. *OpenFOAM 2.1.0 User Guide* [Online]. [Accessed 10/09/2013 2013].
 POPE, C. 2006. Safety of Slipstreams Effects Produced by Trains. A report prepared by Mott Macdonald Ltd for RSSB.
 SOPER, D., BAKER, C. & STERLING, M. 2013. The aerodynamics of freight trains. *International Workshop on Train Aerodynamics*. Birmingham University.
 STERLING, M., BAKER, C., J., JORDAN S., C. & JOHNSON T. 2008. A study of the slipstreams of high-speed passenger trains and freight trains. *Proceedings of the Institution of Mechanical Engineers, Part F: Journal of Rail and Rapid Transit*, 222, 177-193.

Derivation of Enhanced Interatomic Potentials for Thorium Dioxide (ThO₂): a Potential Nuclear Fuel

C L.Green¹ and M S.D. Read¹

¹School of Chemistry, University of Birmingham, UK.

cxg210@bham.ac.uk

Abstract

Existing interatomic potentials published for Thorium dioxide have so far been insufficient in modelling all aspects of the material to an acceptable level; some unable to predict the bulk properties or defect properties accurately. A novel method of derivation of interatomic potentials has been employed to calculate a set of potentials that can describe the Thorium-oxygen interaction accurately over the entire region of interest. The potential set will provide an initial platform from which the material can be studied and assessed as to its suitability as an alternative nuclear fuel.

1 Introduction

The use of nuclear power to fulfil the world's energy needs is becoming more popular as the stocks of fossil fuels are quickly depleting; The Nuclear energy institute [1] recorded 30 countries worldwide to be operating nuclear fuel plants in 2012 with 14 countries in potential construction of new power plants. Nuclear power is also considered to be a cleaner energy alternative as no CO₂ gases are released into the environment but in the nuclear fuel cycle other transuranic materials are produced as waste products. Research into the nuclear power industry has been plentiful for many years trying to find ways to improve the current methods.

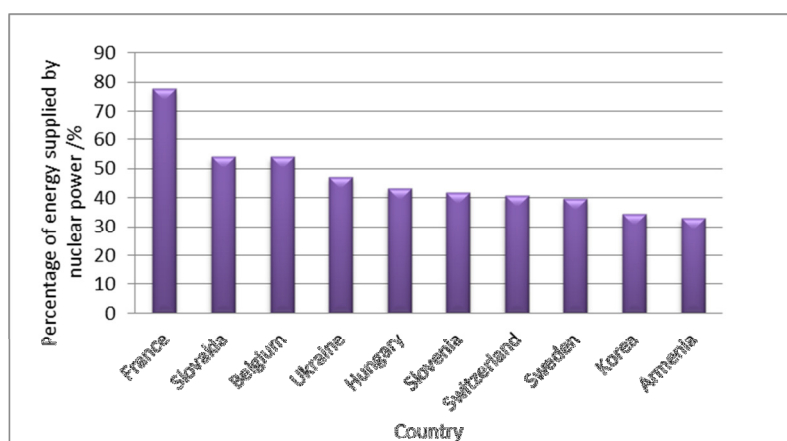


Figure 1: Countries that use nuclear power to supply over a quarter or more of their needs using nuclear power (2011). [1]

Uranium and Uranium/Plutonium mixed fuels are currently the most widely used fuels in power stations around the world but as the stores of Uranium are also getting low the research has turned to new potential fuels. The Uranium/plutonium fuel cycle has provided energy for the world quite

sufficiently for many years and therefore finding a material that can replace these fuels must have many benefits; such things as cost, abundance, performance in higher burn up, environmental factors, waste factors and resistance to proliferation.

Thorium dioxide has been investigated and discussed as a potential nuclear fuel for many years [2, 3] and has even been trialled in some countries; India is currently planning on building their first advanced heavy water reactor that will use Thorium as the bulk of the fuel [4].

Thorium is four times more abundant in the earth's crust than uranium and the Thorium process itself has many benefits over the Uranium fuel cycle; it produces much less transuranic waste as less plutonium is produced and the cycle can consume waste plutonium and other actinides. This reduces the problems of waste management and proliferation.

Computational studies of Thorium dioxide have been plentiful along with experimental studies to investigate Thorium dioxide as a nuclear material. Studies include crystal properties such as lattice parameters and lattice energies, elastic properties such as bulk modulus and elastic constants and also studies as to how the material will react under pressure, temperature and radiation using XRD, neutron diffraction and many other techniques.

Published interatomic pair potentials have been reviewed for their sustainability in reproducing both the structural, physical and mechanical properties of thorium dioxide. It is vital that at the computational level the material is modelled correctly so that as the research moves onto experimental all of the predications are correct. Therefore, a set of interatomic potentials has been derived using a novel fitting procedure in order to improve the understanding of ThO₂ and its characteristics.

2 Computational techniques

2.1 Empirical potentials and lattice properties

The general utility lattice program (GULP) [5] was used throughout this investigation to complete all the calculations.

To be able to describe a model accurately all of the interactions between the atoms within the crystal must be considered. The calculations are performed using the Born-model in which the total energy is partitioned into two interactions; the long range and short range interactions. The short range interaction can be represented by the Buckingham equation shown in equation 1.

$$\phi^{Buckingham}_{(rij)} = A_{ij} \exp\left(-\frac{rij}{\rho_{ij}}\right) - C_{ij}r_{ij}^{-6} \quad (1)$$

Where A , ρ and C are the potential parameters that represent the interactions between the atoms i and j and r is that distance between the atoms.

Another form of the Buckingham potentials is used to describe the anion-anion potential used within this investigation. The Buckingham four range (equation 2) form of the potential and it is used to eliminate the unphysical attraction between the ions at close range by applying the potential over specific intervals.

$$V_{\text{Buck-4}}(r_{ij}) = \begin{cases} A_{ij} \exp(-r_{ij}/\rho_{ij}) & \text{if } r_{ij} \leq r_1 \\ \text{5th order polynomial} & \text{if } r_1 < r_{ij} \leq r_{\text{min}} \\ \text{3rd order polynomial} & \text{if } r_{\text{min}} < r_{ij} \leq r_2 \\ -C_{ij}/r_{ij}^6 & \text{if } r_{ij} > r_2 \end{cases} \quad (2)$$

2.2 The shell model

The shell model [6] is applied as it accurately describes the electronic polarization of the model and is beneficial when investigating the defects within a crystal. The shell model describes the interactions in such a way that the ion charge is partitioned between the core and the shell. The core and shell are screened from each other but connected by a harmonic spring with a spring constant (K_2).

2.3 Defect properties

Defect properties of nuclear fuels are very important as they will be subject to both doping and radiation damage. To describe the defect accurately the Mott Littleton approach is used [7]. This model separates the area surrounding the defect into regions in which the outer atoms are contained. The atoms in region 1 are relaxed explicitly as they are the most effected by the defect and the atoms in region 2a are less affected by the defect and can be treated as dielectric continuum in which the ions interact with a net charge from the defect.

3 Discussion of results

The ThO₂ crystal adopts a fluorite structure ($Fm\bar{3}m$) with a lattice constant of 5.6001Å [8]. The bonding within the system is predominantly ionic with the thorium atoms occupying the face centred position and the oxygen's positioned at the tetrahedral sights.

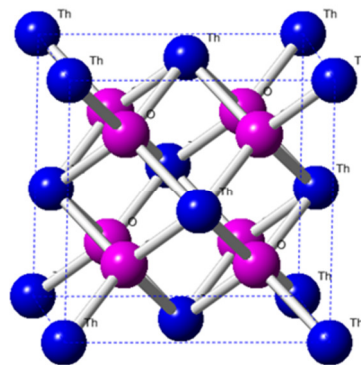


Figure 2: Observed crystal structure for ThO₂

3.1 Derivation of interatomic potentials

Bahera *et al.* [9] provide a detailed review of existing Thoria potentials in which they compare the potentials ability to model the bulk properties such as defect properties and surface properties. In order for the potential set to be considered suitable the difference between all predicted properties experimental observation should be as small as possible. Therefore the potential set must be as

accurate as possible. In order to derive a suitable set of potentials that are able to model the structure perfectly a very detailed fitting method must be applied. The method described within this work has been previously successfully used by Read *et al.* [10] to derive a set of potentials to describe UO_2 .

3.1.1 The anion-anion potential

The anion-anion potential used throughout this work is that of Lewis and Catlow [11]. This potential has previously been used successfully in modelling both UO_2 [10] and ThO_2 [12].

Table 1.0: Buckingham four range potential set for the anion-anion interaction.

| Interaction | A /eV | p /Å | C /eVÅ ⁻⁶ | Y e | K_2 /eVÅ ⁻² |
|-------------|---------------|----------|------------------------|----------|--------------------------|
| | 11,272.6 | 0.1363 | 134.0 | -4.4 | 296.2 |
| O- O | r_{\min} /Å | Cut 1 /Å | r_{\min} /Å | Cut 2 /Å | r_{\max} /Å |
| | 0.0 | 1.2 | 2.1 | 2.6 | 15.0 |

Where Y is the charge on the ion, K_2 is the spring constant and r_{\max} is the cut-off point.

3.1.2 The cation-anion potential

As the Buckingham four-range potential cannot be applied to the cation-anion potential, due to the absence of a stationary point within the function, the C term must be set to zero so that the unphysical attractive forces at short distances can be avoided. This provides a Born-Mayer form of the potential in which only the A and p terms are used to describe the material.

The derivation process begins with the screening of a set of A and p values in which a solution set is produced. The solution set will show the combinations of the potentials A and p that will give the lattice constant closest to the observed value.

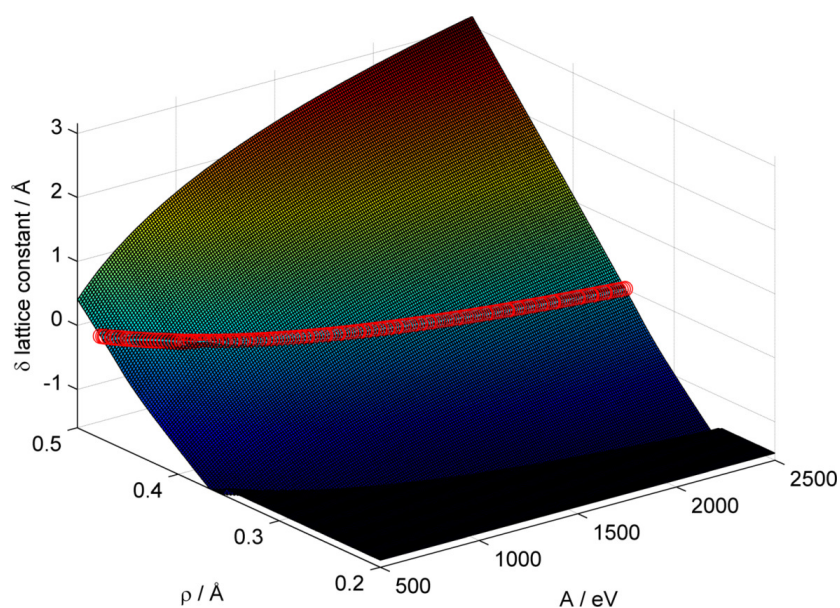


Figure 3: Surface plot representing the difference between the A and p and the observed Th-O lattice constant.

The solution set is then screened once again to fit to bulk properties. Elastic constants are used as they describe the response of the lattice with respect to deformation of the material. As the material is cubic symmetry reduces the unique elastic constants to C_{11} , C_{12} and C_{44} .

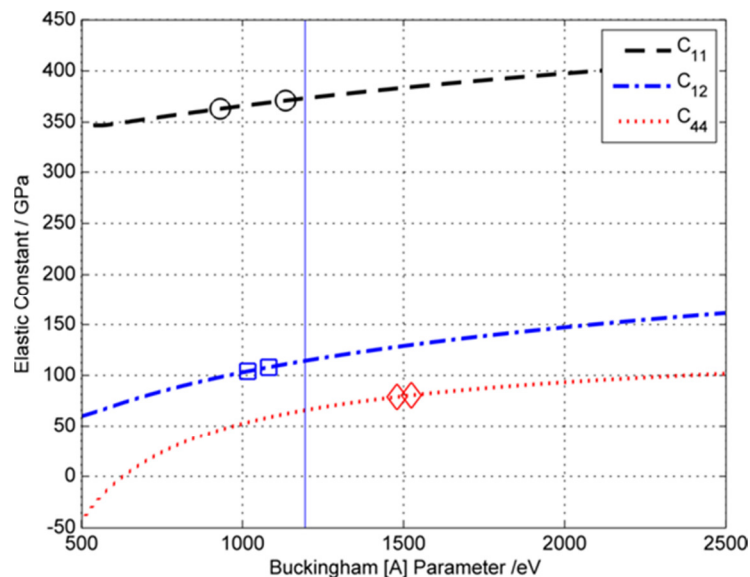


Figure 4: Predicted and experiential elastic constants plotted against the potential paraeter (A).

Due to the value of C_{44} showing a significant difference in value three approaches were taken to try to fit the elastic constants as best as could be done resulting in three sets of potentials (Shown in table 2.0).

Table 2.0: Three sets of Buckingham potentials for the Cation-anion interaction.

| | A /eV | $p / \text{\AA}$ | C /eV \AA^{-6} | Y e | $K_2 / \text{eV}\text{\AA}^{-2}$ |
|-------|-----------|------------------|-------------------------|-------|----------------------------------|
| Set 1 | 1394.4724 | 0.3861 | 0.00 | -2.54 | 91.9415 |
| Set 2 | 1047.7387 | 0.4078 | 0.00 | -2.54 | 129.5660 |
| Set 3 | 1193.9986 | 0.3975 | 0.00 | -2.54 | 105.7408 |

Where Y is the charge on the ion and K_2 is the spring constant.

The next step involved adjusting the spring constant to fit the dielectric properties of the material. This is so that the potentials will perform accurately when calculating defect properties within the structure.

Once the spring constant has been adjusted the potential can be initially validated as to its behaviour under varying temperatures by investigating the changes in lattice constant (A) and the lattice energy.

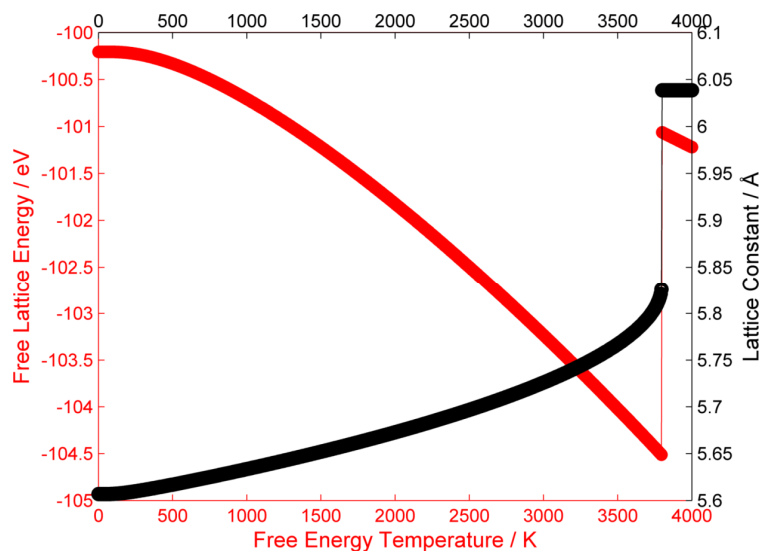


Figure 5: Thermal stability of the potential (set 3)

Investigations into the thermal stability of the potentials conclude that all three of the potential sets are suitable up to 3700K.

3.2 Perfect Lattice properties

The three potentials sets were used to calculate bulk properties of the material including elastic constants, Bulk modulus and dielectric properties. A least squares method was used to determine which potential set was able to reproduce the experimental results the best.

Table 3.0: Born-Mayer potential for the Th-O interaction

| Interaction | A / eV | $p/\text{Å}$ | C / eVÅ ⁻⁶ | Y e | K ₂ / eVÅ ⁻² |
|-------------|-----------|--------------|-----------------------|-------|------------------------------------|
| Th-O | 1193.9986 | 0.3975 | 0.0 | -6.54 | 105.7408 |

The resulting set of potentials is shown in table 3.0 and the bulk properties calculated shown in table 4.0.

Table 4.0: Comparison of calculated and experimental bulk properties

| Property | Observed | Calculated | % Difference |
|--|-------------------|------------|--------------|
| Lattice constant (a_0) / Å | 5.6001 [8] | 5.6001 | 0 |
| Lattice energy / | -104.39 [13] | -100.33 | 4.11 |
| Elastic constants /GPa | | | |
| C₁₁ | 367 ± 4.0 [14] | 373.23 | -1.69 |
| C₁₂ | 106 ± 2.0 [14] | 114.36 | -7.92 |
| C₄₄ | 79.7 ± 0.8 [14] | 65.82 | 17.44 |
| Moduli | | | |
| Bulk | 193 [14] | 200.65 | -3.96 |
| Shear | 95.6-100.6 [14] | 81.93 | 14.30 |
| Youngs | 256,270 [15] | 319.58 | -24.84 |
| Poissons Ratio | 0.279 [14] | 0.23 | -6.64 |
| Dielectric constants | | | |
| Static | 18.9 [16] | 18.1 | 4.23 |
| High frequency | 4.4 [16] | 4.7 | -6.82 |
| Phonons at 298K | | | |
| L mode | 269.2/279 [17,18] | 271.37 | -0.81 |
| T mode | 569.8/567 [17,18] | 425.48 | 25.33 |

Table 4.0 shows the percentage difference between the observed and calculated bulk properties; the excellent agreement over the range of properties shows that the potential is robust and can be used, with confidence, for further calculations.

3.3 Defect properties

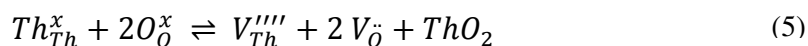
After a robust set of potentials have been determined further investigations can be carried out starting with defect properties. The most basic of defects that can occur within a crystal are point defects. These consist of vacancies and interstitials. The calculated formation energies of these defects within the ThO₂ crystal are listed in Table 5.0.

Table 5.0: Defect formation energies for isolated defects within the ThO₂ unit.

| Defect | Published Formation energy /eV [14] | Coordinate position | Calculated Formation energy /eV |
|-------------------------------------|-------------------------------------|---------------------|---------------------------------|
| Th⁴⁺ vacancy | 84.66 | (0,0,0) | 78.05 |
| O²⁻ vacancy | 15.83 | (0.25,0.25,0.25) | 16.15 |
| Th⁴⁺ Interstitial | -64.86 | (0.5,0.5,0.5) | -59.13 |
| O²⁻ Interstitial | -9.82 | (0.5,0.5,0.5) | -11.06 |

3.3.1 Frenkel and Schottky defects

Vacancy and interstitial defects can be combined to calculate the energy of frenkel and schottky defects within a material.



Equations 3-5 represent the frenkel (3, 4) and schottky (5) defect calculations.

The results are shown in table 6.0 and they suggest that oxygen frenkel pairs are the most favourable defect to form within the structure.

Table 6.0: Frenkel and Schottky energies within the ThO₂ cell (per defect).

| Defect | Experimental formation energy /eV | Calculated formation energy /eV |
|---------------|-----------------------------------|---------------------------------|
| Th Frenkel | 19.8 | 18.916 |
| O Frenkel | 6.01 | 5.092 |
| Schottky trio | 11.93 | 10.020 |

4. Conclusions

A potential set has been derived using available experimental data and a novel method of potential fitting. The potentials were then tested as to their ability to reproduce bulk properties and defect properties of the material.

The potentials showed a very good agreement with experimental data with little percentage difference. The defect calculations also showed good agreement with previously published data and the calculations also showed that oxygen frenkel pairs were the most favourable defect to form.

5. Acknowledgements

The calculations performed within this investigation were performed using the University of Birmingham's BlueBEAR HPC service.

6. References

- [1] Nuclear Energy Institute (2010) 1776 I Street NW, Suite 400, Washington, D.C. 20006-3708 P: 202.739.8000F: 202.785.4019. http://www.nei.org/resourcesandstats/nuclear_statistics/worldstatistics/
- [2] M. Lung, O. Gremm. Perspectives of the Thorium fuel cycle. *Nucl. Eng. Des.* **180** (1998) 133-146.
- [3] S. Peggs, W. Horak, T. Roser, G. Parks, M. Lindroos, R. Seviour, S. Henderson et al. *Proceedings of the international particle accelerator conference. IPAC 2012.*(2012) 29-33.

- [4] Guardian (2012) <http://www.guardian.co.uk/environment/2011/nov/01/india-thorium-nuclear-plant>. Nov 2011
- [5] J.D. Gale and A.L. Rohl, *Mol. Simul.* **29** (2003) 291.
- [6] B.G. Dick and A.W. Overhauser. *Phys. rev.* **112** (1958) 90-103.
- [7] N. Mott and M. Littleton, *Trans. Faraday Soc.* **34** (1938) 485.
- [8] M. Idiri, T. Le Bihan, S. Heathman and J. Rebizant. *J. Phys. Rev. Ser 3; B. Condens. Matter.* **70** (2001) 014113-1-014113-8.
- [9] R. K. Bahera and C. S. Deo. *J. Phys: Condens. Matter.* **24** (2012) 215405.
- [10] M.S.D Read. R.A. Jackson. *J. Nuc. Mat.* **406** (2010) 293-303
- [11] G.V. Lewis and C.R.A. Catlow, *J. Phys. C* **18**, 1149-1161 (1985).
- [12] T. Karakasidis and P. J. D. Lindan. *J. Phys.: Condens. Matter.* **6** (1994) 2965-9
- [13] P. M. Maceado, W. Capps and J. B. Watchman. *J. Am. Ceram. Soc.* **47** (1964) 651
- [14] E. A. Colbourn and W.C. Mackrodt. *J. Nucl. Mater.* **118** (1983) 50-59.
- [15] G.C.Benson, P.I. Freeman and E. Dempsey. *J. Am. Ceram. Soc.* **46** (1963) 43-47
- [16] J.D.Axe and G.D.Pettit. *Phys. Rev.* **151** (1966) 676-680.
- [17] K. Clausen, W. Hayes, J. E. Macdonald, R. Osbourn, P.G. Schnabel, M.T. Hutchings and A. Magerl. *J. Chem. Soc. Faraday. Trans. 2.* **83** (1987) 1109-1112.
- [18] M. Ishigame and M. Kojima. *J. Phys. Soc. Japan.* **41** (1976) 202-10.

Atlas of simulated images for Au₅₅ nanoclusters using multislice method

Nan Jian, Kuo-juei Hu and Richard Palmer

NPRL, School of Physics & Astronomy, University of Birmingham, UK.

Research of nanoclusters is crucial for to understanding of why and how nanostructures are different from bulk materials in many aspects. Their structures have strong connections to their unusual properties. To probe their structures experimentally, we employed aberration-corrected scanning transmission electron microscopy that could provide us with resolution of sub-Angstrom level on these nanoclusters of only from tens to a hundred Angstroms in diameter. However, the structure of clusters cannot be resolved solely by high-resolution images, because STEM images are 2D projections of electron-atom interaction with 3D structure of clusters. To solve this problem, we conduct image simulation based on a multislice method which interaction between electrons and clusters are treated as electron interaction with each slice of the 3D structure individually in orders. We generate simulated images from various directions of the cluster and portrait simulated image atlas for the cluster. We then match each experimental image with a simulated image in the atlas. In this research, we find the positive matches between experimental images of size-selected Au₅₅ clusters and simulated images calculated from a DFT theoretically predicted Au₅₅ chiral model.

A Nano cluster is defined as an aggregation of atoms containing between 2 to 200,000 atoms. Clusters have attracted a lot of research interests due to their sizes and structures, which are between molecular and microcrystalline and are essential for their properties. Now clusters are considered a new kind of nanomaterial. Size-selected clusters are used to etch nanoscale structures for nanofabrication [1], some small clusters are catalysts for chemical reactions [2,3] while some big clusters can be used to mark protein molecules in biology [4].

Au₅₅(PPh₃)₁₂Cl₆ is a very famous cluster due to its unique electronic properties given that it can act as a single electron switch. It has the potential application to be the next generation fast and energy saving electronic switch or transistor [2]. But since it firstly synthesized in 1981, the argument about what structure it has have never been agreed upon. At first Schmid proposed it had a cuboctahedral structure by the molecular weighing that determined the molecular formula and Mossbauer spectra that showed 4 types of Au atoms. Later, the X-ray powder diffraction research showed that the icosahedral structure seemd more likely to be the structure of the Au₅₅(PPh₃)₁₂Cl₆ clusters [5-7]. To investigate the atomic structure of Au₅₅(PPh₃)₁₂Cl₆, aberration corrected High Angle Annular Dark Field Scanning Transmission Electron Microscopy (HAADF-STEM) was used.

Electron microscopy is a powerful tool to characterize the structure of material [8] and make one of the inventors, Ernst Ruska, to win a nobel prize in 1986. A Scanning Transmission Electron Microscope uses an electron source to produce the electron beam to scan over the specimen, a detector under the sample is employed to detect the scattering signal to form an image [9]. By the developing of aberration correction technology, the resolution of an aberration corrected STEM can reach sub-Angstrom now. The HAADF imaging uses a detector to select the high angle scattered electron which can be regard as Rutherford scattered electrons. So the intensity of a HAADF image is directly proportional to Z^n . (Z is atomic number of the object material, n is an index which is determined by each STEM) So HAADF image are also called Z-contrast images.

When the high-resolution STEM images were gotten, how to characterize the clusters' structure would be a problem. An idea is to assume a structure, then simulate the STEM images of it, then check if the real-space STEM images matched with them. If yes, this material should have the same structure of the model. The multislice method is the most popular approach of EM image simulation. The principle of it is to divide the material potential to many slices and projected onto a plane vertical to the observation orientation. Then calculate the first slice's beam diffraction and do the propagation from one slice to another and finally get the wave function of the surface of the material. In our research, a software package called QSTEM that is based on multislice method was used to do the STEM image simulation.

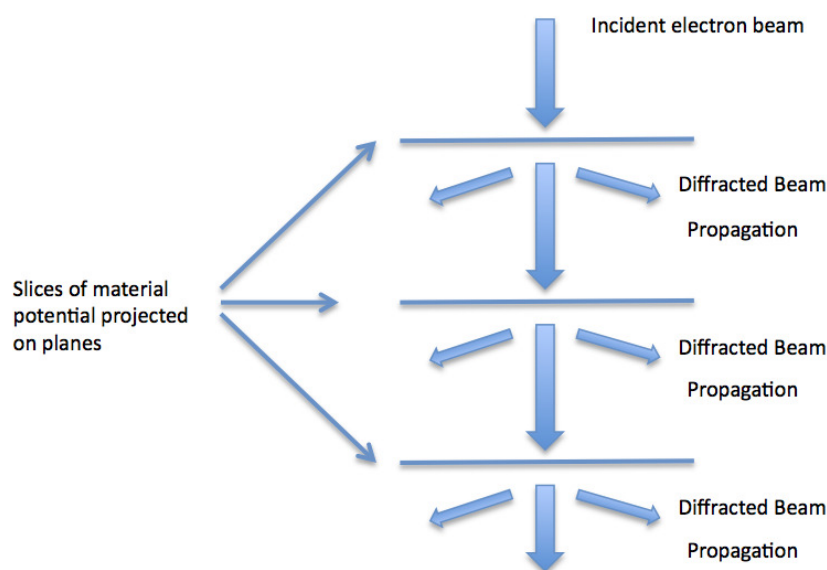


Figure 1: Schematic of multislice method

Although we can simulate the STEM image of nanoclusters, the image can only give us 2D information. To avoid this drawback, we present a simulation atlas which is a set of simulation images from every possible observation orientations. So no matter from which orientation the cluster was imaged, we can find a relevant simulation image to compare with. This approach extremely increases the efficiency of cluster structure characterization. In our research, there are 4 structure models (chiral, cuboctahedral, icosahedral and decahedral) used to simulate the STEM images. There are hundreds of simulation images, so to simplify the comparison work we divide all the simulation images into 7 groups based on their image pattern features. When doing the comparison work, at first, classify the experimental image with their pattern feature, then compare it with its corresponding simulation group, finally find the closest simulation. This will avoid wasting time comparing obviously different images.

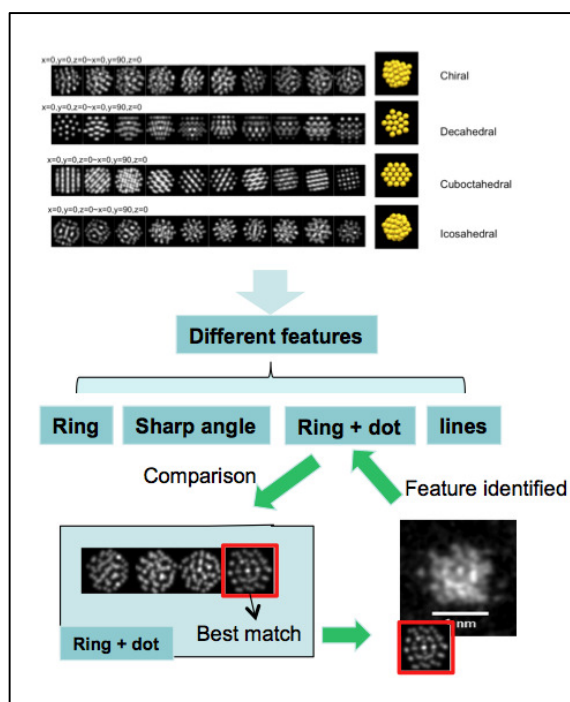


Figure 2 the schematics of the simulation atlas and comparison process

Before characterizing the cluster structure, the cluster weighing is necessary to verify the cluster we investigate is the $\text{Au}_{55}(\text{PPh}_3)_{12}\text{Cl}_6$ cluster. Using the Z-contrast feature of HAADF image, size-selected Au_{309} clusters were used as mass balance to weigh the $\text{Au}_{55}(\text{PPh}_3)_{12}\text{Cl}_6$ cluster. The result showed that the $\text{Au}_{55}(\text{PPh}_3)_{12}\text{Cl}_6$ clusters have 53.38 ± 3.16 Au atoms in average. So they can be considered as $\text{Au}_{55}(\text{PPh}_3)_{12}\text{Cl}_6$ clusters. We also measure the clusters' radius and their aspect ratio. The figure below shows the distribution of their radius and aspect ratios, they have an average radius of 1.405nm which convinced with many previous studies on the $\text{Au}_{55}(\text{PPh}_3)_{12}\text{Cl}_6$ clusters that they have a diameter of 1.4 nm [1-3]. Their aspect ratios are not focus on one peak but last from 1.05 to 1.6. Which shows the clusters do not have a symmetry structure.

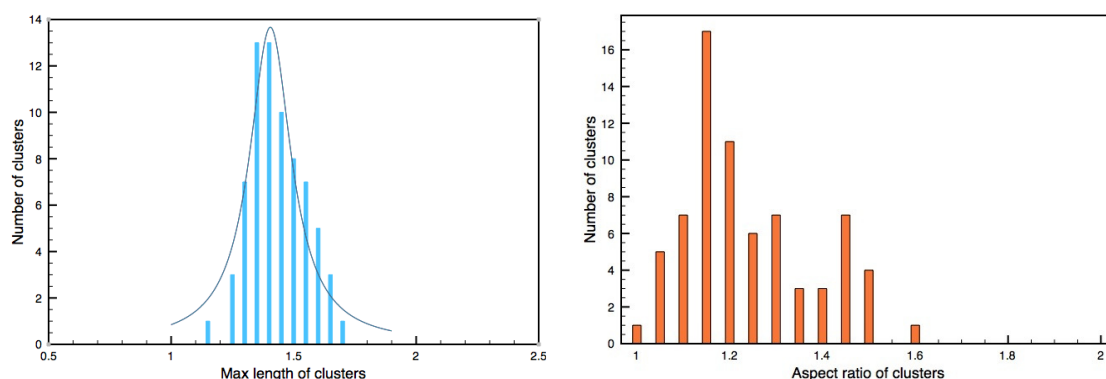


Figure 3 (a) The distribution of the radius of $\text{Au}_{55}(\text{PPh}_3)_{12}\text{Cl}_6$. (b) The distribution of the aspect ratio of $\text{Au}_{55}(\text{PPh}_3)_{12}\text{Cl}_6$.

After the comparison of all 72 clusters that have 55 ± 2.5 Au atoms, there were 38 clusters showed a best match to the chiral structure model simulation. Very few cluster matched the cuboctahedral and

no decahedral and icosahedral have been found. Nearly half of the clusters showed an amorphous structure. This result, combined with the aspect ratio study can suggest that the chiral structure is the majority structure for $\text{Au}_{55}(\text{PPh}_3)_{12}\text{Cl}_6$. Below are some example of structure model and comparison results.

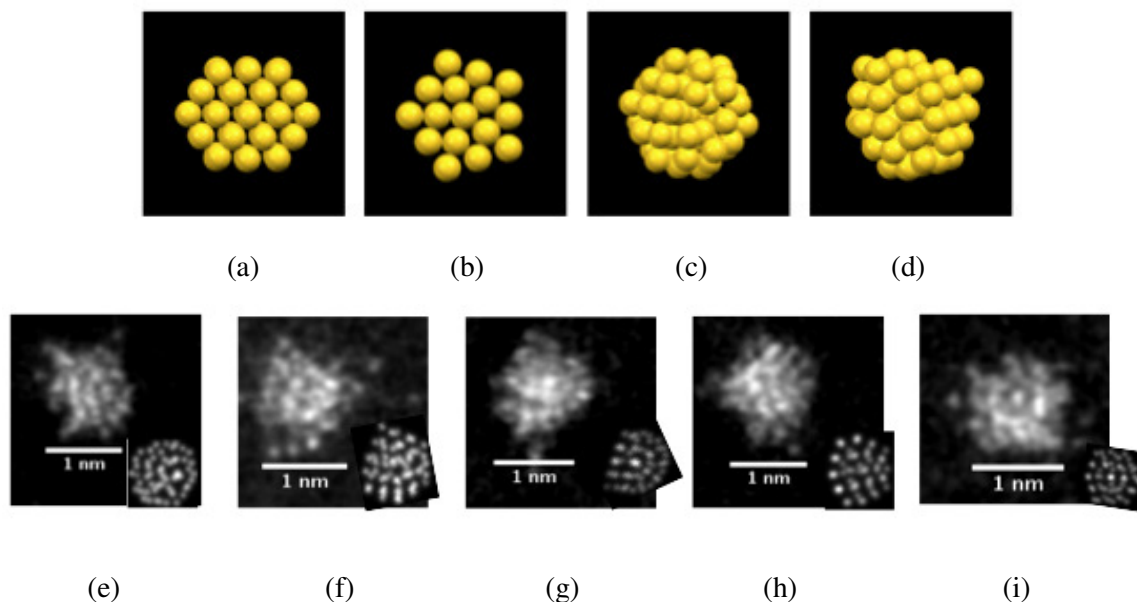


Figure 4 (a)-(d) model of cuboctahedral, decahedral, icosahedral and chiral. (e)-(i) comparison result

References

1. Kolb, D., Ullmann, R. & Will, T. Nanofabrication of Small Copper Clusters on Gold(111) Electrodes by a Scanning Tunneling Microscope. *Science* (New York, N.Y.) 275, 1097–9 (1997).
2. Johnston, R. *Atomic and Molecular Clusters*. (2010).
3. Daniel, M.C. & Astruc, D. Gold nanoparticles: assembly, supramolecular chemistry, quantum-size-related properties, and applications toward biology, catalysis, and nanotechnology. *Chemical reviews* 104, 293–346 (2004).
4. Retnakumari, A. et al. Molecular-receptor-specific, non-toxic, near-infrared-emitting Au cluster-protein nanoconjugates for targeted cancer imaging. *Nanotechnology* 21, 055103 (2010).
5. Schmid, G., Pfeil, R. & Boese, R. $\text{Au}_{55}[\text{P}(\text{C}_6\text{H}_5)_3]_{12}\text{Cl}_6$ —ein Goldcluster ungewöhnlicher Größe. *Chemische ...* 3642, 3634–3642 (1981).
6. Farirbanks, M. C., Benfield, R. E., Newport, R. J. & Schmid, G. An exafs study of the cluster molecule $\text{Au}_{55}(\text{pPh}_3)_{12}\text{Cl}_6$. *solid state communications* 73, 431–436 (1990).
7. Marcus, M. & Andrews, M. Structure and vibrations of chemically produced Au_{55} clusters. *Physical Review B* 42, 3312–3316 (1990).
8. Pennycook, S. Z-contrast stem for materials science. *Ultramicroscopy* 30, 58–69 (1989).
9. Crewe, a. V. A High-Resolution Scanning Transmission Electron Microscope. *Journal of Applied Physics* 39, 5861 (1968).

Development of Simulation Tools for Exploring Plenoptic Camera Applications

CJ Meah^{1,2}, IB Styles²

¹PSIBS DTC, University of Birmingham, UK.

cjm861@bham.ac.uk

²School of Computer Science, University of Birmingham, UK.

Abstract

Plenoptic camera design has many parameters to optimise in order to achieve the best possible 3-D imaging capability. Furthermore construction of the cameras requires specific elements to be placed extremely accurately in the optical train of the system, and optimal parameters differ between applications. An important tool for design and development is simulation, which allows exploration and optimisation without physically committing to a system. Rendering and modelling techniques for plenoptic data are also important in extracting the maximum amount of information, and can be performed on the simulated data. Simulation and rendering software is being developed to allow for *in silico* exploration.

4 Introduction

An ordinary camera consists of a lens and a sensor, and generates an in focus image for the imaging plane of the system, with all other planes out of focus in the final image. In order to change viewpoint, aperture, or focal point, the system must be physically changed and another image acquired. The basis of a plenoptic camera is to preserve the directional information of rays which is lost in a conventional camera; rays which would have met on a sensor pixel are split onto separate pixels by a microlens.

By sacrificing spatial resolution for this angular information image viewpoint, focal plane, and aperture can be changed computationally post-acquisition. In essence, plenoptic cameras provide a 3-D representation of a scene from a single acquisition. This ability has a wealth of applications in a variety of areas.

One issue that a number of free parameters dictate the final performance of the plenoptic system, meaning optimisation of these parameters is needed. Microlens properties also play an important role in determining system performance, and microlens array placement is key to a trade-off in spatio-angular resolution, and often must be accurate on the order of microns. Furthermore, the components of the system must complement each other to attain the maximum efficiency in imaging, for example matching the f-number of both the microlenses and the main lens. These parameters are difficult to explore physically, which is where simulation tools can aid design and exploration.

5 Plenoptic Architectures

There are two well established plenoptic architectures which take different approaches to tackling the spatio-angular trade-off (Georgiev et al. 2006). The original plenoptic camera (often denoted as Plenoptic 1.0) (Ng et al. 2005) consists of a microlens array placed at the principle image plane of the main lens, and the image sensor one focal length behind the microlenses. The microlenses are completely defocused from the scene, and each microlens gathers information for a single conjugate spatial point. In a final rendered image each microlens therefore contributes to a single pixel, meaning

that spatial resolution is determined by the number of microlenses in the array. Computational rendering strategies can improve on this single pixel contribution per microlens (Lumsdaine & Georgiev 2008), but it is a useful baseline. The rays hitting each microlens are split onto the sensor pixels, which can be seen as angular binning. Therefore, the number of pixels covered by a microlens determines the angular resolution.

The emphasis of the original plenoptic camera is on gaining angular resolution, however this is at the expense of spatial resolution which is often the priority in many applications. An alternative plenoptic set-up called the focused plenoptic camera (or Plenoptic 2.0) (Todor Georgiev & Lumsdaine 2010) trades back this gain in angular information for spatial information. It uses the microlenses as a relay system, placing the microlens array a distance a from the image plane and the sensor a distance b from the microlens plane, satisfying

$$1/f = 1/a + 1/b ,$$

where f is the microlens focal length. The angular distribution for a spatial point is now spread over multiple microlenses, and each micro-image represents a spatial image. The raw image produced by the system can be pictured as taken by a multi-view stereo system. When rendering a final image, patches can be taken from micro-images and tiled together, meaning many more pixels per microlens contributing to the image compared with the original plenoptic camera.

Table 1: Outline of different plenoptic architectures.

| Plenoptic Camera Properties | | |
|-------------------------------|---------------------------------------|-------------------------------------|
| Properties | Original Plenoptic Camera | Focused Plenoptic Camera |
| Microlens Plane (mP) | Main Lens Image Plane (MLIP) | MLIP + a |
| Sensor Plane | mP + microlens focal length | mP + b |
| Spatial Resolution | # microlenses | b/a of the sensor resolution |
| Angular Resolution | # pixels under microlens | a/b |

Both plenoptic architectures perform differently due to their approach to the spatio-angular trade-off. It is useful to consider both of these choices; however the physical set-up and component specification will be different for both, which is why plenoptic simulations are useful.

6 Plenoptic Simulation

Optical simulation software is widely accessible, with many commercial packages available. However these are often very expensive and are not specifically designed for plenoptic image exploration. Therefore a software tool was created to enable any architecture of plenoptic camera to be simulated with an input scene.

The majority of the simulation utilises ray tracing methods for propagating geometric rays through the optical system, which consists of an arbitrary set of definable optical components. Ray transfer

matrices were used for this purpose since they are easy to define, extend, and can be calculated very quickly. In a ray transfer matrix system, a ray is defined by a height h and angle θ , which are both relative to the optical axis. By defining a ray in these terms, it can be operated on by a matrix describing an optical path. For instance, the free space and lens matrices are defined as:

$$T = \begin{bmatrix} 1 & d \\ 0 & 1 \end{bmatrix}, \quad L = \begin{bmatrix} 1 & 0 \\ -1/f & 1 \end{bmatrix},$$

where d is the distance travelled in free space, and f is the focal length of the lens. These matrices can be combined so as to produce a system matrix, meaning that a single operation now propagates the ray through the system. In terms of simulating a microlens array, each microlens defines its own optical axis, and it is not known before tracing which lens a ray will hit. Therefore a separate step is involved, where a ray is traced to its intersection with the microlens array and then operated on by the particular microlens it hits. The microlens centre must be treated as the optical axis for the lens refraction operation, but then returned to the system axis.

Instead of considering each ray individually, we can form a vector of rays and operate on this whole vector at once. This is useful in speeding up computation on a CPU. Since plenoptic cameras sacrifice spatial resolution for angular, a higher resolution sensor is normally needed to alleviate these effects. However, a higher resolution sensor means many more rays than are usually needed. This, along with the need to sample angular information adequately, means that a plenoptic simulation needs many more rays than are usually considered in standard ray tracing applications. For a realistic simulation often vectors containing millions of rays are needed.

A key issue in the simulation software is computational speed and efficiency. In backwards ray tracing, a ray is propagated from the sensor through the optical system to the object. This has the advantage of only considering rays which are guaranteed to hit the sensor, which means much higher efficiency for dense scenes and in general. Forwards ray tracing is useful in sparse scenes, and also since it better represents the physical process of image acquisition (rays travel to the sensor in the real world). Backwards ray tracing is favoured for efficiency in this software.

Objects for the simulation can be either matrices of voxels or a polygon based mesh. In both cases, backwards ray tracing requires ray-polygon or ray-voxel intersection methods, which are often the bottleneck in the ray-tracing timeline. A brute-force method requires a ray to be checked with each polygon in the scene. In opaque scenes, surface normals can be used to overlook inaccessible polygons; however scene meshes can have thousands of vertices and faces. An octree implementation allows more efficient checking and indexing of intersections, as opposed to checking for intersections with all polygons for each ray. An octree discretises the scene into blocks, with each block either further discretised or containing mesh vertices. By implementing this discretisation, and using a tree-search algorithm, rays are checked against the octree branches until a node is hit, and the checked against the vertices contained within the node. This is invaluable when simulating large or detailed scenes.

7 Computational Approaches to Plenoptic Data

Rendering methods used on plenoptic data depend on the plenoptic architecture used. Approaches for both the original (Ng 2006) and focused plenoptic camera (Todor Georgiev & Lumsdaine 2010; T. Georgiev & Lumsdaine 2010) have been implemented in real-time to allow easy exploration of image

data. Implementing rendering methods also allows for the development of post-processing algorithms. An example given is the depth map algorithm for the focused plenoptic camera, which exploits the multi-view stereo style set-up by using phase-correlation on neighbourhoods of microlenses to give the relative disparity for regions of space. Both the depth mapping and rendering of images is highly parallelisable, meaning vast increases in computational performance are achievable. The current performance of the MATLAB code to extract a depth map and surface render a 40 megapixel raw plenoptic image is between 20-60 seconds. The performance of the depth map algorithm used is dependent on how detailed a scene (or micro-image) is, with lack of image features leading to unreliable depth estimates.

The 3-D nature of a plenoptic camera allows us to extract the depth information of a scene, and the way in which the 4-D light field is parameterised allows for the use of computed tomography reconstruction techniques, as seen in medical image reconstruction. In terms of surface capture, a system can be simulated which utilises mirrors to provide multi-view analysis from a single acquisition. The reconstruction of this 3-D model is achieved iteratively through a maximum likelihood expectation maximisation (MLEM) reconstruction, which performs better than Radon transforms on multi-view data.

8 Conclusions

A toolbox for plenoptic simulation, rendering and data exploration has been developed which is capable of simulating millions of rays through a complex system of optics. The rendering of plenoptic images has many aspects which have been included in the software, on top of visualisations of surfaces and 3-D models. This toolbox will be useful in plenoptic camera design and, since any scene inputs are supplied by the user, many applications can be explored fully *in silico*. Future work includes incorporating Gaussian beam propagation and wave effects.

References

- Georgiev, T. & Lumsdaine, a., 2010. Reducing Plenoptic Camera Artifacts. *Computer Graphics Forum*, 29(6), pp.1955–1968. Available at: <http://doi.wiley.com/10.1111/j.1467-8659.2010.01662.x> [Accessed June 17, 2013].
- Georgiev, Todor & Lumsdaine, A., 2010. Focused Plenoptic Camera and Rendering. , pp.1–28.
- Georgiev, T., Zheng, K. & Curless, B., 2006. Spatio-Angular Resolution Tradeoffs in Integral Photography. *Rendering* Available at: <http://www.tgeorgiev.net/Spatioangular.pdf> [Accessed October 18, 2013].
- Lumsdaine, A. & Georgiev, T., 2008. Full resolution lightfield rendering. ... *University and Adobe Systems, Tech. Rep.*, (January), pp.1–12. Available at: <http://www.tgeorgiev.net/FullResolution.pdf> [Accessed June 17, 2013].
- Ng, R., 2006. *Digital light field photography*. Available at: http://testcis.cis.rit.edu/~cnspci/references/dip/light_field_photography/ng2006.pdf [Accessed June 21, 2013].
- Ng, R., Levoy, M. & Brédif, M., 2005. Light field photography with a hand-held plenoptic camera. *Computer Science*, pp.1–11. Available at: <http://www.soe.ucsc.edu/classes/cmcs290b/Fall05/readings/lfcamera-150dpi.pdf> [Accessed June 21, 2013].

Comparison of CFD Methods to Wind-tunnel Data for a Class 43 High Speed Train

Justin Morden, Hassan Hemida, Chris Baker

School of Civil Engineering, University of Birmingham, UK., B15 2TT

jam239@bham.ac.uk

Abstract

This paper focuses on the application of computational fluid dynamics (CFD) to external aerodynamic flow around a 1/25th scale class 43 HST model. The CAD model of the train featured a high level of geometric detail within the under-carriage region to improve the accuracy of the simulation and to provide a more accurate simulation of under-body and wake flow structures. Two different CFD methods were used to study the flow around the HST. The obtained surface pressures are compared to wind tunnel data previously collected in order to determine the best practice when simulating external flows.

1 Introduction

Validation of the CFD approach is a critical stage prior to any investigation due to the sensitivity of the setup to a number of factors. With the power of computers following Moore's law the optimum setup used is constantly evolving. With current computational power high detail RANS (Reynolds-averaged Navier-Stokes) based simulations are becoming the normal, therefore a new more accurate approach needs to be investigated to continue pushing research forward. Research published for the LES (Large Eddy Simulation) approach has relied upon the use of highly simplified trains that omit under body detail and even the inter-carriage gap in some circumstances. This research approach provides a high level of insight into the fundamental flow regimes that occur around the body of a train at different yaw angles but fail to accurately study the effect of under body details. This paper looks at the application of a DDES (Delayed Detached Eddy Simulation) approach to a 1/25 scale class 43 HST train with a high level of geometric detail around the under-body. The surface pressure coefficients results of the two CFD approaches will be compared to data collected from a comparable wind-tunnel test to assess their accuracy and allow for a conclusion to be made.

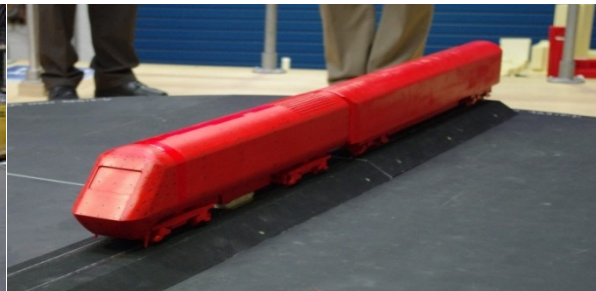
2 Wind-tunnel experiment

Wind tunnel tests were conducted by RWDI on behalf of the research project, The tests were conducted on a 1/25th scale two car model of a class 43 train (Figure 1) on a scale ballast shoulder with rails (Figure 2) The power car, passenger carriage, inter-carriage gap and bogies were all

included in the model. The train and ballast shoulder were mounted upon a raised platform 20cm above ground level to remove any effects created by the boundary layer on the wind tunnel floor. The power car was fitted with 313 pressure taps over its surface that were sampled for a time of 120 seconds for each run to provide time average results. The power car mount was fitted with a load cell to enable the measurement of lift and drag forces and the overturning moment. A total of 11 runs were conducted where the train's yaw angle was varied from 0° to 45° in 5 degree increments at a constant flow velocity of 13.2m/s, the Reynolds number for these simulations was to 1.0×10^5 which is below the recommendations made in British Standards (2009) for the conducting of wind tunnel tests.



Figure 1: full scale HST.

Figure 2: 1/25th scale HST windtunnel model.

3 CFD

The initial step in conducting the CFD simulations was the simplification of the CAD geometry; this involved the removal of the windscreen and roof slats due to their minimal importance and complexities during the meshing process. The sensor umbilical cord was also excluded from the CAD geometry due to its exact dimensions being unknown.

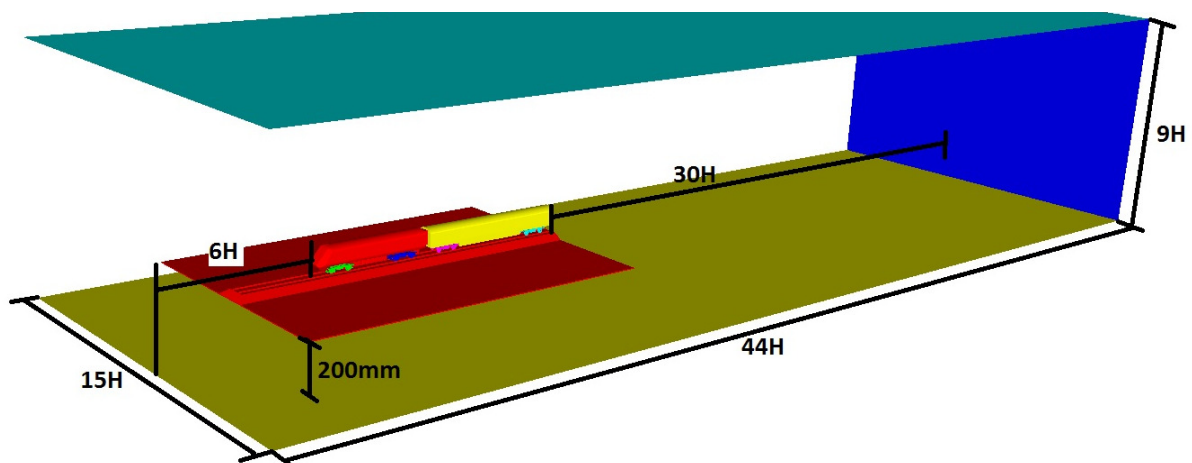


Figure 3: Computational domain sizes (H is height of train)

Figure 3 shows the overall domain size. The blockage ratio calculates to be 6% including the raised platform, this is below the recommendations in section 5.3.4 of the BS EH 14067-4:2005+A1:2009

guidelines which recommends 10%. The blockage ratio of 6% is also lower than the blockage ratios used in Ekeroth (2009) and Hemida (2009).

3.1 CFD setup

Both the RANS and DDES setups were initially run using first order upwind schemes before being switched to 2nd order central differencing schemes, this approach was chosen to improve the initial stability of the simulation and to reduce the time required to achieve convergence. The DDES simulation used a Crank-Nicholson 2nd order scheme for the time integration.

Convergence for the simulation was determined by monitoring the drag and lift forces of the leading carriage until there was no more change against time when plotted using line of best fit using a polynomial of two.

For the RANS simulations the SIMPLE algorithm proposed in Szablewski (1973) was used for the pressure-velocity coupling. The DDES experiments used the PISO algorithm proposed in Issa (1986) for pressure-velocity coupling.

3.2 Computational Mesh

Multiple meshes were produced using the Ansys Tgrid software to conduct a mesh sensitivity study (Figure 4), results of the study showed that a fine mesh of 34 million cells (Figure 5) would provide the highest accuracy whilst still ensuring suitable hardware requirements.

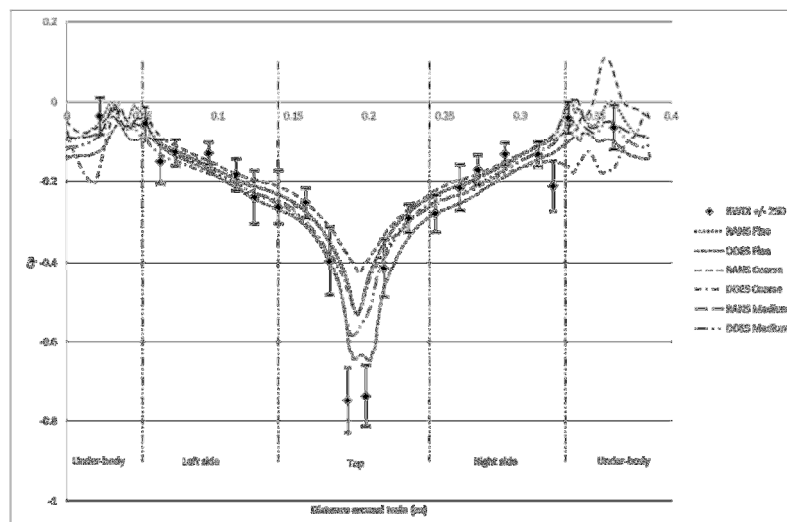


Figure 4: Mesh sensitivity study

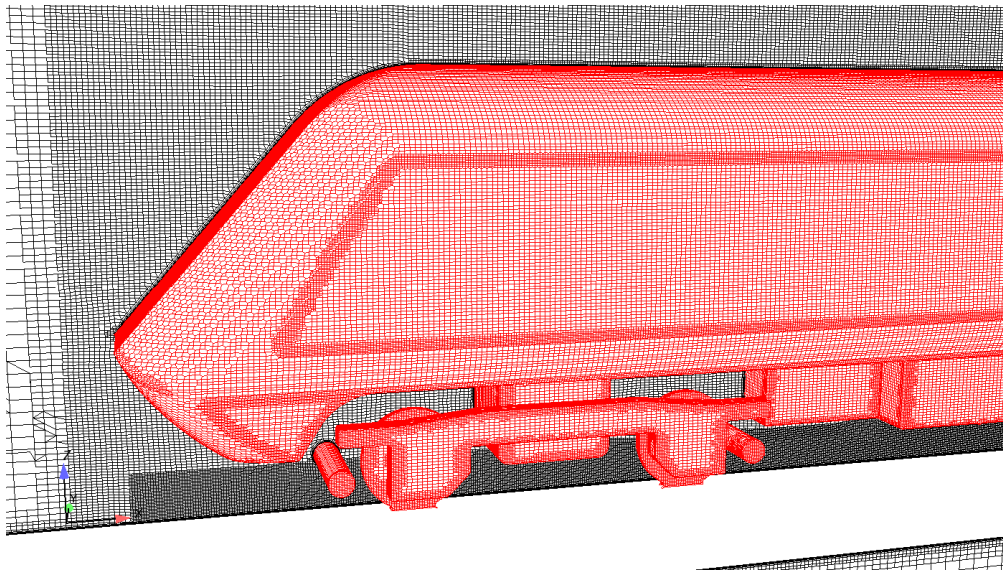


Figure 5: Close up of Fine mesh, showing engine and first bogie (red) and a central slice through the mesh (black)

Figure 5 shows a close up of the fine mesh, along the central slice it can be seen how the mesh density is varied depending upon its location, the mesh near the train is reduced in size in comparison to the larger cells that can be seen on the left side. Due to the importance of underbody detail on the flow field around a train as described in Baker (2010) and Jönsson (2010) the mesh is further refined between to ballast shoulder top and the mid axel height.

4 Results

Pressure taps fitted to the wind tunnel model are grouped in lines (clips) around the train on all three axis, The location of the chossen clip lines for study can be seen in Figure 6.

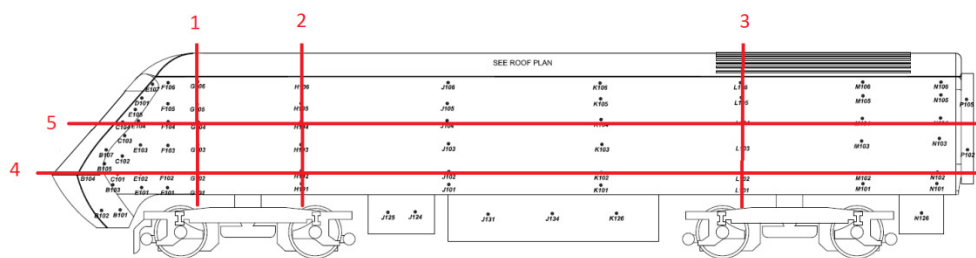


Figure 6: Clip locations on train

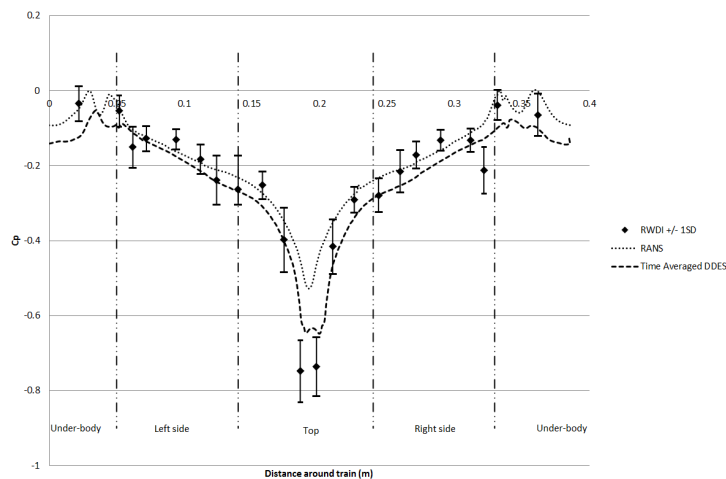


Figure 7: Cp at clip location 1

Figure 7 shows surface pressure coefficient around clip location 1, it can be seen that both the RANS and the DDES approach have similar profiles with the DDES results predicting lower pressure coefficients at all locations. Around the train sides and the undercarriage the two approaches are within or close to the margin of error for the wind tunnel results. Over the roof the RANS method significantly under predicts the pressure coefficient in comparison to the wind tunnel measurements. The DDES method better predicts this, though the calculated value is still below the measured value and its margin of error. It is worth noting that neither the RANS nor DDES approach predicted the pressure drops recorded near the lower sides to the train.

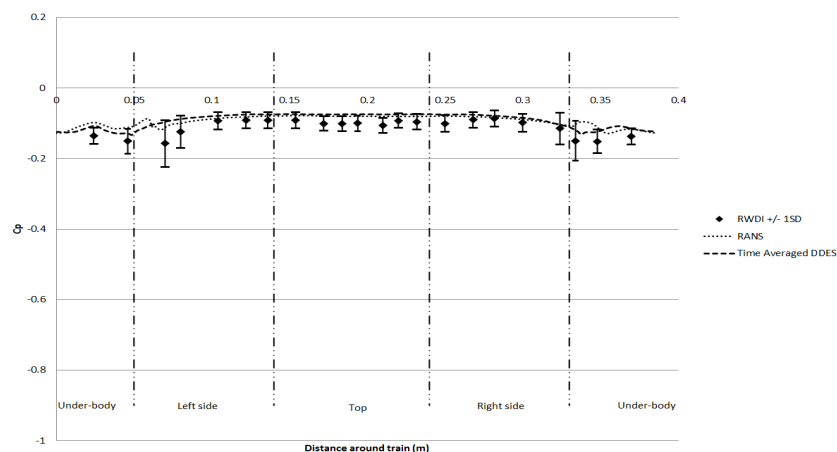


Figure 8: Cp at clip location 2

Figure 8 shows the surface pressure coefficients at clip location 2, at this location both CFD methods predicted similar pressure coefficients to each other over the trains side and roof but differ slightly within the under-body region. Both approaches predict higher pressure coefficients than recorded however both are nearly entirely within the margin of error for the wind tunnel data. Around the lower right side and under carriage the DDES approach proves to be more accurate by correctly

predicting the drop in pressure whereas the RANS approach predicted a rise in the surface pressure coefficient.

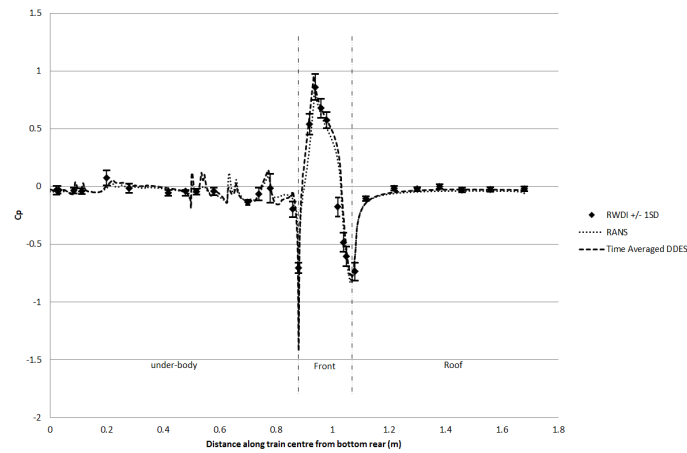


Figure 9: Cp along train centre line

Figure 11 shows a clip along the trains centre line, at this locations the surface pressure coefficients over the trains roof were calculated as an average of pressure taps that are located in close proximity each side of the centre line. Along the centre line of the train both approaches predict the surface pressure coefficients generally stay within the margin of error for the wind tunnel results. The RANS and DDES results also predict similar surface pressure variations within the under-body region, however a lack of pressure tap points within this location in comparison to the geometric complexity adds uncertainty to any conclusions that could be made.

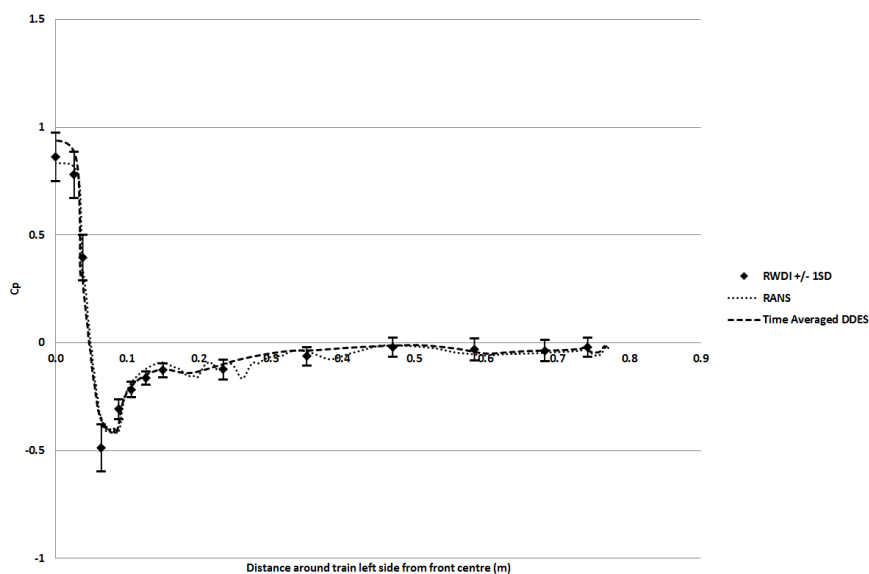


Figure 10: Cp at clip location 4

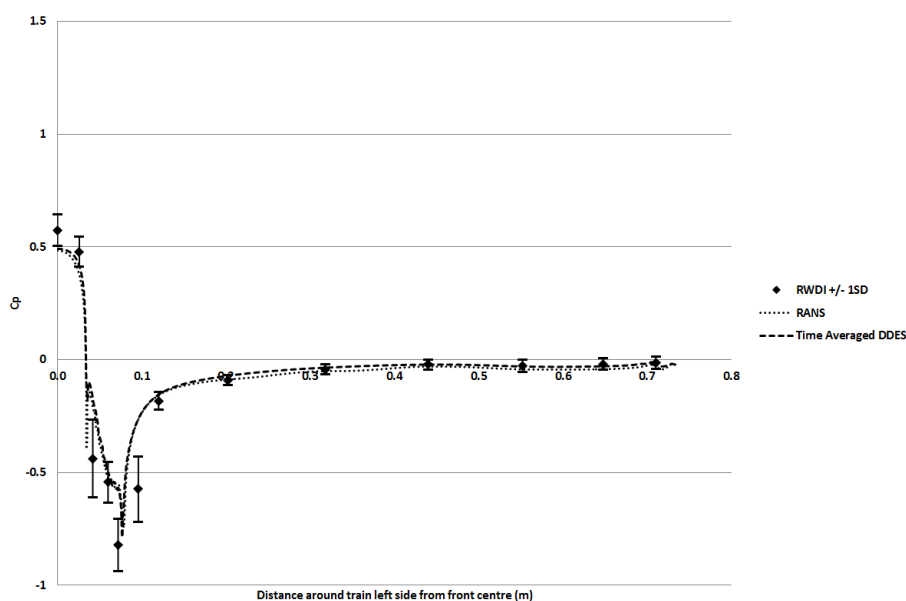


Figure 11: Cp at clip location 5

Figures 10 and 11 shows surface pressure coefficients around the left side of the train starting at the front centre. Both CFD methods show good correlation with results obtained from the wind tunnel tests by remaining within the margins of error for a large majority of the results. In Figure 10 it can be seen that the DDES results over predict the head peak pressure coefficient, the difference between the DDES and RANS results at this point are due to differences in predictions of separation over the ballast shoulders step. In Figure 11 both approaches under predict the head peak pressure and the surface pressures around the corners of the train, this is caused by the removal of the windscreen detail which is normally recessed causing disturbance to the flow around its edges.

5 Conclusion

Both methods accurately replicated the surface pressure coefficients over the train, generally the DDES approach better predicted peak pressures in comparison to the RANS results. The similarity of results was to be expected due to the relative simplicity of calculating surface pressures and due to both approaches relying upon a RANS approach in the near wall regions. A larger difference in the approaches could be seen when the drag coefficients were compared to the wind tunnel data, the wind tunnel model had a drag coefficient of 0.12 whilst the DDES results calculate the drag coefficient to be 0.095, This was considerably more accurate than the RANS results that calculate the drag coefficient to be 0.074. The large difference between the two approaches was due to the difference in wake predictions and the underpredictions of the train head pressure by the RANS approach. The results showed that the overall increase in accuracy and flow information obtainable from the DDES simulation outweighed its increased computational expense when compared to the RANS approach.

6 References

- Baker, C. 2010. The flow around high speed trains. *Journal of Wind Engineering and Industrial Aerodynamics*, 98, 277-298.
- British Standards. 2009. BS EN 14067-4:2005+A1:2009.
- Ekeroth, F., Kalmteq, N., Pilqvist, J. & Runsten, J. 2009. Crosswind flow around a high-speed train on embankment.
- Hemida, H. & Krajnovic, S. 2009. Exploring flow structures around a simplified ICE2 train subjected to a 30 degree side wind using LES. *Journal of Engineering Applications of Computational Fluid Dynamics*.
- Issa, R. I. 1986. Solution of the implicitly discretised fluid flow equations by operator-splitting. *J. Comput. Phys.*, 62, 40-65.
- Jönsson, M. 2010. Numerical investigation of the flow underneath a train and the effect of design changes.
- Menter, F. R. 1994. Two-equation eddy-viscosity turbulence models for engineering applications. *AIAA journal*, 32, 1598-1605.
- Spalart, P. R. 2009. Detached-eddy simulation. *Annual Review of Fluid Mechanics*, 41, 181-202.
- Szablewski, W. 1973. B. E. Launder and D. B. Spalding, *Mathematical Models of Turbulence*. 169 S. m. Abb. London/New York 1972. Academic Press. Preis geb. \$ 7.50. *ZAMM - Journal of Applied Mathematics and Mechanics / Zeitschrift für Angewandte Mathematik und Mechanik*, 53, 424-424.

Methodology Development of Design of a Hybrid Parallel Robot

Hamid Rakhodaei¹, Mozafar Saadat²

¹School of Mechanical Engineering, University of Birmingham, UK

hxr765@bham.ac.uk

²Faculty of Engineering, University of Birmingham, UK.

Abstract

This paper addresses a new method for the design and modeling of a hybrid parallel robot involving two parallel kinematic mechanisms that are serially connected. The design includes a tripod mounted on the moving plate of a hexapod in order to gain a larger overall work volume whilst retaining sufficient overall stiffness for flexible, accurate, and automated gripping and jiggling applications such as the assembly of large aerospace components. Different configurations are analyzed and compared in order to identify the most optimum structural architecture in terms of stiffness and workspace. The theoretical model is supported by the simulation results using SOLIDWORKS, SOLIDSIMULATION and MATLAB software tools. Experimental results were obtained by exerting a known force to the tripod, here acting as the end effector, that causes displacement along the actuator. The actual displacement was then determined by receiving data from a set of strain gauge sensors that are connected to the body of the actuators.

1 Methodology

The 6 UPU-3UPR configuration of hybrid parallel robot is investigated in order to increase the workspace while stiffness of the model remains in suitable level for industry application such as jigs and fixture in aerospace area. The considered characteristics of desired robot lead the investigation about the stiffness and workspace of hybrid parallel robot in comparison with the conventional model of parallel robot such as the tripod and the hexapod. In following study the inverse kinematic of the hybrid model is developed. The developed kinematic model is used to find the actuator size and workspace of robot. In developed model the possible position and orientation of end-effector are searched to check limitation of the system. The stiffness model of hybrid parallel robot is developed by using identified stiffness matrix of the hexapod and the tripod. The finite element analysis of the robots are investigated and compared.

2 Kinematic Mapping

The motions of the end effector for 6 DOF base is calculated by developing the transformation matrix containing all possible rotation and translation motions as given in Equation 1.

$$T = T_r \times (R_\theta \times R_\phi \times R_\varphi) \quad (1)$$

Therefore, the second position of the end effector is obtained by using the transformation matrix. The platforms are considered to be rigid bodies throughout this paper, thus all points on the platforms move along the same path motions.

Firstly, the initial positions of the center point of platform A will need to be identified, together with the linear motions in x, y and z directions, and the desired orientation with reference to the fixed position of the centre point of platform B, as given in

Transformation matrix is used, as shown in Equation 2.1.a .

$$[T] = \begin{bmatrix} c\theta c\psi & -c\theta s\psi & s\theta & 0 \\ c\theta s\psi + c\psi s\theta s\theta & c\theta c\psi - s\theta s\psi & -c\theta s\theta & 0 \\ s\theta s\psi - c\theta c\psi s\theta & c\psi s\theta + c\theta s\theta s\psi & c\theta c\theta & 0 \\ L & M & N & 1 \end{bmatrix} \quad (2.1.a)$$

$$L = s\psi((mc\theta + ns\theta) + c\psi(lc\theta - s\theta(nc\theta - ms\theta))) \quad (2.1.b)$$

$$M = c\psi(mc\theta + ns\theta) - s\psi(lc\theta - s\theta(nc\theta - ms\theta)) \quad (2.1.c)$$

$$N = ls\theta + c\theta(nc\theta - ms\theta) \quad (2.1.d)$$

Where, l, m and n are linear motions along x, y and z respectively.

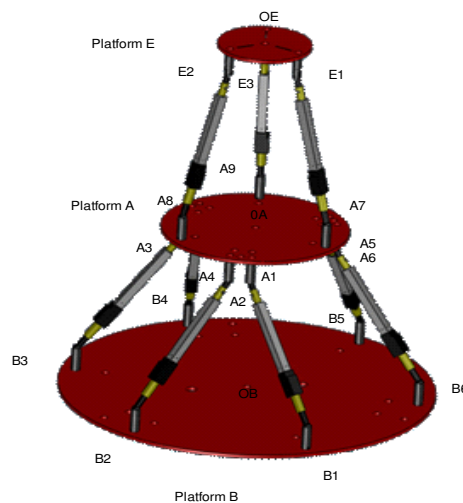


Figure 1: CAD Model for Kinematic

3 Workspace limitation analysis

The developed parametric transformation matrix is capable of illustrating all of the vector motions in space without any limitations due to the actuators and joints, as shown in Figure 1.

Based on the geometrical dimensions and maximum stroke of the actuators, the parameters are obtained as follow:

In order to define the joint limitation, the angles between the actuators and the base platform are obtained and compared with the maximum joints motion range as follows:

$$A_i B_i \cdot U_x = |A_i B_i| \times \cos(\alpha_{B_i}) \quad i \in \{1 \dots 6\} \quad (3.a)$$

$$A_i B_i \cdot U_y = |A_i B_i| \times \cos(\beta_{B_i}) \quad i \in \{1 \dots 6\} \quad (3.b)$$

$$B_i A_i \cdot (U_x \times \frac{A}{B} T) = |B_i A_i| \times \cos(\alpha_{A_i}) \quad i \in \{1 \dots 6\} \quad (3.c)$$

$$B_i A_i \cdot (U_y \times \frac{A}{B} T) = |B_i A_i| \times \cos(\beta_{A_i}) \quad i \in \{1 \dots 6\} \quad (3.d)$$

Where, α_{A_i} and β_{A_i} are the joints' angles with their own X-axis and Y-axis respectively. Moreover, the parameters in equation are defined as: $U_x = (1 \ 0 \ 0 \ 1)$ and $U_y = (0 \ 1 \ 0 \ 1)$.

However, the angles of revolute joints are obtained using equation 4.a,

$$E_j A_i \cdot (U_x \times \frac{A}{B} T) = |A_i B_i| \times \cos(\alpha_{E_i}) \quad i \in \{7 \dots 9\}, j \in \{1 \dots 3\} \quad (4.a)$$

$$E_j A_i \cdot (U_y \times \frac{A}{B} T) = |A_i B_i| \times \cos(\alpha_{E_i}) \quad i \in \{7 \dots 9\}, j \in \{1 \dots 3\} \quad (4.b)$$

Where, α_{E_j} ($j=1, 2, 3$) are the angles of the joints connecting to platform E after a particular motion, and u_{2X} is the axis of the revolute joints in a particular pose and orientation.

Where, B is the positions of joints on lower platform an alpha is angle between actuator and platform.

The maximum translation motion in x and y are assumed the same as that in z axis. The lengths of the actuators and their angles with respect to the base plate are calculated for each motion in order to verify the motion profile.

4 Stiffness of Hybrid Parallel Robot

In this section the stiffness of the hybrid parallel robot is investigated through the comparison of different models. The derived formulation is based on the stiffness matrix of the tripod and the hexapod. Here, all matrices are assumed invariable:

$$F = K \times U \quad (5)$$

Where, the parameters are defined as: $F = [F_x \ F_y \ F_z]^T$, $U = [U_x \ U_y \ U_z]^T$ and K is stiffness matrix.

The Stiffness of the hexapod and the tripod are derived using equations derived by equation 15. The displacement of the hybrid system is equivalent to the sum of the hexapod and the tripod displacements. In order to calculate the equation for the displacement, an inverse matrix of the system stiffness is multiplied and as a result, displacement of system is as follow:

$$U = u_H + u_T \quad (6.a)$$

$$U = K_H^{-1} \times F + K_T^{-1} \times F \quad (6.b)$$

The obtained formulae for the hexapod and the tripod are substituted in the equation 7. Therefore, the stiffness of the system is obtained as follows:

$$K^{-1} = K_H^{-1} + K_T^{-1} \quad (7)$$

4.1 FEA simulation of the models

Finite Element simulations were performed in order to analyze and compare structural stiffness of a number of different configurations of the parallel hybrid robot. Initially, the stiffness of the tripod and the hexapod are obtained separately. The material, mesh size, exerted force, and the pose are identical for all of the models in this simulation in order to compare the effect of size and joint positions in the different configurations as shown in Figures 2 and 3. The material throughout is Aluminum 7075-T6, with a force of 100N exerted to the end-effector. The FE mesh size of 3.048mm was used.

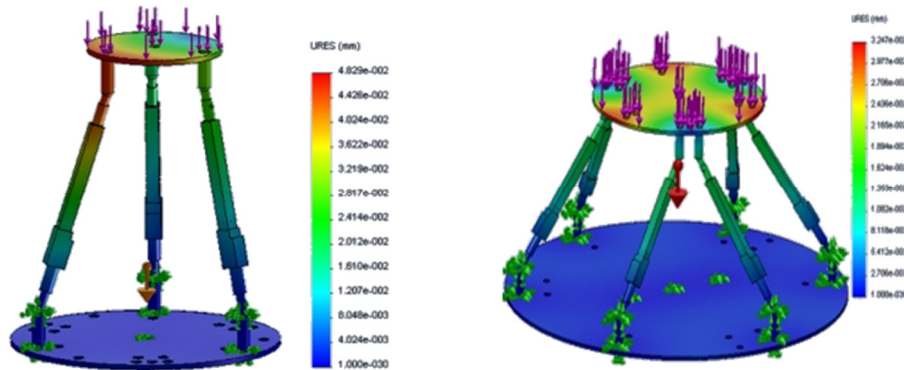


Figure 2: Tripod with D=50, 25 Cm and Tripod With D= 25-12.5cm In Left And Right Hand Side Respectively

The results show that the 3-3 configuration is stiffer than 6-3, while the actuators' displacement is reduced in the 6-3 model.

However four symmetrical configurations based on the lower joints' positions of the tripod are considered and simulated for comparison purposes. These are 6-3-N-3, 6-3-M-3 models as shown in Figures 3.

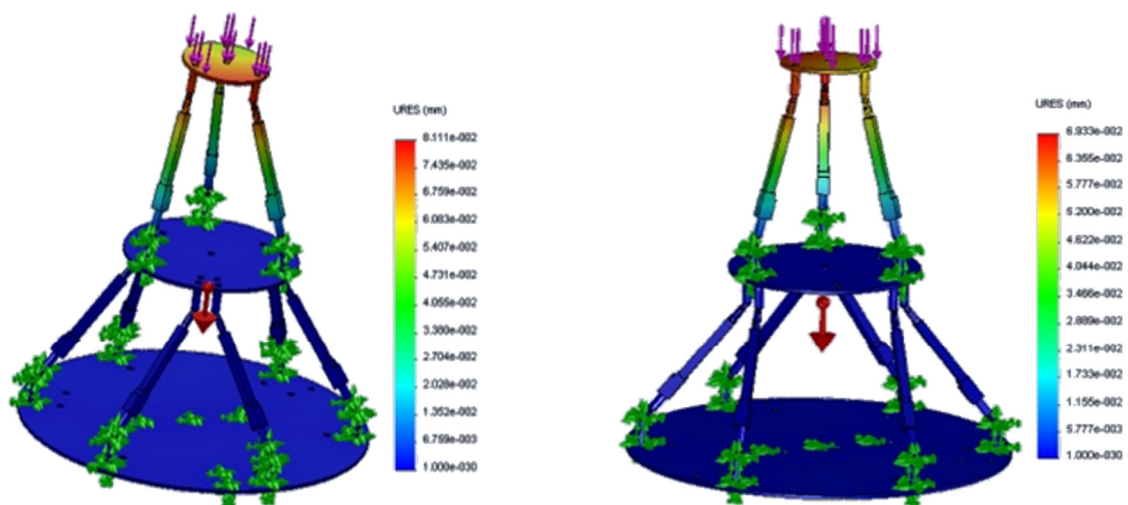


Figure 3: The 6-3-M-3 and the 6-3-N-3 Deformation FEA Analysis

Analysis and simulation of various Stewart Platform configurations for lower limb rehabilitation

Alireza Rastegarpanah, Mozafar Saadat, Hamid Rakhodaei

School of Mechanical Engineering, University of Birmingham, UK.

AXR925@bham.ac.uk

Abstract

In this paper the structure of five different types of Stewart platform were compared to one another with regard to stability under different load conditions. These include a platform with semi-regular hexagons (PSRH), a triangular simplified symmetric manipulator (TSSM), a minimal simplified symmetric manipulator (MSSM), a platform with regular hexagons (PRH) and a platform with similar symmetric hexagons (SSH). Matlab and SolidWorks software were used to determine the exact position of the upper platforms, the length of actuators, and the workspace of the platforms through inverse kinematic analysis following a specific motion profile at a particular time. The desired trajectory according to the workspace of the platforms were also determined. The results show that the platform with semi-regular hexagons has the most stable structure of all. The results are then considered for a robotic lower limb rehabilitation system.

1 Introduction

The aim of physiotherapy by robots is to move paralyzed and disabled organs because of diseases such as cerebral apoplexy (Speich *et al.*, 2004). Using the mobile platform under the patient's foot in order to create movement is a mechanism which is used in the rehabilitation of the ankle. In this mechanism, by programming the movement of the mobile platform, the entire foot or some parts of the foot are impelled to move.

With respect to different arrangements of the joints on platforms and the shape of the platforms, there are different structures with varying levels of stability. In this study five Gough –Stewart platforms of different structures were investigated; one of them is the PSRH structure (a platform with semi-regular hexagons); all of its base joints and all its mobile joints are coplanar and the distance between the actuators is so much greater than in other structures that the probability of contact between the actuators is reduced. Another structure is that of the TSSM (Triangular simplified symmetric manipulator); the mobile platform in this structure is triangular and the joints of the upper platform are close to each other. The third structure is called the SSH (Similar symmetric hexagons); here the shape of the mobile and fixed platforms is symmetric and similar. The structure of similar symmetric hexagons is much like that with semi-regular hexagons, except that with similar symmetric hexagons, the platforms are related to each other in shape ratios of the same size. The fourth structure, called the PRH (Platform with regular hexagons) has regular and similar hexagonal mobile and fixed platforms. The last configuration, called the MSSM (Minimal simplified symmetric manipulator), combines the TSSM with a 3-3 platform, and its mobile and fixed platforms have a similar triangular shape (St-Onge *et al.* 2000 , Ahmadi *et al.* 2013).

It is very complex to identify all the foot motions because these are on three planes and axes. Three kinds of movement are defined for the foot, referred to as plantar\dorsiflexion, eversion\ inversion, and adduction\abduction. According to an analysis of the foot anatomy which was performed in the rehabilitation centre, the desired extent of translation Motions along x, y and z directions is 30 cm, 5-15 cm and 20cm, respectively (Saglia *et al.*,2009).

To choose the most suitably structured Stewart platform for rehabilitation applications, one must consider the anatomy of the ankle and the stability of the five different Stewart platform structures, as analyzed by Solidworks software. Next, the kinematic of the Stewart platform for all configurations was considered and on this basis the maximum workspace of the selected robot was examined.

2 Methodology

2.1 Finite Element Analysis (FEA)

As it can be seen in Figure 1, using Solidworks software, presents the Finite Element analysis (FEA) of the Stewart platform with different structures, in order to find the most stable structure to use for purposes of in rehabilitation. The foot gripper which fixes the foot on top of the platform has been used to perform dorsiflexion and plantarflexion of ankle. In this analysis; assumptions are made about the nature of the problem and the computational limits. All the structures were designed and analyzed statically in the home position, when three different forces – 1500 N, 1300 N and 1100N – were exerted vertically on the gripper. The uniform standard mesh size, small in scale and of high quality, is used for finite element analysis. After finite element analyses had been made of the different structures, it was found that by exerting different forces, the PSRH structure had the lowest stress and displacement, with a higher factor of safety and greater stiffness than the other structures.

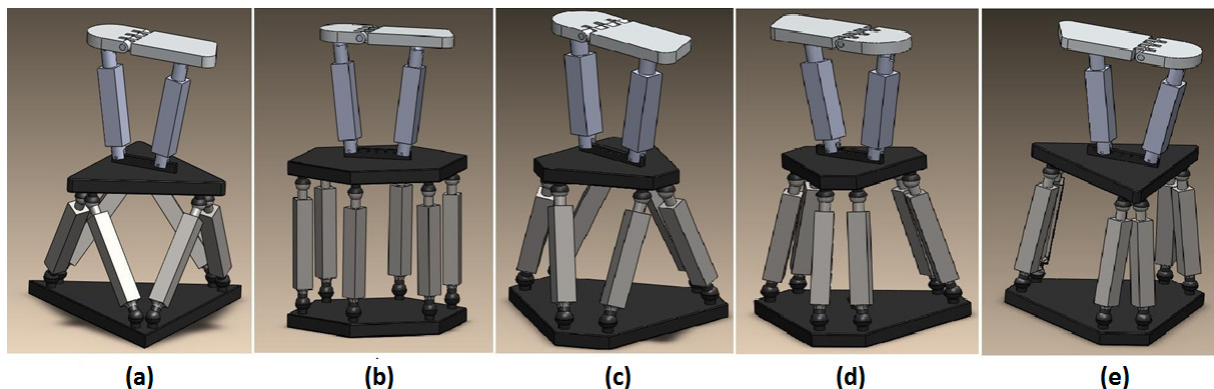


Figure 1-Five different configurations of parallel robot.(a) MSSM ,(b) PRH ,(c) PSRH,(d) SSH,(e) MSSM

2.2 Kinematic

It is worth mentioning that singularity occurs on PRH because of identical geometry of lower platform and upper platform,equal length of actuators and parallel configuration of actuators and PRH can not be considered as a rehabilitation robot. In all the configurations, the lower platform and upper platform are called respectively the “Base” and the “Top”. The linear actuators, which will be called “legs”, are connected to the vertices of the Base and Top with spherical joint (Liu 1993). With respect to **Gruebler's Equation**, this gives the whole system six degrees of freedom (Tsai 1996).The

coordinate system (X, Y, Z) was placed on the centre of the base with the Z axis pointing vertically upwards, called the base frame. The end effector coordinate system (x, y, z) was attached to the centre of the end effector platform with the z axis perpendicular to the end effector, pointing upwards; this coordinate was called the top frame (Gonzalez *et al.*,2011).

L1, L2,..., L6 represent the lengths of the actuators, $[p_x \ p_y \ p_z]^T$ represent the location of the top frame with respect to the base frame and (α, β, γ) represent the rotation angles of the top frame, first around the X axis to α degrees, then around the Y axis to β degrees and at last around the Z axis to γ degrees. Therefore the position and orientation of the upper platform is determined by:

$$Xp = [p_x, p_y, p_z, \alpha, \beta, \gamma]^T \quad (1)$$

The coordinates of these Points with respect to the Base frame are known and fixed, as can be seen in Figure 2. For the five different configurations, the coordinates of vertices of the base and top, with respect to the Base frame, were calculated.

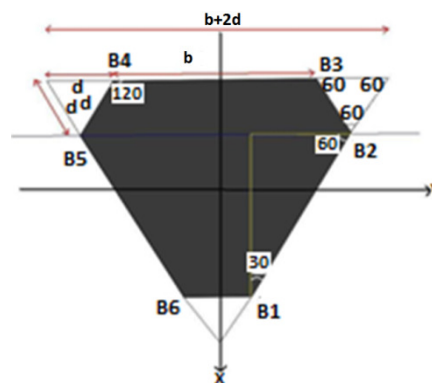


Figure 2 -The hexagonal platform

As Figure 2 shows, in PSRH structure, the hexagon is inscribed by an equilateral triangle whose sides are $(b+2d)$ long. The coordinate system was placed in the centre of equilateral triangle whose x axis divided the side B1B6 into two equal parts (St-Onge 2000). With respect to this coordinate system, the coordinates of the hexagon vertices were calculated. The side of b, d, B and D were respectively 20cm, 66.67cm, 30cm and 10cm respectively. For example the coordinate of 2 vertices in 2 dimension is calculated and other vertices can be calculated with respect to geometry of the Top and Base platforms.

$$\text{Height of the equilateral triangle} = \frac{\sqrt{3}}{2} (B + 2D) \quad (2)$$

$$XB1 = \frac{\sqrt{3}}{6} (2B + D) \quad (3)$$

$$XT2 = \frac{\sqrt{3}}{6} \quad (4)$$

$$YT2 = \frac{(b+d)}{2} \quad (5)$$

In the platform with a structure of regular hexagons, the coordinates of the vertices of the top and base are the same, but the size of the sides of the base differs from the size of the sides of the top. The base side and Top side were 20cm and 30cm, respectively. For example the coordinate of a vertex calculated based on geometry of the platform;

$$XB1 = \frac{\sqrt{3}}{2} a \quad (6)$$

$$YB1 = \frac{a}{2} \quad (7)$$

In the TSSM structure, the coordinates of base vertices are similar to those of the semi regular hexagons. The side of Top (a), bigger side of the Base and smaller side of the Base were 20cm, 30cm and 10cm, respectively. For instance the coordinate of one of the vertices calculated here:

$$XT1 = \frac{\sqrt{3}}{6} a \quad (8)$$

In the MSSM structure, because both platforms are triangular in shape, the coordinate of their vertices are the same as the coordinates of the vertices of the upper platform in the TSSM structure with sides of different sizes. The side of the Top was 20cm and side of the base was 30cm.

In the similar symmetric hexagons configuration, both platforms have a similar shape but the sides are of different sizes. So, the coordinates of the vertices of both platforms, with the different sizes of their sides, would be same as the coordinates of the vertices of the lower platform of the semi-regular hexagons. The side of b,d,B and D were respectively 20cm,66.67cm,30cm and 10cm respectively. After calculating the geometry of each structure, the homogeneous transformation matrix from the TOP (upper platform) to the BASE (lower platform) frames was used for all of the configurations to find the position of the upper platform. It is described by the following transformation matrix:

$$T_{BASE}^{TOP} = \begin{bmatrix} \cos \beta \cos \gamma + \sin \alpha \sin \beta \sin \gamma & -\cos \beta \sin \gamma + \sin \alpha \sin \beta \cos \gamma & \cos \alpha \sin \beta & Px \\ \cos \alpha \sin \gamma & \cos \alpha \cos \gamma & -\sin \alpha & PY \\ \sin \beta \cos \gamma + \sin \alpha \cos \beta \sin \gamma & \sin \beta \sin \gamma + \sin \alpha \cos \beta \cos \gamma & \cos \alpha \cos \beta & PZ \end{bmatrix} \quad (9)$$

Where α, β and γ are rotational motion around X, Y and Z axis, respectively and Px, Py and Pz are translations in X, Y and Z direction. With respect to this homogeneous transformation and the trajectory of Xp , the coordinates of the vertices of the top and base for all of the configurations were calculated by the following equation: (Zhang et al., 2002)

$$\begin{bmatrix} XT_i \\ YT_i \\ ZT_i \\ 1 \end{bmatrix} = T_{BASE}^{TOP}(px, py, pz, \alpha, \beta, \gamma) \begin{bmatrix} XT_i \\ YT_i \\ ZT_i \\ 1 \end{bmatrix} \quad (10)$$

The vertices coordinates of the upper platform and the length of the actuators for all of the configurations were calculated by following equations. But because of the long and bulky equations and repetitive method of calculation, only the equations for calculating the one of the vertices of the top and length of one of the actuators of PSRH structure are given (St-Onge 2000).

$$X_{T1} = -\frac{\sqrt{3}}{6}(2b + d) \times (\cos \beta \cos \gamma + \sin \alpha \sin \beta \sin \gamma) + \frac{d}{2} (-\cos \beta \sin \gamma + \sin \alpha \sin \beta \cos \gamma) + Px \quad (11)$$

$$Y_{T1} = -\frac{\sqrt{3}}{6}(2b + d) \times \cos \alpha \sin \gamma + \frac{d}{2} \cos \alpha \cos \gamma + Py \quad (12)$$

$$Z_{T1} = -\frac{\sqrt{3}}{6}(2b + d) \times \sin \beta \cos \gamma + \sin \alpha \cos \beta \sin \gamma + \frac{d}{2} \sin \beta \sin \gamma + \sin \alpha \cos \beta \cos \gamma + Pz \quad (13)$$

$$L1 = \sqrt{\left(x_{T3} - \frac{d}{2\sqrt{3}} - \frac{b}{\sqrt{3}}\right)^2 + \left(y_{T3} - \frac{d}{2}\right)^2 + z_{T3}^2} \quad (14)$$

$$L1 = T_3 - B_1 \quad (15)$$

Where, X_{T1} , Y_{T1} and Z_{T1} representing the coordinate of the point 1 in Top platform and L1 corresponds to length of actuator number 1 .

2.3 Path motion

To define an accurate path motion for rehabilitation of ankle ,gait analysis have been performed in West Midland Rehabilitation Centre (WMRC), UK. Twenty able-bodied participated in this experiment with age(year) of 24.34 ± 4.83 , weight(kg) of 73.41 ± 5.2 , height(cm) of 172.74 ± 4.2 . As shown in Figure 3, the range of motion and trajectory of movement for lower limb joints have been analysed by Vicon Nexus software.

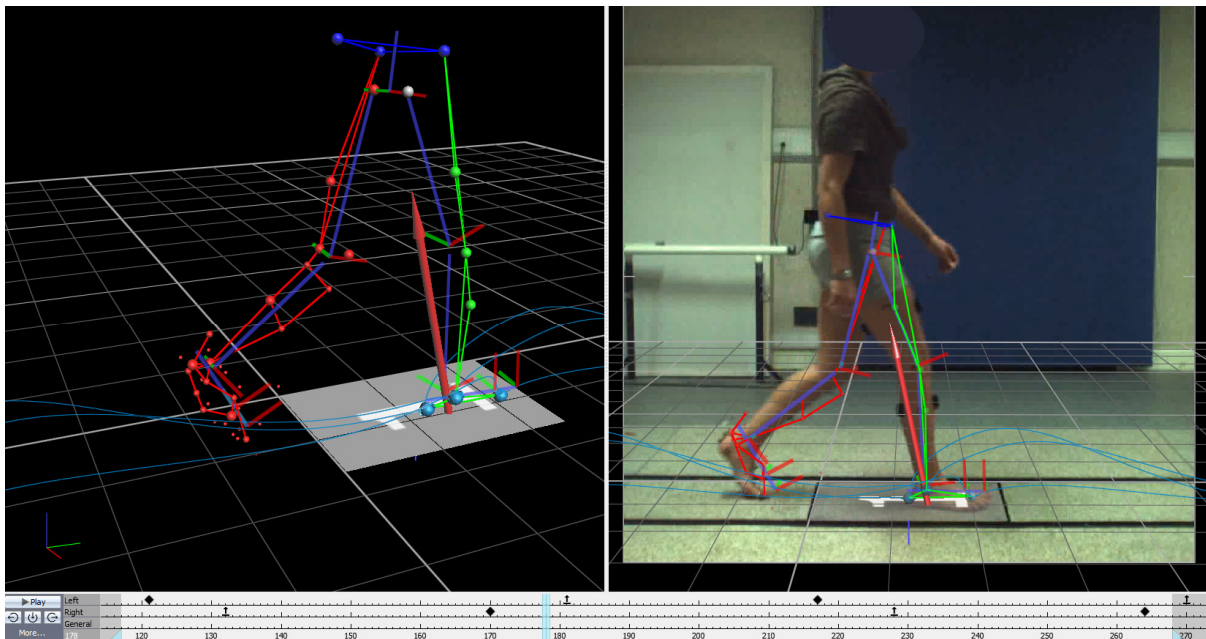


Figure 3 - Gait analysis

Once all the lengths of the coordinates and actuators were calculated, the whole algorithm with some modifications was imported to Matlab software for simulating different motions. In this algorithm, by defining the specific motion profile, orientation and time domain, the exact position of the top (including the coordinates of the centre and vertices of the top) was found at different times. With respect to obtained data from gait analysis, the following trajectory has been defined for the movement of the Top platform, as an rehabilitation exercise:

$$P(i)_{(x,y,z,\alpha,\beta,\gamma)} = \left(\frac{i}{n} \times 68, \frac{i}{n} \times 35, \frac{i}{n} \times 15, 10, -5, -2\right) \quad (16)$$

Where, n referred to the length of time domain, which is [0:25]; parameter (i) is used as a counter, which is in the domain of [2:25].

Workspace of the 6-Dof parallel robot programmed with Matlab software package based on the developed inverse kinematic formulation. The search engine points of workspace is based on Cartesian and polar algorithm. The length of the actuators for each specified position and orientation is calculated in equation 12 in order to identify the stroke size and possibility of each applied motion.

$$L_i = T_{BASE}^{TOP} \times T_i - B_i \quad i \in \{1 \dots 6\} \quad (17)$$

Where, L_i , T_i and B_i are the length of actuators, joint position on moving platform and joint position on base platform respectively.

3 Result

3.1 FEA results

Different forces, 1500 (N), 1300 (N) and 1100 (N), were exerted on the gripper and the maximum displacement and maximum stress for each structure were measured. In FEA analysis, the material which was used for upper platform, lower platforms and gripper was aluminium alloy 1345 and the material of the actuator shafts was carbon steel (Ashby 2005). The thickness of the upper platform and lower platform in all the structures was 3 cm. Moreover, in all the structures, spherical joints of the same size were applied to the upper and lower levels of the Stewart platform. All the structures had the same actuators, the stroke of which was fixed at 2 cm.

The joints play a crucial role in design and in order to achieve the desired DOF, this design used two types of spherical and prismatic joints. Aluminium alloy 1345 was chosen for the upper platform and lower platform (Ashby 2005). By exerting a force of 1500 (N), the PSRHs structure had the maximum displacement of 0.056 mm and maximum stress of 21 (Mpa). The primary stress analysis shows that the maximum stress for PSRH ($2.1e10$). By exerting a load of 1500 (N), the MSSMs structure tolerated the greatest stress of all the structures. PSRH had the highest factor of safety (1.31) and stiffness 26619 (N/mm) of all structures and these results lead to the choice the PSRH structure as the most stable one for manufacturing application.

3.2 Kinematics

The graphs of variation of the length of the actuators with respect to the time, for the five possible structures of the Stewart platform were calculated. With respect to the defined motion profile and initial length of the actuators 36cm and their utmost length 61cm, that the acceptable range of length of the actuators in the PSRH structure would be in the time domain of [19:21] and, in this time domain, the length of the actuators is between 36cm and 61cm. This means that, in other times in the time domain of 0:25, one or more actuators cannot reach the desired length.

With respect to the obtained data from gait analysis, the mean value for ankle's trajectory of 20 participants have been analysed and trajectory of left ankle is shown in Figure 4 :

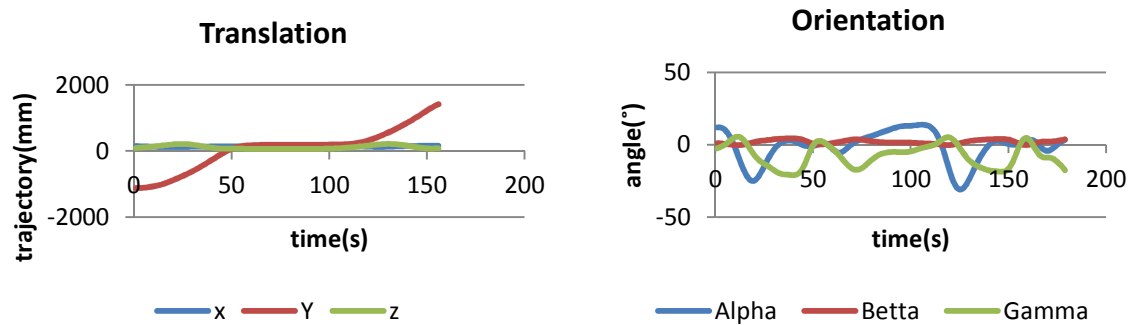


Figure 4 - Trajectory if the ankle joint in a gait cycle

As it can be seen in Figure 5, the path motion for all of the configurations have been simulated using Matlab software .

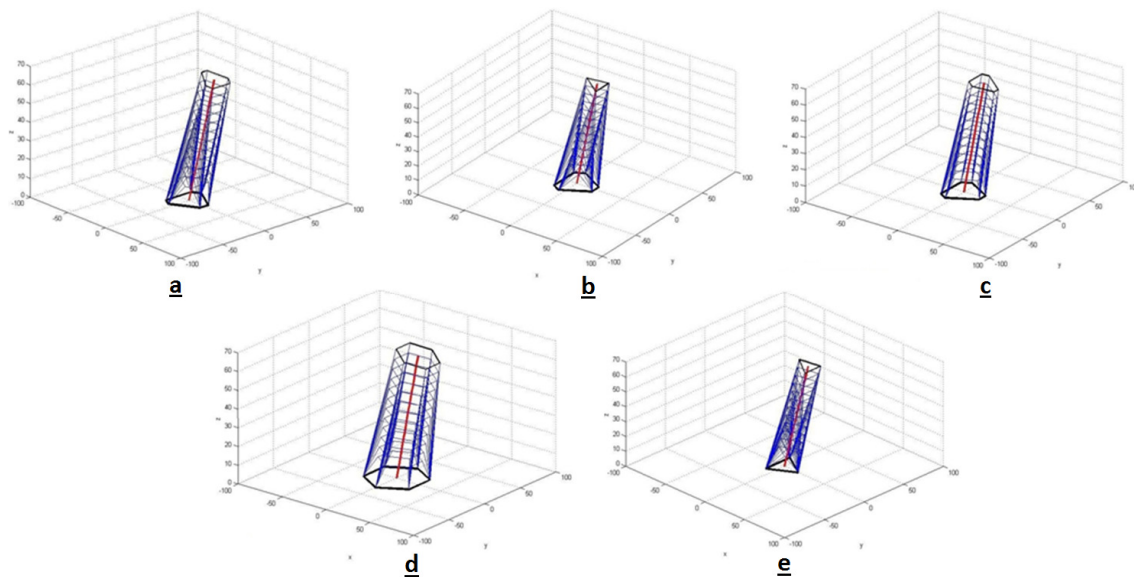


Figure 5 - The position of the Stewart platform with different structures in same motion profile.(a) PSRH; (b) TSSM; (c) SSH; (d) PRH; (e) MSSM

A suitable and simple motion profile with the desired orientation was selected and applied to the algorithm. Figure 6 shows that the workspace of the designed Stewart platform with the PSRH structure was measured and the shape of the derived workspace was similar to what was found by Stoughton (Stoughton *et al.*, 1993). Manipulators which have a short distance between joints such as the TSSM and MSSM have a minor workspace compared with manipulators which have a long distance between joints.

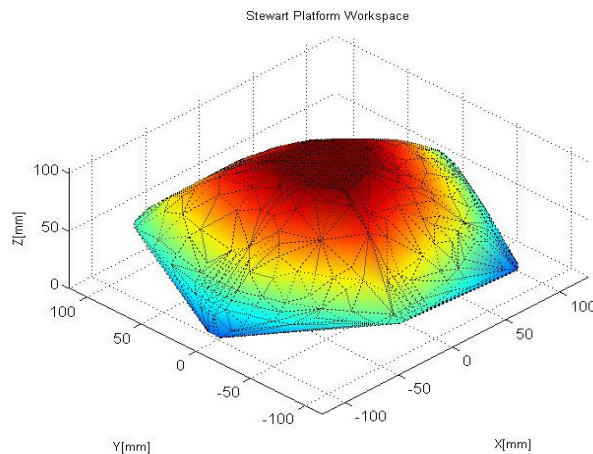


Figure 6 - Workspace Results of Hexapod

4 Conclusion

Different configurations of parallel robot have been modelled and with respect to FEA analysis, their stability compared with each other. Platform of semi regular hexagons showed more stability in compare with other structures and it was found that the stability of different structures completely depends on the position of the joints and actuators and the shape of the platforms. Then, with respect to the gait analysis, the range of movement of lower limb`s joints for 20 able-bodied was obtained. With respect to kinematic analysis and gait analysis, a suitable path motion was defined as a rehabilitation exercise and based on kinematic analysis and defined path motion, the workspace of robot was calculated. With respect to FEA analysis, Kinematic analysis and range of motion of lower limb`s joints, it was found that PSRH structure is a suitable choice for rehabilitation purposes.

5 Acknowledgments:

Authors wish to thank Applied Computing & Engineering (ac&e) Company and West Midland Rehabilitation centre (WMRC) for their supports.

6 References

- Ashby, M. F.2005. Materials selection in mechanical design. MRS BULLETIN, 30, 995.
- Gonzalez, H., and M. S. Dutra.2011, Direct and inverse kinematics of Stewart platform applied to offshore cargo transfer simulation,13th World Congress in Mechanism and Machine Science. Guanajuato, México, 19-25 June
- Kapur, P., R. Ranganath, and B. S. Nataraju.2007. Analysis of Stewart platform with flexural joints at singular configurations. 12th IFToMM World Congress, Besançon,France.
- Liu, K., J. M. Fitzgerald, and F. L. Lewis.1993. "Kinematic analysis of a Stewart platform manipulator", IEEE Transactions on Industrial Electronics, **40**(2): 282-293.

Mousavi, M., Karimi, A., & Tale Masouleh, M. 2013. On the approximated and maximal singularity-free workspace of 6-UPS parallel mechanisms using convex optimization. In *Robotics and Mechatronics (ICRoM)*, 2013 First RSI/ISM International Conference Tehran, Iran , 419-424.

Speich, J. E. and J. Rosen .*Medical robotics*, Marcel Dekker: New York, 2004. 983–993.

St-Onge, B. M. and C. M. Gosselin . 2000 .Singularity analysis and representation of the general Gough-Stewart platform. *The International Journal of Robotics Research*, 19(3): 271.

Saglia, J. A., N. G. Tsagarakis, J. S. Dai, and D. G. Caldwell. 2009 .Inverse-kinematics-based control of a redundantly actuated platform for rehabilitation. *Proceedings of the Institution of Mechanical Engineers, Part I: Journal of Systems and Control Engineering* , **223**(1): 53-70.

Stoughton, Robert S., and Tatsuo Arai.1993.A modified Stewart platform manipulator with improved dexterity, *IEEE Transactions on Robotics and Automation*, 9.2: 166-173.

Tsai, L. W., G. C. Walsh, and R. E. Stamper. 1996. Kinematics of a novel three DOF translational platform, *IEEE*, **4**(4), 3446-3451.

Zhang, D., & Gosselin, C. M. (2002). Kinetostatic analysis and design optimization of the tricept machine tool family. *Journal of manufacturing science and engineering*, 124(3), 725-733.

CFD modelling of lab-scale anaerobic digesters to determine experimental sampling locations

Rebecca Sindall¹, John Bridgeman¹ and Cynthia Carliell-Marquet¹

¹ School of Civil Engineering, University of Birmingham, UK.

rcs587@bham.ac.uk

Abstract

Literature suggests that microbiological communities in anaerobic digesters are damaged at high mixing speeds, reducing biogas production. This paper uses CFD to model a lab-scale mechanically-mixed digester and explore the patterns of turbulent kinetic energy at different mixing speeds. Results using four turbulence models are compared to PIV results and it is found that realisable $k-\epsilon$ is best at predicting digester flow patterns. It is shown that in order to assess the effect of mixing upon the microbiology of the digester, microbial samples should be taken from the impeller region, as well as regions above and below the impeller.

1 Introduction

Each day, the UK water industry collects, treats, and returns to the environment over 10 billion litres of waste water at over 9000 wastewater treatment sites. Sewage sludge is a by-product of this treatment process. Anaerobic digestion (AD) is the most common method of stabilising the sludge before it is disposed of to land. Biogas, the main by-product of AD, can be used as a renewable source of heat and power through the use of combined heat and power units. Thus, increasing the biogas production of an anaerobic digester becomes desirable. Mixing in anaerobic digesters is necessary to bring bacteria in the biomass and food sources in the sludge together so that sludge stabilisation can occur (USEPA, 1976). However, the effects of mixing on biogas production are not clear, though there is a growing body of literature that suggests that a low level of mixing is beneficial (Kaparaju et al., 2008, Stroot et al., 2001). It is hypothesised that this is because high levels of turbulence at high mixing speeds are detrimental to methane-producing bacteria (Hoffman et al., 2008). In this work, CFD simulations of a lab-scale mechanically-mixed digester are used to identify areas of high and low turbulence within digesters mixed at different speeds. This allows future experimental work to identify appropriate sampling locations for the study of microbiological communities present in areas of high and low turbulence. This will allow a better understanding of the link between mixing and biogas production.

2 Methodology

2.1 Model geometry

The CFD model is of a cylindrical vessel with a four-bladed flat impeller and four baffles spaced equally around the vessel wall. The geometry of the vessel and the detail of the impeller are shown in Figure 1. The digester has a diameter of 200 mm and a height of 200mm. The impeller has a diameter of 90 mm, height of 20 mm, and blade thickness of 8 mm. It is located so that the impeller

centreline is 60 mm above the base of the digester. The baffles are 10 mm thick and extend 10 mm from the vessel side.

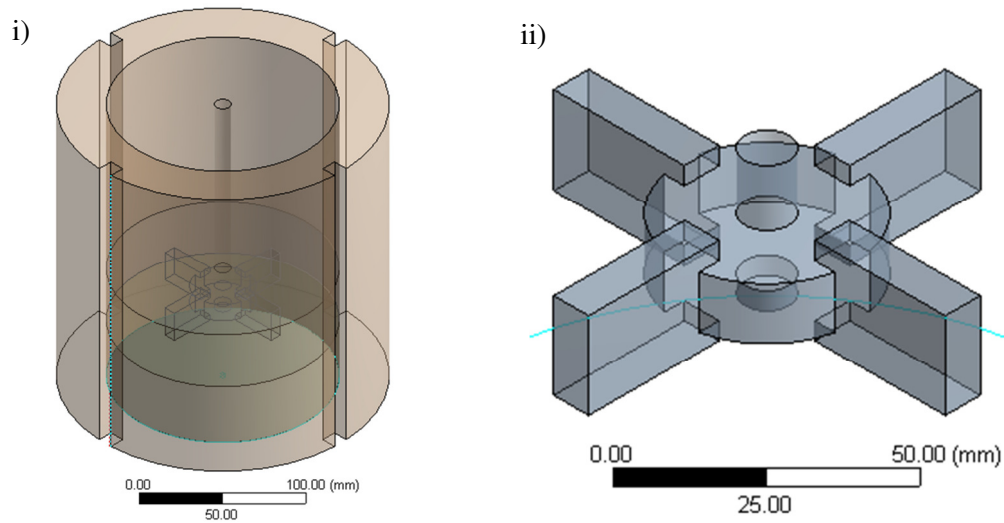


Figure 1– Geometry of i). the digester vessel and ii). the impeller

2.2 Numerical method and boundary conditions

Commercial CFD software, ANSYS Fluent 13.0 (ANSYS-Fluent, 2010a) was used to create the digester model. The geometry and mesh were created using ANSYS DesignModeler and ANSYS Meshing in ANSYS Workbench 13.0 (ANSYS-Fluent, 2010b).

The simulations were run using a second-order upwind discretisation scheme for the convection terms whilst the pressure terms were discretised using a central differencing scheme. The use of a second order convection scheme allows for better resolution of the gradients which in turn gives more accurate solutions than a first-order scheme. However, second-order schemes can take significantly longer to run. Following current best practice, simulations were run using a first-order convection scheme until they were partially-converged and then a second-order convection scheme was applied to reach a fully-converged solution. The semi-implicit method for pressure-linked equations (SIMPLE) (Patanker and Spalding, 1972) is used for de-coupling pressure and velocity.

A sliding mesh (SM) is used in order to capture any unstable flows as the level of rotor-stator interaction is unknown. With the SM method, the vessel is split into two regions, the impeller region and the bulk region. The mesh within the impeller region rotates at a rotational velocity equal to that of the impeller, whilst the mesh within the bulk region remains stationary. The momentum equations are solved across the mesh for each time step, and at the end of the time step, the impeller region slides past that of the bulk region. For this to be possible, the interface between the two regions must be rotationally symmetrical and non-conformal. At the end of each time step, the non-conformal interfaces are updated to reflect the new positions of the two zones relative to one another. This method allows the model to predict unsteady flows as they occur.

All of the walls of the digester, including the base and the impeller blades were specified using a no slip condition. In order to accurately capture the boundary layer, 5 prism layer cells are used on all surfaces that are considered as walls, with a growth rate of 1.2 and the thickness of the first cell being 0.1 mm. As the maximum y^+ in the digester is 1.46, a wall function is not necessary. The liquid free surface was modelled as a symmetry plane.

The non-Newtonian fluid model used was calculated from viscosity measurements of the sludge used in the experimental work, carried out using a Couette viscometer (Fann Model 35). The model uses a density of 965 kg/m³ and follows a non-Newtonian power law model, $\eta = k\dot{\gamma}^n$, with consistency index, $k = 0.0788 \text{ Pa}\cdot\text{s}^{0.8088}$, power law index, $n = 0.8088$ and allowable viscosity range of 0.02–0.035 kg/m-s. A non-Newtonian power law viscosity model was chosen as it has been successfully employed to describe the rheological properties of sewage sludge previously (Seyssiecq et al., 2003) and is considered to be a robust but straightforward model.

2.3 Computational mesh

The unstructured hexahedral mesh was generated using ANSYS Meshing in Workbench 13.0 (ANSYS-Fluent, 2010b). The Grid Convergence Index (GCI) (Roache, 1998) is a simple method to report grid convergence without being limited to doubling the number of cells in each consecutive grid. This allows the grid density to be analysed to provide an indication of error bands. Velocity magnitude values were extracted for 500 individual points in the flow field, and the GCI was calculated as:

$$GCI = F_s \frac{e_{rms}}{r^2 - 1}$$

$$e_{rms} = \sqrt{\frac{\sum_{m=1}^{750} |(u_{m,1} - u_{m,2})/u_{m,2}|^2}{500}}$$

$$r = \left(\frac{h_2}{h_1}\right)^{1/3}$$

where u_m is velocity magnitude at point m , h is the number of cells in the mesh and subscripts 1 and 2 refer to coarse and fine mesh respectively. A factor of safety of $F_s = 1.25$ was applied in accordance with published recommendations for the comparison of multiple grids (Roache, 1998).

Five grid densities were tested: 402,000, 603,000, 966,000, 1,409,000 and 2,347,000. Taking the coarsest mesh as a baseline, GCIs were calculated for the finer grids as 9.6 % (603,000), 7.5 % (966,000), 5.9 % (1,409,000) and 5.7 % (2,347,000). From this, it can be seen that the solutions from the two finest grids approach solution convergence. Whilst the two grids fall slightly outside the 95 % confidence interval, the increase in computing time when increasing the mesh density from 1,409,000 to 2,347,000 was not considered to reflect a corresponding increase in the accuracy of the results and as such the 1,409,000 cell grid will be used to calculate flow patterns in the digester. As such, error bars of 6 % can be attached to the results of the simulations undertaken.

3 Results

3.1 Model validation and turbulence model selection

The results from a number of simulations which made use of various turbulence models were compared to the results of particle image velocimetry (PIV) experiments carried out in a clear plastic replica digester mixing 0.5 g/l carboxymethyl cellulose (CMC) solution at 100 rpm. The turbulence models tested were the realisable k - ϵ , standard k - ω , SST k - ω and Reynolds Stress Model.

Figures 2 and 3 show the u and v velocities along a line at $r/R = 0.6$ with results taken from PIV and CFD simulations. It can be seen that all four turbulence models are able to recreate the general shape of the u and v velocity plots for the PIV data. For all of the turbulence models the peak u velocities in the impeller region are predicted to be slightly higher than the peak demonstrated by the PIV data. The magnitude of the peak u velocity is best predicted by the SST $k-\omega$ model and the Reynolds Stress Model. Both the standard $k-\omega$ and the realisable $k-\epsilon$ models underestimate the magnitude of the peak. Below the impeller, all four of the turbulence models follow the same curve and all four underestimate the magnitude of the u velocity. There are significant differences between the four turbulence models considered above the impeller. Unfortunately, due to the limited frame used in the PIV data, the behaviour of the sludge in the top third of the digester was not monitored and no comparison between the CFD and PIV data can be made. In the area directly above the impeller the u velocities predicted by the realisable $k-\epsilon$ model are closest to the shape and magnitude of the PIV data. Whilst parts of this curve are well followed by the standard $k-\omega$ and the SST $k-\omega$ models, the Reynolds Stress Model does not predict the u velocities well in this area.

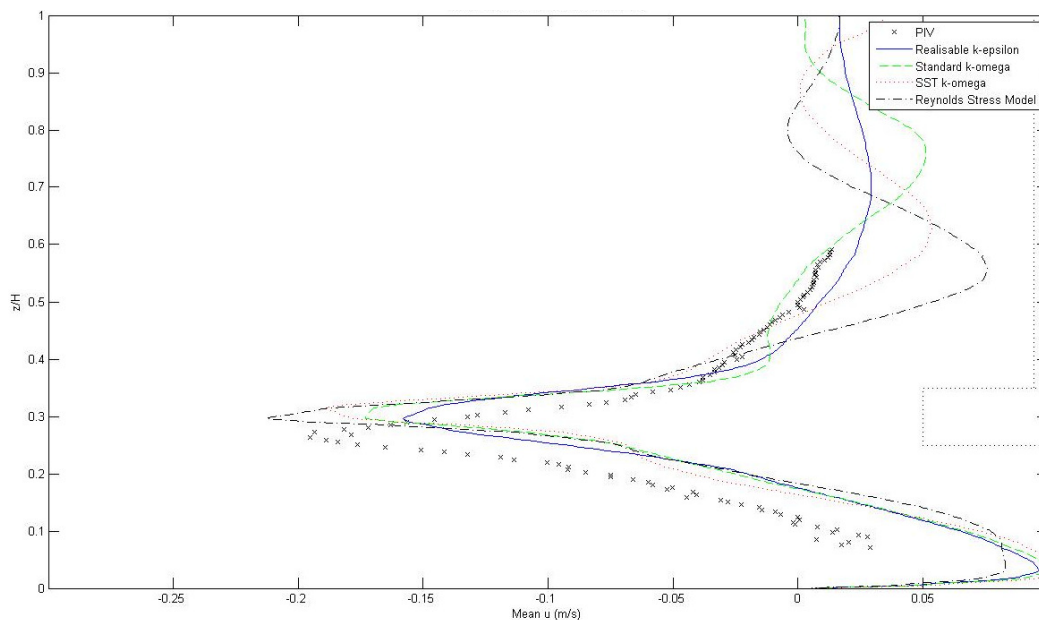


Figure 2 – u velocities along a line at $r/R = 0.6$ modelled using four different turbulence models, as compared to results from PIV

As for the u velocities, the location and magnitude of peak v velocities are well predicted by the CFD simulations with the standard $k-\omega$, SST $k-\omega$ and Reynolds Stress Models all predicting the magnitude of the peak below the impeller very well despite placing it slightly higher in the digester than it is seen to occur from the PIV data. The realisable $k-\epsilon$ model is better at locating the peak, though it underestimates the magnitude. This is also true when considering the peak above the impeller. This is well-located by the SST $k-\omega$ and Reynolds Stress Models as well, though these models overestimate the magnitude of the peak. The standard $k-\omega$ model underestimates the magnitude of this peak but predicts a wider peak than is identified by the PIV data. The realisable $k-\epsilon$ model predicts the uppermost PIV data points with remarkable accuracy.

From the u and v velocity PIV data, the turbulent kinetic energy was calculated and compared to the turbulent kinetic energy predicted by the CFD simulations as shown in Figure 4. Whilst all four of the turbulence models are able to predict the location of the peak turbulent kinetic energy, none of the

models predict the magnitude of the peak well. The best of the models is the realisable $k-\epsilon$ model which predicts approximately 65 % of the peak magnitude. The other three models predict less than 15 % of the peak magnitude.

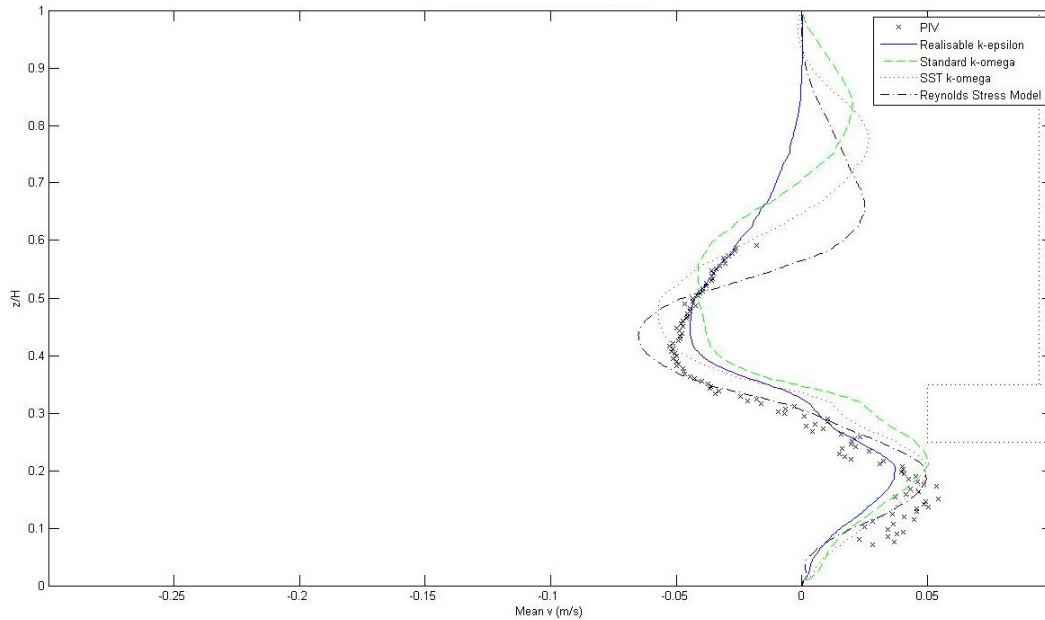


Figure 3 – v velocities along a line at $r/R = 0.6$ modelled using four different turbulence models, as compared to results from PIV

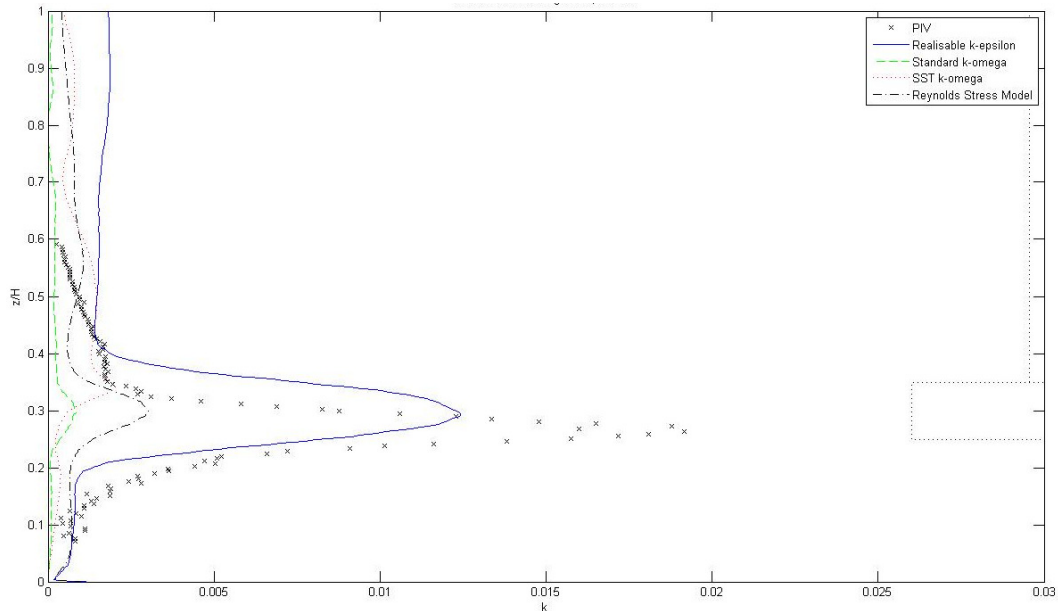


Figure 4 – Turbulent kinetic energy, k , along a line at $r/R = 0.6$ modelled using four different turbulence models, as compared to results from PIV

Whilst the realisable $k-\epsilon$ model underestimates the peak magnitudes of both velocity and turbulent kinetic energy, it appears to be the best fit to the PIV data. It is also the best at predicting the turbulent kinetic energy. As such, all further results are based on simulations which make use of the realisable $k-\epsilon$ model.

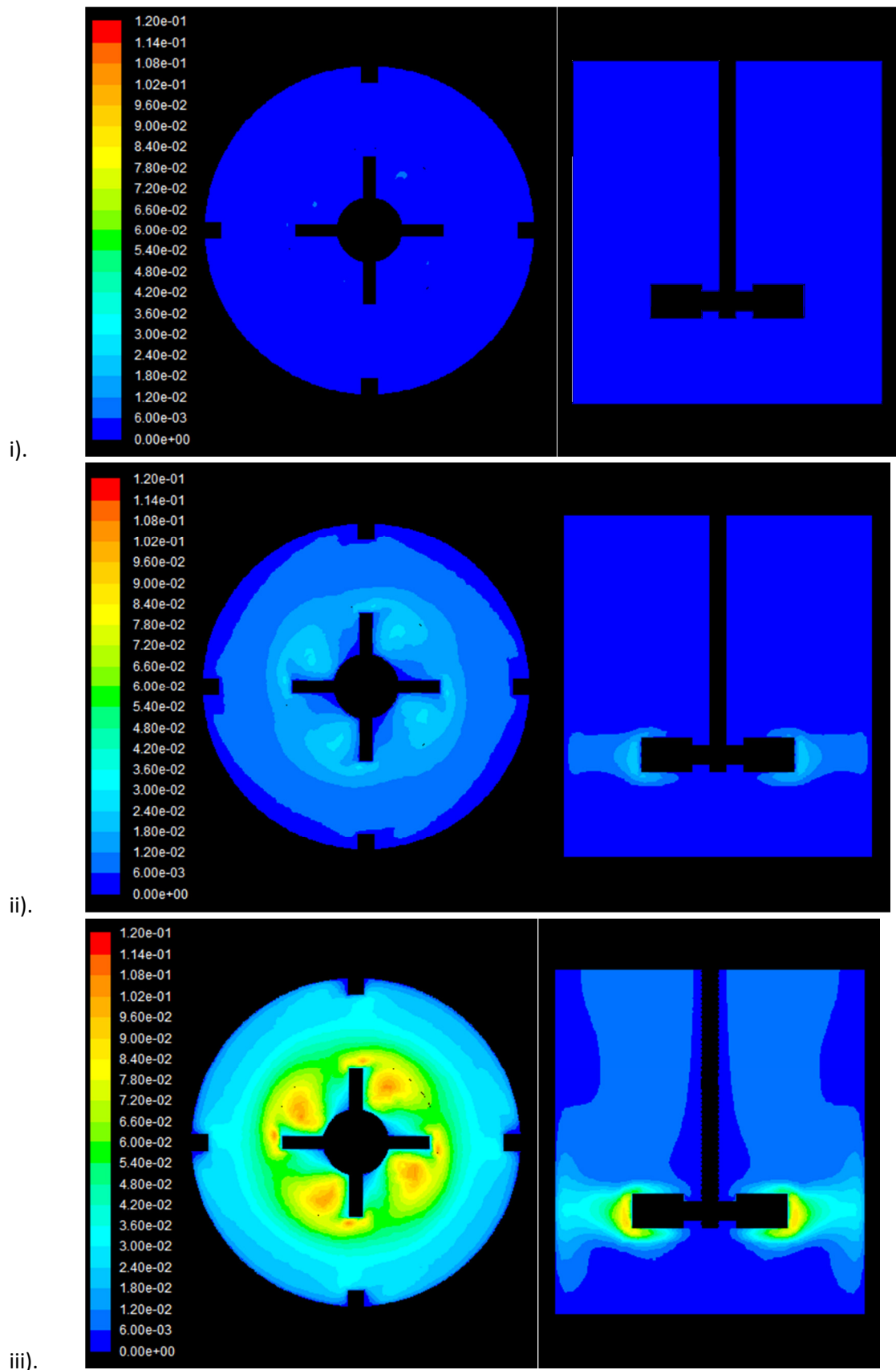


Figure 5 – Contour plots of turbulent kinetic energy for digesters mixed at i). 50 rpm, ii). 100 rpm and iii). 200 rpm

3.2 Turbulent kinetic energy

Turbulent kinetic energy (TKE) is the mean kinetic energy per unit mass. It is the result of fluid shear, friction or buoyancy and therefore may be considered as an indication of the impact of turbulence on flocs and microbial communities in the digester. As TKE is calculated from a scalar transport equation, it is likely that the exact values predicted by Reynolds-averaged Navier-Stokes (RANS) CFD models as used here will be inaccurate. The accuracy of these results could be improved by using a large eddy simulation (LES) model. However, the contours and relative magnitudes across the vessel predicted by RANS simulations in this work are still of interest. The k - ϵ model used in these simulations models the TKE based on the assumption that turbulence is isotropic. In scenarios where anisotropic turbulence dominates, it is expected that this will lead to the over-prediction of TKE, although this is not the case when comparing the model to the PIV experiments discussed above.

Figure 6 shows the TKE contours in the digester at mixing speeds of 50, 100 and 200 rpm respectively. At a mixing speed of 50 rpm, there is virtually no predicted TKE. At 100 rpm and 200 rpm, there are differences in the magnitude of the TKE but the contour patterns are similar. Notably, and unsurprisingly, the highest levels of TKE appear in the impeller region, with virtually no TKE predicted above and below the impeller. The magnitude of TKE at the tips of the impeller blades and in the recirculation regions in the wake of the blades is a magnitude higher than in the bulk of the digester. This clearly demonstrating that it is in the impeller region that the turbulence experienced is at its highest.

3.3 Turbulent intensity

The turbulence intensity, I , is often used as a non-dimensional measure of the level of turbulence. It is defined mathematically as:

$$I = \frac{\sqrt{\frac{2}{3}k}}{u}$$

where k is turbulent kinetic energy and u is the mean velocity.

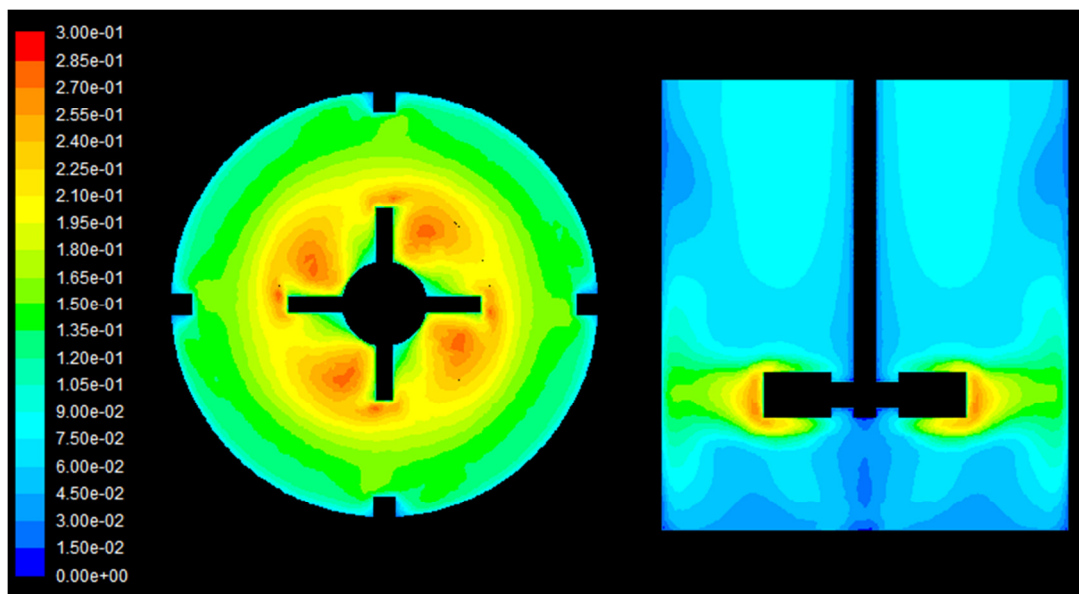


Figure 6 – Contour plots of turbulence intensity for a digester mixed at 200 rpm

The mean velocity was selected as the tip speed of the impeller in order to give a global turbulence intensity. Figure 6 shows an example of the turbulence intensity contours in the digester. By normalising the turbulence intensity by dividing by the tip speed, all of the digesters experience similar contours and turbulence intensity magnitudes. The bulk of the digester experiences very little turbulence, with turbulence intensities of 10 % or lower. However, in the plane of the impeller, the turbulence intensity is significantly higher, with intensities of 10-20 % close to the walls and of 20-30 % in the impeller region. Once again, the highest turbulence intensities are found at the tip of the impeller blades and in the recirculation regions in the wake of the blades.

From this, it can be seen that turbulence intensity varies dramatically across the digester. As such, in order to judge the effects of mixing on microbiological communities, samples would need to be taken from the impeller region as well as from the regions above and below the digester.

4 Conclusions

In this work, a lab-scale anaerobic digester was modelled using a range of turbulence models and compared to PIV experiments. The realisable $k-\varepsilon$ model was found to be most capable of accurately predicting the flow patterns brought about by mixing. Using this model, it was found that the highest levels of TKE are found in the impeller region. The magnitude of TKE at the tips of the impeller blades and in the recirculation regions in the wake of the blades was an order of magnitude higher than in the bulk of the digester. As mixing speeds increase, the magnitude of TKE was found to increase correspondingly, giving similar contours of turbulence intensity at all mixing speeds. A more complex model, such as LES, would be required to accurately assess the value of TKE, but this work does demonstrate the relative magnitude of TKE in a digester. This is sufficient to recommend that in order to assess the effects of mixing on microbiological communities, samples should be taken from the impeller region, above the impeller region and below the impeller region.

References

- ANSYS-FLUENT 2010a. Fluent 13.0. Lebanon, NH.
- ANSYS-FLUENT 2010b. Workbench 13.0. Lebanon, NH.
- HOFFMAN, R., GARCIA, M. L., VESVIKAR, M., KARIM, K., AL-DAHMAN, M. H. & ANGENENT, L. T. 2008. Effect of shear on performance and microbial ecology of continuously stirred anaerobic digesters treating animal manure. *Biotechnology and Bioengineering*, 100, 38-48.
- KAPARAJU, P., BUENDIA, I., ELLEGAARD, L. & ANGELIDAKI, I. 2008. Effects of mixing on methane production during thermophilic anaerobic digestion of manure: Lab-scale and pilot-scale studies. *Bioresource Technology*, 99, 4919-4928.
- PATANKER, S. V. & SPALDING, D. B. 1972. A calculation procedure for heat, mass and momentum transfer in three-dimensional parabolic flows. *International Journal of Heat and Mass Transfer*, 15, 1787-1806.
- ROACHE, P. J. 1998. Verification of Codes and Calculations. *American Institute of Aeronautics and Astronautics Journal*, 36, 696-702.
- SEYSSIECQ, I., FERRASSE, J.-H. & ROCHE, N. 2003. State-of-the-art: rheological characterisation of wastewater treatment sludge. *Biochemical Engineering Journal*, 16, 14-56.
- STROOT, P. G., MCMAHON, K. D., MACKIE, R. I. & RASKIN, L. 2001. Anaerobic codigestion of municipal solid waste and biosolids under various mixing conditions - I. digester performance. *Water Research*, 35, 1804-1816.
- USEPA 1976. Anaerobic Sludge Digestion Operations Manual.

Parallel Solution of the Linear Elasticity problem with applications in Topology Optimization

James Turner¹, Michal Kocvara¹ and Daniel Loghin¹

¹School of Mathematics, University of Birmingham, UK.

turnerj@maths.bham.ac.uk

Abstract

In this paper, we aim to solve the system of equations governing linear elasticity in parallel using domain decomposition. Through a non-overlapping decomposition of the domain, our approach aims to target the resulting interface problem, allowing for the parallel computation of solutions in an efficient manner. As a major application of our work, we apply our results to the field of topology optimization, where typical solvers require repeated solutions of linear elasticity problems resulting from the use of a Picard approach.

1 Introduction

Consider a solid elastic body occupying an open and connected domain $\Omega \subset \mathbb{R}^d$ with Lipschitz boundary $\partial\Omega = \partial\Omega_D \cup \partial\Omega_N$, where clamping and traction are imposed on $\partial\Omega_D$ and $\partial\Omega_N$ respectively. Under the application of both body forces $f: \Omega \rightarrow \mathbb{R}^d$ and boundary tractions $g: \partial\Omega_N \rightarrow \mathbb{R}^d$, the material is subject to deformation so that a given reference point \mathbf{x} of the initial undeformed material is translated to the vector $\mathbf{x}' = \mathbf{x} + u(\mathbf{x})$ of the deformed material, with u denoting the displacement. Through the assumption of linearly elastic material behaviour, the governing equations for u correspond to the following mixed boundary value problem

$$\mathcal{L}u := -\nabla \cdot \sigma(u) = f \quad \text{in } \Omega, \quad (1a)$$

$$\sigma(u) = E: \varepsilon(u) \quad \text{in } \Omega, \quad (1b)$$

$$u = 0 \quad \text{on } \partial\Omega_D, \quad (1c)$$

$$\sigma(u) \cdot \hat{n} = g \quad \text{on } \partial\Omega_N. \quad (1d)$$

In the above, the strain caused as a result of the displacements u is characterized by the symmetric linearised strain tensor

$$\varepsilon(u) = \{\varepsilon(u)\}_{i,j=1}^d, \quad \varepsilon_{ij}(u) = \frac{1}{2} \left(\frac{\partial u_i}{\partial x_j} + \frac{\partial u_j}{\partial x_i} \right).$$

In the above, \hat{n} corresponds to the unit outward pointing normal vector on $\partial\Omega$ and $E := E(\mathbf{x})$ denotes the fourth order elasticity tensor, describing the elastic stiffness of Ω as a result of the load placed upon it.

We will consider the case where our body consists of one or more isotropic materials (i.e: rotational and directional independence). Equation (1b) describing Hooke's Law can be written as

$$\sigma(u) = 2\mu \varepsilon(u) + \hat{\lambda} \operatorname{tr}(\varepsilon(u))\hat{I},$$

where \hat{I} represents the identity matrix of appropriate size, $\text{tr}(A)$ denotes the trace of a matrix A and both μ and $\hat{\lambda}$ correspond to Lamé constants defined in the usual manner

$$\mu := \frac{\bar{E}}{2(1 + \nu)}, \quad \hat{\lambda} := \frac{\nu \bar{E}}{(1 + \nu)(1 - 2\nu)}.$$

with $\bar{E} > 0$ corresponding to Young's modulus and $-1 < \nu < \frac{1}{2}$ the Poisson ratio. We now look to apply domain decomposition to the problem (1). To do this, we divide our domain Ω into N nonoverlapping subdomains Ω_i with local boundaries $\partial\Omega_i$ and outer unit normals \hat{n}_i . We denote by Γ the resulting skeletal interface $\Gamma = \bigcup_{i=1}^N \Gamma_i$ where $\Gamma_i := \partial\Omega_i \setminus \partial\Omega$, and by $I := \bar{\Omega} \setminus \Gamma$ the set of interior nodes, with $u|_{\Omega_i} =: u_i$. Assuming that the restriction of u_i to components of the skeletal interface $u_i|_{\Gamma_i}$ is known, problem (1) is equivalent to the following set of subproblems

$$\begin{aligned} \mathcal{L}u_i &= f_i && \text{in } \Omega_i, \\ u_i &= 0 && \text{on } \partial\Omega_D \cap \partial\Omega_i, \\ \sigma(u_i) \cdot \hat{n}_i &= g_i && \text{on } \partial\Omega_N \cap \partial\Omega_i, \\ u_i &= \lambda_i && \text{on } \Gamma_i, \end{aligned} \tag{2}$$

where $i = 1, \dots, N$. By writing $u_i = u_i^1 + u_i^2$, we look to describe an appropriate interface operator that will allow problems to be decoupled and thus solved strictly on subdomains in parallel. Through the definition of matrix extension operators H_i that map interface data to relevant subdomains via $u_i^2 = H_i \lambda$, the system (2) can be decoupled into the following $2N + 1$ subproblems

$$\begin{aligned} \mathcal{L}u_i^1 &= f_i && \text{in } \Omega_i, \\ u_i^1 &= 0 && \text{on } \partial\Omega_D \cap \partial\Omega_i, \\ \sigma(u_i^1) \cdot \hat{n}_i &= g_i && \text{on } \partial\Omega_N \cap \partial\Omega_i, \\ u_i^1 &= 0 && \text{on } \Gamma_i, \end{aligned} \tag{3a}$$

$$\sum_{i=1}^N \sigma(H_i \lambda) \cdot \hat{n}_i = - \sum_{i=1}^N \sigma(u_i^1) \cdot \hat{n}_i \quad \text{on } \Gamma, \tag{3b}$$

$$\begin{aligned} \mathcal{L}u_i^2 &= 0 && \text{in } \Omega_i, \\ u_i^2 &= 0 && \text{on } \partial\Omega_D \cap \partial\Omega_i, \\ \sigma(u_i^2) \cdot \hat{n}_i &= 0 && \text{on } \partial\Omega_N \cap \partial\Omega_i, \end{aligned} \tag{3c}$$

The associated weak form to problem (3b) is referred to as the Steklov-Poincaré equation, where the so-called Steklov-Poincaré pseudo-differential operator $S : \Lambda_\theta \rightarrow \Lambda'_\theta$ is defined in the following manner (Turner, 2014)

$$s(\lambda, \eta) = \langle S\lambda, \eta \rangle := \sum_{i=1}^N \left[\int_{\Gamma_i} (\sigma(H_i \lambda) \cdot \hat{n}_i) \eta \, ds \right] =: \sum_{i=1}^N \langle S_i \lambda_i, \eta_i \rangle,$$

where $\lambda, \eta \in \Lambda_\theta$ and $\lambda_{|\Gamma_i} =: \lambda_i, \eta_{|\Gamma_i} =: \eta_i$. The space Λ_θ is chosen to be a suitable fractional Sobolev space of index θ based on the boundary conditions of the problem, dependent on the intersection of Γ with $\partial\Omega$ (Quarteroni & Valli, 1999, Toselli & Widlund, 2005).

2 Matrix Formulation

Through a finite element discretisation of the weak formulation, it can be shown that the discrete formulation to the original problem (1) requires the solution of a matrix-vector system (Turner, 2014). By distributing nodes based on their location within the domain, we can view this system as follows

$$K\mathbf{u} = \begin{pmatrix} K_{II} & K_{I\Gamma} \\ K_{\Gamma I} & K_{\Gamma\Gamma} \end{pmatrix} \begin{pmatrix} \mathbf{u}_I \\ \mathbf{u}_\Gamma \end{pmatrix} = \begin{pmatrix} \mathbf{f}_I \\ \mathbf{f}_\Gamma \end{pmatrix} = \mathbf{f}, \quad (4)$$

where

$$K_{II} = \bigoplus_{i=1}^N K_{I_i I_i}, \quad \mathbf{u} = (\mathbf{u}_I, \mathbf{u}_\Gamma) \in \mathbb{R}^{n=n_I+n_\Gamma}. \quad (5)$$

In comparison, the corresponding matrix formulations for each of the discrete weak formulations to the problems presented in (2) can be written down as

$$K_{II}\mathbf{u}_I^1 = \mathbf{f}_I, \quad (6a)$$

$$S\mathbf{u}_\Gamma = \mathbf{f}_\Gamma - K_{\Gamma I}\mathbf{u}_I^1, \quad (S = K_{\Gamma\Gamma} - K_{\Gamma I}K_{II}^{-1}K_{I\Gamma}) \quad (6b)$$

$$K_{II}\mathbf{u}_I^2 = -K_{I\Gamma}\mathbf{u}_\Gamma, \quad (6c)$$

with global solution $\mathbf{u} = (\mathbf{u}_I^1, \mathbf{0})^T + (\mathbf{u}_I^2, \mathbf{u}_\Gamma)^T$. In the above, the matrix S corresponds to the Schur complement, and so the discretisation of the decoupled problem (2) can be viewed as a Schur complement approach to the discretisation of the global problem (1). Using (4) and (5), we are able to view (6) in terms of $2N + 1$ subproblems in the following way

$$K_{I_i I_i}\mathbf{u}_{I_i}^1 = \mathbf{f}_{I_i}, \quad i = 1, \dots, N \quad (7a)$$

$$S\mathbf{u}_\Gamma = \mathbf{f}_\Gamma - K_{\Gamma I_i}\mathbf{u}_{I_i}^1, \quad (7b)$$

$$K_{I_i I_i}\mathbf{u}_{I_i}^2 = -K_{I_i \Gamma}\mathbf{u}_\Gamma, \quad i = 1, \dots, N \quad (7c)$$

We therefore look to solve (4) by exploiting the potential for parallelisation present in (7).

3 Preconditioning

The systems we expect to solve will typically be both sparse and large scale, due to the expected fineness of the finite element discretization required in modern design processes, allowing for the computation of resolute solutions. This is of particular importance for domains containing sharp jumps, occurring for instance due to predefined fixed or void regions. Therefore, it is appropriate to consider iterative solution techniques when solving systems of the form (4). For our problem, we will consider GMRES (Saad & Schultz, 1986) for reasons to be described below.

In order to avoid the direct construction and application of the Schur complement matrix, and to improve the spectral properties of the system matrix, we seek an appropriate preconditioner for the system (4). Through the following choice of P , we see that

$$P = \begin{pmatrix} K_{II} & K_{I\Gamma} \\ 0 & S \end{pmatrix}, \quad KP^{-1} = \begin{pmatrix} \hat{I}_{II} & 0 \\ K_{\Gamma I} K_{II}^{-1} & \hat{I}_{\Gamma\Gamma} \end{pmatrix}.$$

The minimum polynomial of KP^{-1} is $(\lambda - 1)^d$, suggesting that iterative solution methods such as GMRES will converge in at most d iterations (Ipsen, 2002). Based on this, we propose to precondition from the right with an approximation \tilde{P} of P as follows

$$K\tilde{P}^{-1}\tilde{\mathbf{u}} = \mathbf{f}, \quad \tilde{\mathbf{u}} = \tilde{P}\mathbf{u},$$

where

$$\tilde{P} = \begin{pmatrix} K_{II} & K_{I\Gamma} \\ 0 & \tilde{S} \end{pmatrix}, \quad \tilde{P}^{-1} = \begin{pmatrix} K_{II}^{-1} & 0 \\ 0 & \hat{I}_{\Gamma\Gamma} \end{pmatrix} \begin{pmatrix} \hat{I}_{II} & -K_{I\Gamma} \\ 0 & \hat{I}_{\Gamma\Gamma} \end{pmatrix} \begin{pmatrix} \hat{I}_{II} & 0 \\ 0 & \tilde{S}^{-1} \end{pmatrix},$$

with \tilde{S} representing an approximation to the discrete Steklov-Poincaré operator. We therefore seek a representation of \tilde{S} that is not only practical to invert but can also be seen to provide an appropriate preconditioning strategy for the resulting interface problem.

The form of \tilde{S} chosen is based on work in (Arioli & Loghin, 2009), where discrete norm representations for projections of the interpolation spaces Λ_θ onto suitable finite dimensional subspaces are described and analysed. Discrete norms of the form

$$H_\theta = M + M(M^{-1}L)^{1-\theta}, \quad \theta \in [0,1], \quad (8)$$

are shown to be equivalent to their continuous counterparts on Λ_θ , where M and L denote the mass and Laplacian matrices respectively assembled on the interface Γ . One particular example corresponds to $\theta = 1/2$, which is shown in (Arioli & Loghin, 2009) to adhere to the same coercivity and continuity bounds as the discrete Steklov-Poincaré operator, leading to mesh independent performance of GMRES. The norms presented in (8) can be shown to be spectrally equivalent to

$$\tilde{H}_\theta = M(M^{-1}L)^{1-\theta},$$

Both of the above can be applied component-wise to a system, suggesting an appropriate form of \tilde{S} as

$$\hat{H}_\theta = \bigoplus_1^d \tilde{H}_\theta. \quad (9)$$

From the above, it is clear that fractional powers of matrices must be determined in order to apply the discrete norms. For relatively small problems, this can be achieved through direct methods such as a generalised eigenvalue decomposition. However, the complexity involved is $O(n_\Gamma^3)$ suggesting instead the use of iterative approaches for larger problems. In (Arioli & Loghin, 2009), approximations through the use of truncated Lanczos and inverse Lanczos algorithms are described, and will also be employed within this work through the use of flexible GMRES (Saad, 1993) to account for the changing nature of the preconditioner.

4 Results

We present various results in this section to illustrate our approach in practice. It should be noted that while certain examples involve symmetric system matrices, our choice of non-symmetric preconditioner suggests GMRES as an appropriate Krylov solver.

The test problem considered involves a cantilever beam over the 2D domain $\Omega = (0,2) \times (0,1)$, with downward force $f = 0.75$, and outward traction $g = 1$. The domain will be clamped on the right hand side through the application of homogeneous Dirichlet conditions on the relevant boundary. An illustration of the deflection as well as a pictorial example of a division of the domain (into 16 subdomains) is provided in Figure.

As discussed in the previous section, iterative approaches will be used for the application of \hat{H}_θ . For this work, it was found that the inverse Lanczos approach delivered the most promising results, largely due to the relatively small number of basis vectors required to apply the discrete norms.

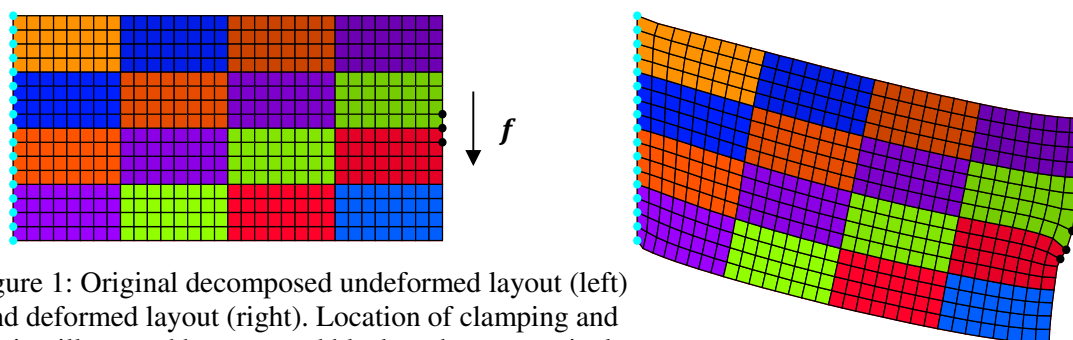


Figure 1: Original decomposed undeformed layout (left) and deformed layout (right). Location of clamping and traction illustrated by cyan and black nodes, respectively.

Table illustrates our results for differing mesh parameters h and subdomains. The column labelled $\tilde{S} = \hat{I}$ illustrates results for both test problems in the absence of interface preconditioning. By reading this column from top to bottom (for each problem), we observe a logarithmic dependence on the number of GMRES iterations for increasing mesh parameters. Reading this column from left to right also suggests a logarithmic dependence on the number of subdomains.

In comparison, the column labelled $\tilde{S} = \hat{H}_\theta$ of the table provides results with the interface preconditioner as discussed in (9). Here, it can be seen that the number of iterations are independent of the chosen mesh parameter. Whilst there is a logarithmic dependence on the number of iterations for an increasing number of subdomains, a direct comparison with the column labelled $\tilde{S} = \hat{I}$ suggests that our preconditioning strategy provides significant savings in the number of iterations required for convergence.

The final column labelled $\tilde{S} = \hat{H}_{OPT}$ illustrates results for selected values of theta based on testing. It was found that the recorded values were able to provide improved results over the other two columns, suggesting that different values of theta are able to provide a closer approximation to the decay of the associated Steklov-Poincaré operator.

Table 1: Results for the test problem. Tolerance of GMRES set at 10^{-6} .

| | $\tilde{S} = \hat{I}$ | | | $\tilde{S} = \hat{H}_\theta$ | | | $\tilde{S} = \hat{H}_{OPT}$ | | |
|------------|-----------------------|----|-----|------------------------------|-----|-----|-----------------------------|-----|-----|
| # Domains | 4 | 16 | 64 | 4 | 16 | 64 | 4 | 16 | 64 |
| θ | - | - | - | 0.5 | 0.5 | 0.5 | 0.5 | 0.6 | 0.7 |
| $h = 1/32$ | 28 | 47 | 68 | 12 | 18 | 27 | 12 | 17 | 22 |
| $1/64$ | 41 | 66 | 96 | 12 | 19 | 27 | 12 | 18 | 23 |
| $1/128$ | 59 | 93 | 137 | 12 | 19 | 27 | 12 | 19 | 24 |

In order to observe the computational benefits of our method, we look to provide rough estimates in order to gauge how our derived approach will perform in a parallel environment. Due to the non-overlapping nature of our approach, all subdomain solves can be carried out in parallel. As mentioned previously, the main issue surrounds the solution to the resulting interface problem. Within each application of our preconditioner to this problem, we are required to invert the discrete interface Laplacian. This issue is present in the Lanczos process, and also in the subsequent generalised eigenvalue decomposition that follows. Due to the structure of this matrix, these inversions can lead to a computational bottleneck for an increasing number of subdomains, and so we would like to consider an iterative approach to alleviate this issue.

The structure of the involved matrix suggests conjugate gradient as a suitable alternative, coupled with an appropriate preconditioning strategy (PCG). In this work, we propose to precondition by using the relevant contributions of L restricted to Γ_i , with the cross points removed to enable construction in parallel. The parallel CPU time taken for each GMRES iteration can then be realised by dividing the number of PCG iterations multiplied by the CPU time taken to apply the preconditioner by the total number of faces involved in the construction of Γ . By adding this contribution to the CPU time taken for one parallel subdomain solve, we calculate the total CPU time by multiplying the result to the total number of GMRES iterations required to achieve convergence.

The results for the investigation are displayed in Table below, where CPU times (in seconds) are provided for differing mesh and subdomain sizes. A Linux machine with an Intel® Core™ i7 CPU 870 @ 2.93 GHz with 8 cores was used to obtain the data. The bracketed numbers in the table indicate the total number of GMRES iterations required to achieve convergence.

Table 2: Total CPU times (seconds) anticipated through the use of parallel computing.

| # Domains | $\tilde{S} = \hat{H}_{OPT}$ | | | |
|------------|-----------------------------|---------|--------|--------|
| | 4 | 16 | 64 | 256 |
| θ | 0.5 | 0.6 | 0.7 | 0.75 |
| $h = 1/16$ | 0.0169 | 0.0168 | 0.0176 | 0.0254 |
| 1/32 | 0.0635 | 0.0273 | 0.0199 | 0.0232 |
| 1/64 | 0.4455 | 0.1238 | 0.0384 | 0.0238 |
| 1/128 | 3.8716 | 1.0804 | 0.2529 | 0.0623 |
| 1/256 | 50.2476 | 13.2858 | 3.3204 | 0.7295 |

From the table, it can be seen that for relatively coarse meshes, we do not see a significant enough decrease in the CPU time to warrant the use of parallelism. This behaviour can be attributed to the computational complexity of sparse matrix inversion ($O(k^2n)$, k is the bandwidth) for relatively small values of n , and also the efficiency of the backslash command in MATLAB. However, notable savings in CPU time equating to roughly factor 4 can be seen for finer meshes. These figures are encouraging, as they suggest that our approach is capable of significant speedup through the use of parallel architecture when compared directly to solving the problem globally on a single processor.

After collating the results in Table , a general increase was noted in the number of GMRES iterations when compared directly to the figures obtained in Table . The reason for this can be attributed to the use of inner PCG iterations. In particular, a logarithmic dependence on the mesh parameter was

observed for cases involving smaller numbers of subdomains. However, the deterioration can be seen as an acceptable compromise, as the results for larger meshes suggest the use of an increasing number of subdomains for improved performance. It should be noted that the results obtained above were done so with a relatively coarse tolerance for PCG of 10^{-3} .

It should not be expected that continual speedup can be gained through the use of an increasing number of subdomains, as certain factors such as inter-processor communication between each of the three steps will begin to play an important role. Therefore, in terms of a regular subdivision, this would suggest an optimal decomposition of the domain based on the mesh parameter, and also possibly other contributing factors relating to computer hardware.

5 Topology Optimization

As an application of our findings, we will describe how our work can be incorporated into commonly used solvers from problems arising in topology optimization. The problem we consider here is the so-called Variable Thickness Sheet problem (Bendsøe & Sigmund, 2003:p.54-57), which can be described mathematically using finite elements by the following nonlinear optimization problem

$$\begin{aligned}
 & \min_{\mathbf{u}, \boldsymbol{\rho}} && \mathbf{f}^T \mathbf{u} \\
 & \text{subject to:} && K(\boldsymbol{\rho}) \mathbf{u} = \mathbf{f}, \\
 & && K(\boldsymbol{\rho}) = \sum_{i=1}^m \rho_i K_i, \\
 & && \sum_{i=1}^m \rho_i \leq V, \\
 & && \bar{\rho} \leq \rho_i \leq \underline{\rho}, \quad i = 1, \dots, m.
 \end{aligned} \tag{10}$$

In the above, the n -vector of nodal displacement values $\mathbf{u} = \mathbf{u}(\boldsymbol{\rho})$ denotes the solution to the elasticity equations, with $\mathbf{f} \in \mathbb{R}^n$ representing the corresponding discretisation of the load linear form. The density $\boldsymbol{\rho} \in \mathbb{R}^m$ is subject to upper and lower bounds $\bar{\rho}$ and $\underline{\rho}$ respectively, with the volume of the body being denoted by V . Additionally, $K(\boldsymbol{\rho})$ represents the finite element stiffness matrix for the elasticity equations, with each K_i , $i = 1, \dots, m$ denoting elemental stiffness matrices.

By considering the method of Lagrange multipliers, minima to (10) are obtained through a nonlinear system of equations. The nonlinearities can be dealt with using a number of commonly used approaches. For instance, one could consider the use of interior point methods (Hoppe & Petrova, 2004). The fairly standard solution technique used by the community involves the consideration of fixed point type update schemes for an initial guess for the density in the following way

1. Finite Element Analysis (FEA) – solve equations of linear elasticity.
2. Density update – e.g.: OC (Bendsøe & Sigmund, 2003), MMA (Svanberg, 2002).
3. Check for convergence. If not satisfied, rerun 1 and 2 using updated density.

It can be expected that a reasonably large number of fixed point iterations are required to obtain a suitable final design. The bulk of computational effort will be concentrated on the Finite Element Analysis step, namely the repeated process of obtaining updated displacement variables through the

use of the equations of linear elasticity (Borrvall & Petersson, 2001). Therefore, we propose to apply our preconditioning strategy as discussed in Section 3 to this problem coupled with the fairly straightforward Optimality Criteria (OC) method for the density update. No attempt will be made here to carry out Step 2 above in parallel; however (Borrvall & Petersson, 2001) describe an appropriate implementation using the Method of Moving Asymptotes (MMA).

In Table , results are provided illustrating the performance of our approach for the cantilever beam problem. The results were obtained using an adaptive tolerance for GMRES based on successive compliance values. The total number of fixed point iterations are given, along with the average number of GMRES iterations per fixed point step (bracketed). Whilst the number of fixed point iterations appears to increase for finer meshes, the average number of GMRES iterations remains roughly constant. Whilst we still see a logarithmic dependence on the average number of GMRES iterations for an increasing number of subdomains, the fixed point iterations remain roughly constant.

Table 3: Results for the cantilever beam problem solved using our preconditioning strategy for the FEA coupled with the OC method for the density update.

| # Domains | 4 | 16 | 64 | 256 |
|------------|---------|---------|---------|---------|
| θ | 0.5 | 0.6 | 0.7 | 0.75 |
| $h = 1/16$ | 10 (10) | 10 (18) | 10 (33) | 10 (56) |
| $1/32$ | 17 (11) | 17 (18) | 17 (34) | 19 (54) |
| $1/64$ | 23 (11) | 23 (18) | 24 (32) | 27 (54) |
| $1/128$ | 29 (12) | 30 (17) | 32 (31) | 35 (52) |
| $1/256$ | 33 (13) | 36 (17) | 37 (31) | 41 (49) |

Future work involves validation of our approach on a parallel machine, as well as consideration of further problems (possibly to include 3D domains) and alternative solution methods to try to solve topology optimization problems completely in parallel. We expect our approach to adapt well in parallel, with potential speedup for 3D problems of factor 8 anticipated.

References

- Arioli, M. and Loghin, D. (2009). Discrete Interpolation Norms with Applications. *SIAM J. Numer. Anal.*, 47(4):2924–2951.
- Bendsøe, M. P. and Sigmund, O. (2003). *Topology Optimization: Theory, Methods, and Applications*. Springer Verlag, Providence, Rhode Island.
- Borrvall, T. and Petersson, J. (2001). Large-scale topology optimization in 3D using parallel computing. *Computer Methods in Applied Mechanics and Engineering*, 190(46-47):6201–6229.
- Hoppe, R. H. W. and Petrova, S. I. (2004). Primal–Dual Newton Interior Point Methods in Shape and Topology Optimization. *Numerical Linear Algebra with Applications*, 11(5-6):413–429.
- Ipsen, I. C. F. (2002). A Note on Preconditioning Nonsymmetric Matrices. *SIAM J. Numer. Anal.*, 23(3):1050–1051.

Quarteroni, A. and Valli, A. (1999). *Domain Decomposition Methods for Partial Differential Equations*. Numerical Mathematics and Scientific Computation. The Clarendon Press Oxford University Press, New York. Oxford Science Publications.

Saad, Y. (1993). A Flexible Inner-Outer Preconditioned GMRES Algorithm. *SIAM J. Sci. Comput.*, 14(2):461–469.

Saad, Y. and Schultz, M. H. (1986). GMRES: A Generalized Minimal Residual Algorithm for solving Nonsymmetric Linear Systems. *SIAM J. Sci. Statist. Comput.*, 7(3):856–869.

Svanberg, K. (2002). A Class of Globally Convergent Optimization Methods Based on Conservative Convex Separable Approximations. *SIAM Journal on Optimization*, 12(2):555–573.

Toselli, A. and Widlund, O. (2005). *Domain Decomposition Methods—Algorithms and Theory*, volume 34 of Springer Series in Computational Mathematics. Springer-Verlag, Berlin.

Turner, J. A. (Expected submission: 2014). *Application of Domain Decomposition to problems in Topology Optimization*. PhD thesis, University of Birmingham.

Investigating the Effects of Soft Spots on the Functional and Structural Condition of a Railway Track

Mohamed Wehbi, PhD student, department of civil engineering, University of Birmingham, UK.

Dr. Michael Burrow, lecturer, department of civil engineering, University of Birmingham, UK.

Dr. Gurmel Ghatoara, lecturer, department of civil engineering, University of Birmingham, UK.

Dr. Jin Shi, lecturer, School of civil Engineering, Beijing Jiaotong University, China.

Abstract

Overtime railway track starts to deteriorate due to the combined load of the traffic and environment. A major issue concerns the stiffness of the subgrade which has a significant effect on the performance of the track. Subgrade stiffness variation can manifest themselves as sudden changes in the spatial and elastic properties of the subgrade, these are known as soft spots. To investigate these aspects a validated 3-D finite element model of the train-track system was developed to determine track performance, in terms of functional and structural condition as a function of soft spot geometry. It was found that the location of the soft spot of the factors considered is the most influential parameter that affects structural condition of the track. The size of the soft spot was found to be the most influential parameter affecting the functional condition of the track.

Notations

E_{sg} : the stiffness of the subgrade, in MPa

E_s : the stiffness of the soft spot, in MPa.

TQ : track quality, in mm.

E_{dy} : dynamic stiffness, in KN/mm.

x : the width of the soft spot, in m.

z : the thickness of the soft spot, in m.

y : the length of the soft spot, in m.

r : the depth of the soft spot from the surface of the ballast, in m.

m : the horizontal distance between the centre line of the track and the centre line of the soft spot, in m.

1 Introduction

The railway track, in figure 1, may be considered to be a structural system which is designed to withstand the combined effects of traffic and the environment so that passengers comfort and safety are kept within acceptable limits and the subgrade is adequately protected. If appropriate and timely maintenance is not carried out, speed restrictions are maybe imposed resulting in financial costs. Variations in the properties of the subgrade may create zones of stiffer or softer materials that can affect the overall track performance (Frohling, 1997 and Berggen, 2007). Long wave stiffness variation may produce low frequency vibrations in the train affecting the passenger ride comfort. On the other hand, short wave stiffness variation may induce high frequency vibrations in the rail leading to local deterioration such as fatigue cracking of the rail and hanging sleepers (Dahlberg, 2007). Examples of short wave stiffness variation are soft spots. These can be described as the presence of a finite area with a low

stiffness surrounded by an area with a significantly larger stiffness. To investigate this aspect, a study was undertaken using a 3-D finite dynamic model of the rail track system was used to determine various measures of performance associated with the track as described below.

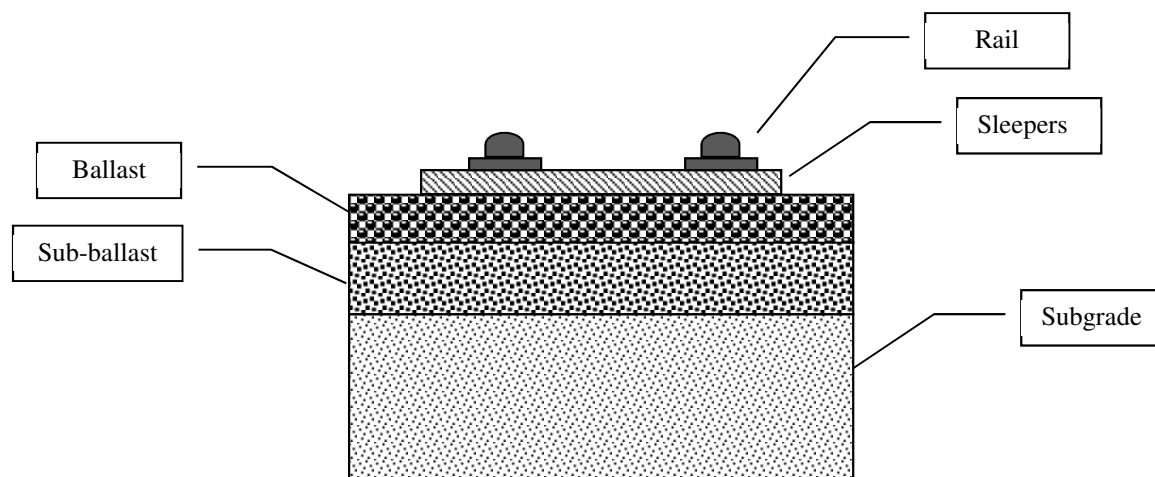


Figure 1: Railway track

2 Modelling a soft spot

An existing FEM of the rail track system was adopted (Shi et al, 2013) using ABAQUS explicit software and it comprises of a total 47555 elements and 64452 nodes constructing a track of 40 metres resting on a typical UK substructure (Burrow, 2007) (see figure 2). Also the train was modelled as shown in figure 3 and table 2. The model it was configured to simulate soft spot with low elastic stiffness surrounded by a stiff subgrade as shown in figure 4 and 5. The dimensions (x , y , z) and location (r , m) of the soft spot were changed for each scenario one at a time as shown in table 3.

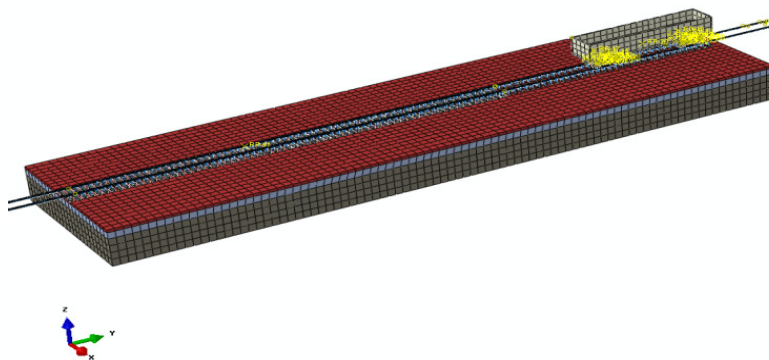


Figure 2: FE dynamic track model

Table 1: FEM specifications (after Shi et al, 2013)

| Specification | Value |
|---------------------------|------------------------|
| Track length | 40 m |
| Train length | 11 m |
| Train speed | 80 Km/hr |
| Number of axles | 4 |
| Wheel load | 125 KN |
| Rail stiffness | 210 GPa |
| Rail density | 7830 Kg/m ³ |
| Rail Poisson ratio | 0.3 |
| Sleeper spacing | 0.6 m |
| Sleeper stiffness | 35 GPa |
| Sleeper density | 2600 Kg/m ³ |
| Sleeper Poisson ratio | 0.22 |
| Sleeper's dimensions | 2.5 m, 0.25 m, 0.16 m |
| Ballast thickness | 0.3 m |
| Ballast stiffness | 180 MPa |
| Ballast density | 1650 kg/m ³ |
| Ballast Poisson ratio | 0.27 |
| Sub-ballast thickness | 0.7 m |
| Sub-ballast stiffness | 50 MPa |
| Sub-ballast Poisson ratio | 0.28 |
| Sub-ballast density | 1800 Kg/m ³ |
| Subgrade thickness | typically 3 m |
| Subgrade stiffness | Varying |
| Subgrade density | 1800 |
| Subgrade Poisson ratio | 0.3 |
| Soft spot Stiffness | 20 MPa |
| Soft spot density | 2100 Kg/m ³ |

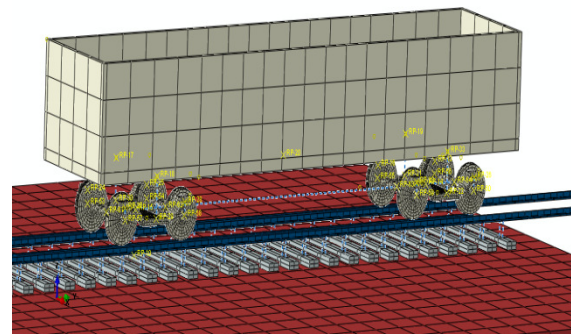


Figure 3: Vehicle Model

Table 2: Vehicle specification (after Shi et al.

| Specification | Value |
|--------------------------------|--|
| Mass of car body (M_c) | 91400kg |
| Inertia of car body (J_c) | $1.33 \times 10^5 \text{ kg} \cdot \text{m}^2$ |
| Mass of frame (M_f) | 1786kg |
| Inertia of frame (J_b) | $420 \text{ kg} \cdot \text{m}^2$ |
| Mass of wheel (M_f) | 1257kg |
| Primary suspension stiffness | 13MN/m |
| Primary suspension damping | $3 \times 10^5 \text{ Ns/m}$ |
| Secondary suspension stiffness | 4.4 MN/m |
| Secondary suspension damping | $4 \times 10^3 \text{ Ns/m}$ |

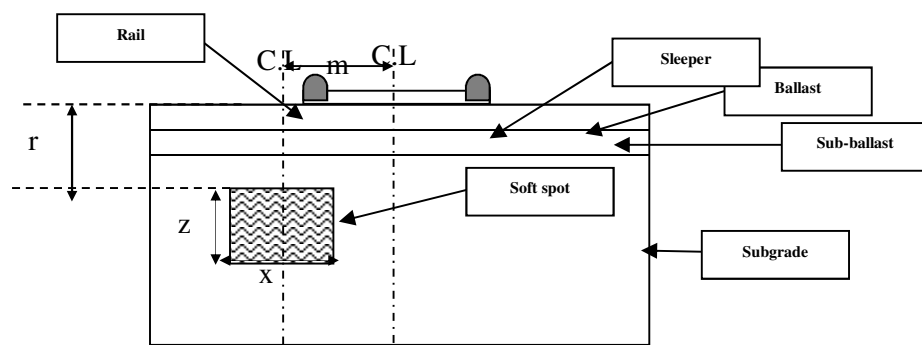


Figure 4: cross-sectional view of rail embankment with a soft spot

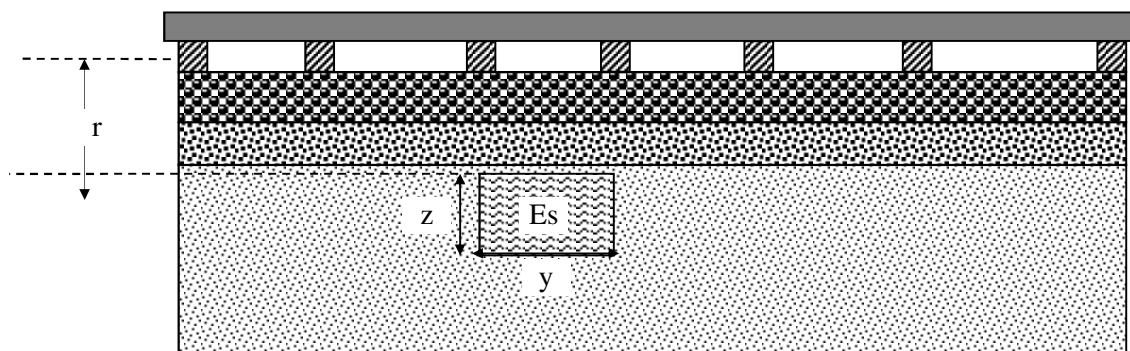


Table 3: soft spot scenarios configurations

| Scenario | Subgrade stiffness E_{sg} (MPa) | Soft spot stiffness E_s (MPa) | x (m) | y (m) | z (m) | m (m) | r (m) |
|----------|--------------------------------------|------------------------------------|---------|---------|---------|---------|---------|
| S1 | 20 | 100 | 4 | 3 | 5 | 0 | 1 |
| S2 | 20 | 100 | 4 | 3 | 10 | 0 | 1 |
| S3 | 20 | 100 | 4 | 3 | 15 | 0 | 1 |
| S4 | 20 | 100 | 2 | 3 | 5 | 0 | 1 |
| S5 | 20 | 100 | 8 | 3 | 5 | 0 | 1 |
| S6 | 20 | 100 | 4 | 1 | 5 | 0 | 1 |
| S7 | 20 | 100 | 4 | 2 | 5 | 0 | 1 |
| S8 | 20 | 100 | 4 | 1 | 5 | 0 | 2 |
| S9 | 20 | 100 | 4 | 1 | 5 | 0 | 3 |
| S10 | 20 | 100 | 4 | 3 | 5 | 2 | 1 |
| S11 | 20 | 100 | 4 | 3 | 5 | 4 | 1 |

3 Measure of track performance

To understand the influence of the dimension and location of the soft spot generally two types of measurements are carried out to determine track performance, namely; functional and structural. Functional measurements are associated with the way in which the track performs from the point of view of the user. Relevant measures include horizontal and vertical track geometry/track quality (Cope, 1993). Track quality (TQ) can be calculated as the standard deviation of vertical profile of the rail. It is desired to keep the value of track quality as low as possible. On the other hand, the measurements of structural condition are associated with the structural integrity of the track and include track dynamic stiffness (Berggen, 2007), and concerned with the long term performance of the track. Dynamic track stiffness (E_{Dy}) is the ratio between the instantaneous dynamic wheel load applied to the corresponding rail deflection at a particular position along the track. It is desired to keep the minimum dynamic stiffness at relatively high value to prevent rail fatigue.

4 Results

The analysis was carried out as it was described earlier to determine the effect of changing the size and location of the soft spot and the results are shown in figure 6 and 7. From these it can be observed that for most cases the structural and function condition of the track start to decrease as the size of the soft spot starts to increase. Similar observation can be also noted as the soft spot location moves closer to the rail. When the width (x) and length (y) of the soft spots exceeds the length and width of the train, the deterioration starts to diminish.

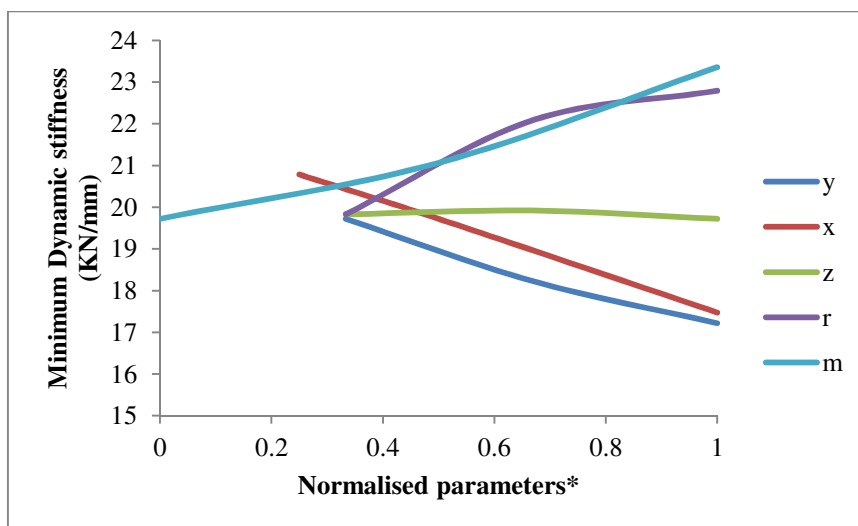


Figure 6: structural condition of the track vs. size and location of the soft spot

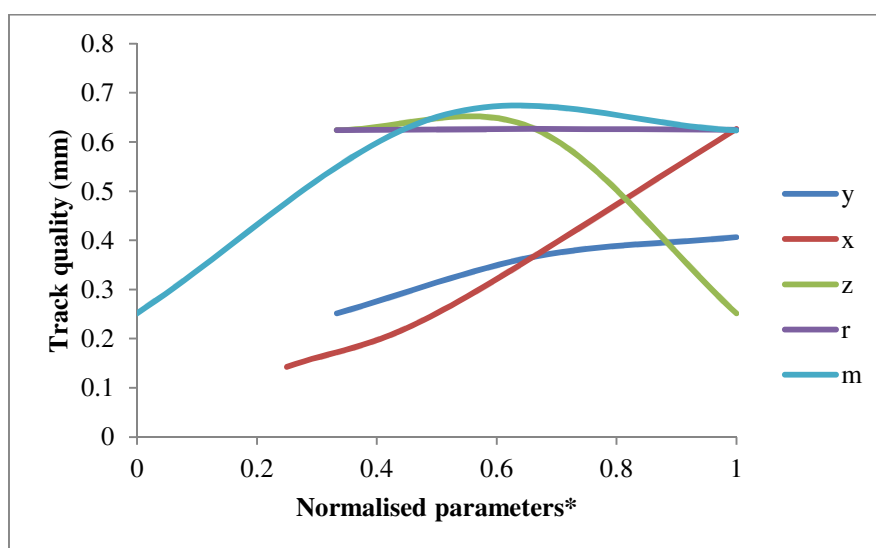


Figure 7: functional condition of the track vs. size and location of the soft spot

*The dimensions and the location are normalised by the maximum value of each parameter

An interesting observation can also be seen as the thickness of the soft spot (z) increases the function and structural condition start to improve. With the increase of soft spot thickness (z) the accumulated deflection will increase and a punching effect starts to manifest at the surface of the soft spot. As a result the stressed area will increase reducing the resultant

deflection which translates into an improvement in the overall condition of the track. Also as the soft spot get closer to the rail, i.e a decrease in (r, m) , the soft spot starts to experience higher stress amplitudes resulting in a decrease in the structural condition of the track. On the other hand, the functional condition of the track starts to worsen as the value of the horizontal distance (m) between the soft spot and the rail reaches 2m and then the condition starts to improve beyond that value. The reason for this is that at 2m distance the soft spot only affects one rail creating differential displacement between the two wheels of the axle.

In order to facilitate the predication of track quality and dynamic stiffness a regression analysis was carried out as suggested by Hamby, 2000 to try to relate track quality and dynamic stiffness as a function of the size and location of the soft spot. The resulting are shown in equation 1 and 2 and figure 7. The models had correlation factors (R^2) more of than 0.92. To determine the most parameter influential parameter the models coefficients were then converted to coefficients weightings using equation 3 and compared against each other; the higher the coefficient weighting the more important the parameter is.

$$E_{Dy} = C_1(x) + C_2(y) + C_3(z) + C_4(r) + C_5(m) \quad (\text{equation 1})$$

$$TQ = C_1(x) + C_2(y) + C_3(z) + C_4(r) + C_5(m) \quad (\text{equation 2})$$

$$CW_n = C_n / (C_1 + C_2 + C_3 + C_4 + C_5) \quad (\text{equation 3})$$

Where: x, y, z, r, m are soft spot parameters

C_1 to C_5 are regression coefficients

CW_n : nth parameter coefficient weighting

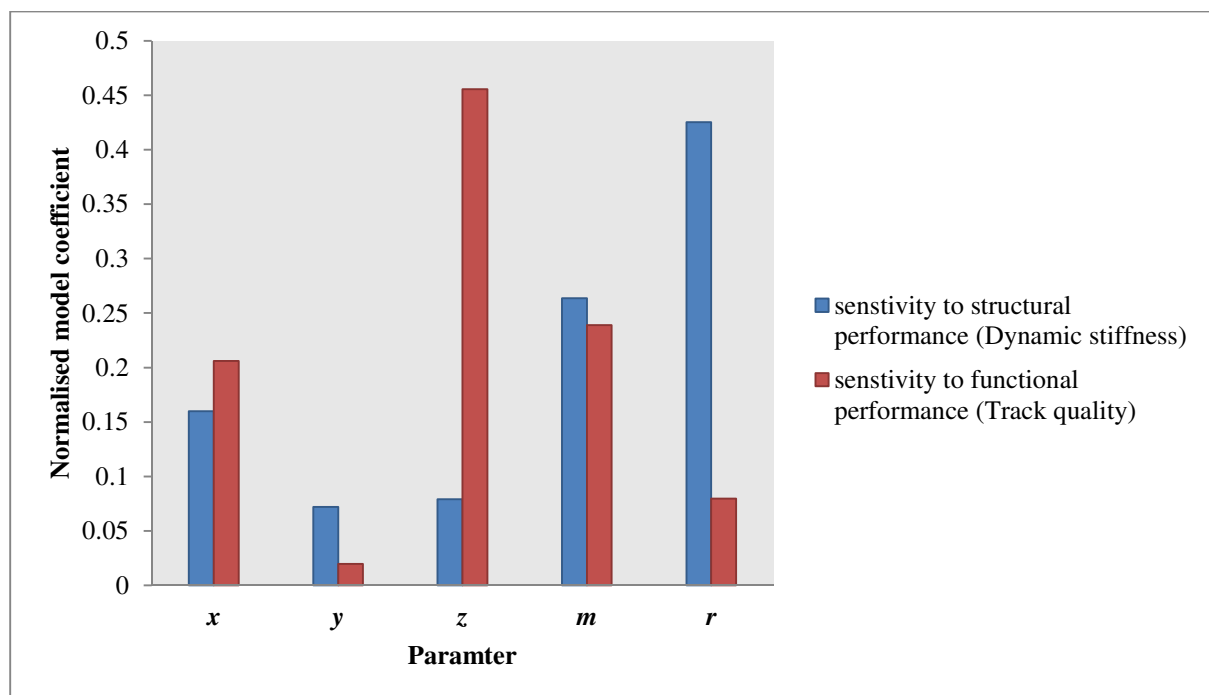


Figure 8: regression coefficients

From figure 8, it can be observed that the location (r , m) of the soft spot has a significant effect on the structural condition on the track; however, the size (z , x) of the soft spot is the most influential parameter that affects the functional condition of the track.

5 Discussion

Soft spots have significant effects on the overall condition of the track. However, there are number of analysis uncertainties in the analysis that need to be addressed including:

1. Elastic modelling: the behaviour of the substructure in the FE model is assumed to be linear elastic; however, previous studies have suggested that it should be modelled as a nonlinear stress-dependent material accompanied with field validation to provide a more accurate representation of the track's dynamic behaviour (Burrow et al, 2007).
2. Smooth rail surface: in the FE model it was assumed to have a perfectly smooth rail with no irregularities. In reality the presence of rail irregularities is unavoidable which has a significant impact on the dynamic load. Therefore modelling rail as smooth may provide underestimated results.
3. Performance indicators: in the analysis, track quality and dynamic stiffness were used to assess the functional and structural, respectively. Those two indicators may not provide a complete understanding of the overall condition of the track and other indicators such as the stress and ride comfort may provide different outcomes.
4. Regression analysis: due to the nonlinearity of the results described earlier multi-regression models were used to understand the influence of each parameter on the overall condition of the track. The results obtained from this method were in a reasonable agreement with the literature (Gonzalez, nd), however, other techniques such as regression Decision Trees and Nonlinear Multiple Regression Analysis maybe used to reinforce those findings.

6 Conclusions

While it is recognised that it is important to carry validations to the model, the following can be concluded from this study:

1. The overall condition of a railway track starts worsens as the soft spot size increases.
2. The functional and structural conditions of a railway track start to improve as the soft spot get further away from the rail.
3. The location of the soft spot is the most influential parameter in terms of the structural condition of the track.
4. The size of the soft spot is the most influential parameter in terms of the functional condition of the track.

References

- Berggren, E. (2009), **Railway track stiffness**, Royal Institute of Technology, Stockholm
- Burrow, M. (2007). Track Stiffness Considerations for High Speed Railway Lines. Centre for Railway Research and Education, School of Engineering, University of Birmingham, UK, Paulo Fonseca Teixeira, Head of Railway Division
- Burrow, M.P.N., Chan, A. H.C, and Shein, A. (2007). Falling weight deflectometer based inverse analysis of ballasted railway tracks. Geotechnical Engineering, Proceedings of the Institution of Civil Engineers. 160 July 2007 Issue GE3. pp 169–177.
- Cope, G. H., Ed. (1993), **British Railway Track: Design, Construction and Maintenance**. Loughborough, The Permanent Way Institution.
- Dahlberg, T.(2010). Railway Track Stiffness Variations – Consequences and Countermeasures International Journal of Civil Engineering, 2010; 8 (1) :1-12. URL http://ijce.iust.ac.ir/browse.php?a_code=A-
- Frohling .R. (1997). Deterioration of railway track due to dynamic vehicle loading and spatially varying track stiffness. From <http://upetd.up.ac.za/thesis/available/etd-01122009-160350/>
- Gonzalez, P, Cuadrado, M, Romo, E. (nd) Small structures in the core (nucleus) of the embankment in high-speedlines. Effects on the variation of the global stiffness of the track and design recommendations. Funacon Caminose De Hierro. Madrid.
- Hamby, D. (2000). A comparison of sensitivity analysis techniques. Savannah River Technology Centre. Westinghouse Savannah River Company.
- Shi, J., Burrow, M. & Chan, A. (2012), "Measurements and simulation of the dynamic responses of a bridge-embankment transition zone below a heavy haul railway line", **Proceedings of the Institution of Mechanical Engineers, Part F: Journal of Rail and Rapid Transit**, vol., no. pp. 254-268.

Posters

| Poster Number | Title | Principal Author |
|---------------|---|-----------------------|
| P01 | Numerical Studies of the enhancement of particle motion and drainage of a falling film by mechanical vibration of non-Newtonian fluids | Shuai Tian |
| P02 | Numerical Modelling Of Solid-liquid Suspensions In A Mechanically Agitated Vessel: CFD And Experiment | Zainab Talib |
| P03 | Adaptive Equalizers In LTE Technology | Zainab Talib |
| P04 | Data analysis for Sonolator results | David Ryan |
| P05 | A recognition model of ACP-HCS interaction for programmed β -branching in type I polyketide synthases | Rohit Farmer |
| P06 | Numerical Investigation Of Low-Velocity Impact Response of Monolithic Glass by 3D Finite Element Method (FEM) | Lasitha Kuruvita |
| P07 | Atomistic simulation studies of ThO ₂ : A potential nuclear fuel | Clare Green |
| P08 | Measurement of Train Aerodynamic Phenomena in operating conditions | Justin Morden |
| P09 | Investigating Radiation Damage in Materials for High Level Waste (HLW) Immobilisation | Geoffrey Cutts |
| P10 | Effect of laterality on symmetry / asymmetry of human lower limb based on mechanical model | Alireza Rastegarpanah |
| P11 | Global Optimisation of Pd-Ir Nanoalloys | Jack Davis |
| P12 | MOS correction of GCM- and RCM-simulated daily precipitation | Jonathan Eden |
| P13 | Numerical Evaluation of the Adequacy of Codified Methods for Progressive Collapses Resistance of Precast Concrete Cross Wall Structures | Mosleh Tohidi |
| P14 | Combined Experimental and ab initio study of magnetic ordering in Schafarzikite-related compounds | James Cumby |
| P15 | Theoretical Investigation of Possible Electrocatalysts for use in PEMFCs | Paul Jennings |
| P16 | Effects of the plan and mass Irregularities of RC Buildings on the Seismic Behaviour of NSCs | Ayad Aldeka |
| P17 | Turbulent and photochemical processes in a deep street canyon – a Large-Eddy Simulation | Jian Zhong |

| Poster Number | Title | Principal Author |
|----------------------|---|-------------------------|
| P18 | Velocity gradient as a tool to link mixing and biogas production in anaerobic digesters | Rebecca Sindall |
| P19 | Selective Laser Melting in AlSi10Mg Alloy | Wei Wang |
| P20 | Parametric sweep for Parallel Robot | Che Zulkhairi Abdullah |
| P21 | Energy Landscape Visualisation | Lewis Smeeton |
| P22 | A Plenoptic Camera Toolbox For Rendering, Simulation and Reconstruction | Chris Meah |
| P23 | Analytical and mechanical modelling of a proposed hydrogel using FE software to simulate the ICSI injection process | Amir Hajivayand |